DISSERTATION

FINITE-CLUSTER CALCULATIONS OF THE CONDUCTIVITY TENSOR, WITH APPLICATION TO ALKALI FULLERIDES AND THE ANDERSON IMPURITY MODEL

Submitted by

David Grant Steffen

Department of Physics

In partial fulfillment of the requirements

For the Degree of Doctor of Philosophy

Colorado State University

Fort Collins, Colorado

Summer 2003

ProQuest Information and Learning Company
300 North Zeeb Road
P.O. Box 1346
Ann Arbor, MI 48106-1346

COLORADO STATE UNIVERSITY

April 2, 2003

WE HEREBY RECOMMEND THAT THE DISSERTATION PREPARED UNDER OUR SUPERVISION BY DAVID GRANT STEFFEN ENTITLED "FINITE-CLUSTER CALCULATIONS OF THE CONDUCTIVITY TENSOR, WITH APPLICATION TO ALKALI FULLERIDES AND THE ANDERSON IMPURITY MODEL" BE ACCEPTED AS FULLFILING IN PART REQUIREMENTS FOR THE DEGREE OF DOCTOR OF PHILOSOPHY.

Committee on Graduate Work

(Please print name under signature)

Stuart Field

Stuart Field

Michael Kirby

MICHAEL KIRBY

Richard E. Eykholt

Richard E. Eykholt

Advisor

Martin P. Gelfand

David A. Krueger

Department Head

DAVID A. KRUEGER

ABSTRACT OF DISSERTATION

FINITE-CLUSTER CALCULATIONS OF THE CONDUCTIVITY TENSOR, WITH APPLICATION TO ALKALI FULLERIDES AND THE ANDERSON IMPURITY MODEL

We have developed a method, based on direct evaluation of the Kubo-Greenwood formula on finite clusters, to evaluate the zero-temperature conductivity tensor in zero and low magnetic fields for tight-binding models. We have applied this method to square-lattice Anderson impurity models, and to a class of models inspired by the alkali fullerides A_3C_{60}.

Experiments on A_3C_{60} show what appears to be a "universal" relation between Hall coefficient and lattice constant; such variations with lattice constant have usually been interpreted as indicating that that conduction bandwidth is the key physical property that is varying (everything else being nearly constant). However, our calculations are inconsistent with this standard interpretation, and we find that the data can only be accounted for within the models under consideration if one accepts the radical suggestion that the effective conduction band filling varies significantly with lattice constant. These calculations also exhibit enormous deviations from Matthiessen's rule.

Our results for the Anderson impurity model appear to exhibit the universal conductance fluctuations that would be expected in this sort of finite-cluster calculation. We present evidence for unanticipated universal fluctuations in the low-field Hall conductivity.

David Grant Steffen

Physics Department

Colorado State University

Fort Collins, CO 80523

Summer 2003

There is a theory which states that if ever anyone discovers exactly what the Universe is for and why it is here, it will instantly disappear and be replaced by something even more bizarre and inexplicable.

There is another theory which states that this has already happened.

- Douglas Adams [1]

"That's right," shouted Vroomfondel, "we demand rigidly defined areas of doubt and uncertainty!"

- Douglas Adams [2]

Acknowledgements

This work was entirely completed using GNU/Linux and other open source software. We are in debt to the open source community, and to the Free Software Foundation in particular, for their excellent software. Thanks also to the CSU high energy physics group, for the use of their computational facilities.

I wish to thank the instructors and students of Colorado International TaeKwon-Do, and particularly the students of the CSU TaeKwon-Do/Hapkido club, who have put up with a senior instructor who wasn't around nearly enough. Particular thanks are due to Mr. Roberto Roena, 6th Dan, for allowing his highest ranking student to disappear for months on end.

Support from my friends and family has been absolutely essential. In particular, I thank my parents, Dr. Grant E. and Nancy Stuart Steffen; my best friend and instructor, Roberto Roena; and most especially, particularly and unexpectedly, my fianceé Fade T Wall.

I would like to thank S. Sondhi, R. E. Eykholt and S. Roberts for useful conversations, and V. Crespi for enlightening correspondence concerning Ref. [3].

This work was supported financially in roughly equal amounts by the National Science Foundation through grant DMR 94-57928, and by the Colorado State University Department of Physics though generous teaching assistant assignments. Additional, and significant, financial support was provided by Prof. Aubrey Poore and Numerica Corp., and by Dr. Grant E. "It's only a loan if you don't finish!" Steffen, MD, MA.

And finally, I must thank my advisor, Professor Martin Gelfand, for his continuing help and abiding patience, and for putting up with me for this long.

Contents

1 Introduction and Overview 1

2 Models and Methods 8

2.1 The Kubo-Greenwood formula. 9

2.2 Realistic and toy tight-binding models 12

2.3 Incorporating the magnetic field 15

2.4 Units 17

2.5 Boundary Conditions 19

2.6 Low Field Expansion 19

2.7 Taking Limits and Notation 22

3 Analysis of the Anderson impurity model 24

3.1 Introduction 24

3.2 The Anderson impurity model 25

3.3 Density of states 26

3.4 Inverse Participation Ratios 26

3.5 Longitudinal conductance 30

3.5.1 The $L \to \infty$ limit 31

3.5.2 The $\eta \to 0$ limit 33

3.5.3 Comparison of limiting procedures 35

3.6 σ_{xy} and R_H 36

4 Universal Conductance Fluctuations **41**

4.1 Introduction 41

4.2 Mean free path 43

4.3 $\Delta\sigma_{xx}$ 44

4.4 $\Delta\sigma'_{xy}$ 47

4.5 Conclusions 49

4.6 Directions for Future Research 49

5 Alkali Fullerides **50**

5.1 Overview of the "standard model" of the electronic properties of A_3C_{60} 50

5.2 The Hall Effect in A_3C_{60} 52

5.3 A_3C_{60} Models 54

5.4 Results 57

5.4.1 Merohedral systems 58

5.4.2 Anderson systems 61

5.4.3 Mixed systems 63

5.5 Conclusions 68

5.5.1 Longitudinal conductivity 68

5.5.2 Hall effect 68

5.6 Directions for Future Research 71

A Derivation of the Kubo-Greenwood formula **72**

B The square-lattice Anderson impurity model **82**

B.1 The square-lattice nearest-neighbor tight binding model 83

B.1.1 Energy and Fermi surfaces 83

B.1.2 Electron velocity 84

B.2 R_H in the zero-disorder limit 85

B.2.1 Ong's technique 85

B.2.2 Longitudinal conductivity and onward to R_H 89

List of Tables

2.1 Units of electrical properties. 18

List of Figures

1.1 The C_{60} molecule. The small spheres represent the positions of the carbon nuclei. The molecule is ~ 10 Å in diameter. 2

1.2 Conceptual diagram of the electronic structure of molecular C_{60}, solid C_{60}, and A_3C_{60}. The h_u orbitals (depicted as being filled) are about 2.5 eV below the t_{1u} orbitals. The band corresponding to the t_{1u} orbitals is about 0.5 eV wide. 3

1.3 The two possible molecular orientations in solid C_{60}. Both orientations are shown from the point of view of the nearest neighbor. Hint: look at the orientation of the bond in the center of each picture. 4

2.1 The functional forms of the peaks involved in the zero-field σ (solid line) and the first-order correction to σ (dashed line). 22

3.1 Density of states per site for the 2D tight binding model. Also shown is the histogram of state energies, calculated directly for a 50×50 system with periodic boundaries. The divergence in the band center is logarithmic. 26

3.2 Inverse participation ratios for a 20×20 and a 45×45 system with disorder $D = 1$. 28

3.3 Effect of smoothing the inverse participation ratio for a 5×5 system (chosen to reduce the amount of data in the figure). 29

3.4 Inverse participation ratios for different sizes of system as a function of energy. These systems all had a disorder parameter $D = 1$. 29

3.5 Inverse participation ratio at the Fermi energy (for 2/3 filling), multiplied by N, as a function of the number of states (i.e., lattice sites) in the system. 30

3.6 $\sigma_{xx}(\omega)$ for a 50×50 system with periodic boundaries, and for open-boundary systems of several sizes. All systems have $L = 50$, $D = 1$ and $\eta = .01$. 31

3.7 System size extrapolation for two disorder levels; in both cases, $\eta = 0.02$. The lines (solid for $D = 0.3$, dashed for $D = 0.5$) are the results of fitting to Eq. (3.1). 32

3.8 Distribution of σ_{xx} for $L = 10$, $D = 0.5$, and $\eta = 0.01$. 33

3.9 $\sigma_{xx}(D, L, \eta)$ vs. η for a 30×30 system with a disorder of $D = 0.3$. The points are the results of averaging over ~ 100 systems; the error bars are the standard error, and (for most points) are smaller than the symbols. 34

3.10 Comparison of the two extrapolation procedures, limiting L then η, and limiting η then L. The symbols and error bars for the "η first" data have been offset slightly for clarity. 35

3.11 $\sigma^0_{xy}(\omega)$ for a 50×50 system with $D = 1$ and $\eta = 0.04$. Here we have averaged over 15 systems, and the error bars represent one standard deviation; they are only shown for every fourth point to improve readability. 36

3.12 $\sigma'_{xy}(\omega)$ for $D = 0.5$ and $\eta = 0.03$, for several system sizes. 37

3.13 Peak location for both $\sigma_{xx}(\omega)$ and $\sigma'_{xy}(\omega)$. 37

3.14 Results for $\sigma'_{xy}(D, L, \eta)$ using two extrapolation methods: using the maximum in $\sigma'_{xy}(\omega)$ (solid line), or taking the value at the location of the $\sigma_{xx}(\omega)$ peak (dashed line). The latter data has been offset in the x-direction slightly to make the error bars visible. 38

3.15 $\sigma'_{xy}(D, L, \eta)$ vs. η for 50×50 systems with $D = 0.5$. The extrapolated $\eta = 0$ value is 6900 ± 350. The error bars are statistical. 39

3.16 $\sigma'_{xy}(D, L)$ vs. L for several values of D. 39

3.17 R_H as a function of disorder. We have "extrapolated" in size by setting $L = 50$. The values of R_H calculated by other methods (0.989 via Appendix B, and 1.5 via the classical Drude result) are shown as dashed lines. 40

4.1 Mean free path as a function of D. 44

4.2 $\Delta\sigma_{xx}$ as a function of system size. The error bars represent the statistical standard error (from averaging over samples). The curves are fits to $a + 1/(bL)$ 46

4.3 $\Delta\sigma_{xx}(D, \eta = .01)$ for 50×50 clusters with open boundaries. 46
4.4 $\Delta\sigma'_{xy}(\eta = .01)$ as a function of system size in $L \times L$ systems. The error bars are statistical. 48
4.5 γ as a function of L for several values of D. The data for $D = 0.7$ and $D = 1$ are offset slightly in the x direction, to make the error bars more visible. 48

5.1 DOS as a function of band filling for Anderson systems. The bandwidths have been normalized. 57
5.2 DOS as a function of band filling for mixed systems; the clean system bandwidth (from Fig. 5.1) has been superimposed. The bandwidths have been normalized. . . . 58
5.3 Bandwidth as a function of Anderson disorder parameter D. The error bars are statistical. 59
5.4 $\sigma_{xx}(\omega)$ for merohedral systems with open and periodic boundary conditions. Here, we used $\eta = 0.01$. Statistical errors are roughly the width of the line. Using $\hat{a}$ for $K_3C_60 = 14.4$ Å, the conversion factor is $e^2/\hat{a}h = 536\ (\Omega\,\mathrm{cm})^{-1}$. 59
5.5 $\sigma_{xx}(D = 0, F)$ as a function of band filling, for merohedral systems with periodic boundaries at $\omega = 0$, and with open boundaries at $\omega = \omega_{\mathrm{peak}}$. The error bars are due to the η extrapolation. 60
5.6 $\sigma'_{xy}(\omega)$ for merohedral systems as a function of band filling. Here, $\eta = 3.21 \times 10^{-2}\hat{\epsilon}$. Statistical error bars are omitted for clarity. The conversion factor is $e^2\hat{a}/\Phi_0 h = 0.134\ (\mathrm{T}\,\Omega\,\mathrm{cm})^{-1}$. 61
5.7 An example of the fit of $\sigma'_{xy}(D, F, \eta)$ to $(a\eta + b)^{-2}$, showing the need to restrict the fit to a range of "good" etas. The η axis is in terms of our "native" units. Here, the "good" eta range could be said to start at $\eta = 5 \times 10^{-4}$, but this was not consistently true. 62
5.8 $\sigma'_{xy}(D, F)$ as a function of the band filling F for merohedral systems. The error bars represent procedural errors. 62
5.9 Hall coefficient as a function of band filling for merohedral systems. The conversion factor is $\hat{a}^3 h/\Phi_0 e^2 = 4.671 \times 10^{-9}\ \mathrm{m}^3/\mathrm{C}$ 63
5.10 $\sigma_{xx}(\omega)$ for Anderson systems, with $F = 0.5$ and $\eta = .01$. 64

5.11 $\sigma_{xx}(D,F)$ as a function of band filling for Anderson systems. The error bars represent 5% error, due to the $\eta \to 0$ extrapolation. 64

5.12 R_H as a function of band filling, for Anderson systems with several values of D. Only the error bars for $D = 0.169$ are shown for clarity, and represent 7% error due to the η extrapolation. 65

5.13 Hall coefficient R_H as a function of D in Anderson systems at half filling. 65

5.14 $\sigma_{xx}(D,F)$ as a function of band filling for mixed systems. As usual the error bars represent 5% error from the η extrapolation. 66

5.15 ρ as a function of band filling for Anderson, merohedral, and mixed systems. The disorder parameter for all systems with Anderson disorder is $D = 0.169$. Error bars are omitted for clarity. Also plotted (topmost curve) is the sum of the merohedral and Anderson resistivities. The difference between this curve and the mixed system result is the deviation from Matthiessen's rule (labeled DMR) 67

5.16 R_H for mixed systems. Error bars are only shown for $D = 0.169$ for clarity, and are due to procedural error; the statistical errors were roughly 1/2 to 1/4 as large. . . . 67

5.17 R_H for mixed systems, as a function of Anderson disorder parameter D, at half filling. 68

B.1 Dispersion relation in the first Brillouin zone for the square 2-d tight binding model. 83

B.2 Fermi surfaces in the first Brillouin zone. The contours are at $1\hat{\epsilon}$ increments. 84

B.3 Average Fermi velocity $\langle v_F \rangle$ as a function of Fermi energy. 86

B.4 Curves defined by $\vec{l}$ as we move around the Fermi surface of the square lattice tight binding model. The axes have units of $\hat{a}\epsilon\tau/\hbar$. Note that the area bounded by the curve vanishes at $E = 0$; for negative E values, the curves are identical to the positive E curves, but are traced out in the other direction (which causes the expected sign change at half filling). $E = 0.786$ corresponds to 2/3 filling. 87

B.5 A_l as a function of Fermi energy. 88

List of Symbols

- α, β: subscripts denoting components of vectors and tensors. Can be one of x, y, or z.
- ΔA: the fluctuations in quantity A. (See Chapter 4.)
- ϵ_r: energy of single-particle state r.
- η: the "smearing" parameter.
- Θ_{ij}: phase factor representing the magnetic field in the Hamiltonian.
- ξ: the localization length.
- μ, ν: molecular orbital indices.
- σ: the conductivity tensor. Elements are denoted $\sigma_{\alpha\beta}$.
- σ'_{xy}: the first-order correction to σ_{xy} due to a magnetic field.
- ω: frequency.
- ω_{peak}: the frequency at which the conductivity is a maximum.
- $\mathbf{A}$: the vector potential.
- a: the physical lattice constant.
- $\hat{a}$: the lattice constant, in the units used in our calculations. For fcc systems, our $\hat{a} = \frac{1}{2}a$.
- B: the magnetic field strength.
- D: Anderson disorder parameter.

- d: dimensionality of the system.
- E_F: Fermi energy.
- F: The bandwidth filling (usually represented as a percent).
- $f(\epsilon_r)$: the Fermi function, evaluated at the energy of state r. As our calculations are at zero temperature, we may always take $f = 1$ below the Fermi energy and $f = 0$ above it.
- H: the single-particle Hamiltonian.
  - H^0 is the zero magnetic field Hamiltonian; the first-order term in the magnetic field expansion is H'.
- i, j: lattice site indices.
- $\mathbf{j}$: the conductivity operator. Components are j_α.
- L: system size.
- ℓ: the elastic mean free path.
- ℓ_{in}: the inelastic mean free path.
- $\vec{l}$: the scattering-length vector (see Appendix B).
- N: number of states in the system, equal to the number of lattice sites multiplied by the number of molecular orbitals. In Appendix A, N represents the number of particles in a many-body state.
- $\mathcal{N}(E)$: density of states (usually, per site) at energy E.
- $P(E)$: the (smoothed) inverse participation ratio at energy E.
- p_i: the (unsmoothed) inverse participation ratio for state i.
- R_H: the Hall coefficient.
- $|r\rangle$: eigenstate of the Hamiltonian.

- $\mathbf{r}_i$: position of lattice site i.
- T_c: superconducting transition temperature.
- V: volume.
- $\mathbf{v}_F$: Fermi velocity.
- $\langle v_F \rangle$: Fermi velocity, averaged over the Fermi surface.

List of abbreviations

- KG: the Kubo-Greenwood formula
- DOS: the density of states
- DMR: deviations from Matthiessen's rule
- UCFs: universal conductance fluctuations

Chapter 1

Introduction and Overview

> In the beginning the Universe was created.
>
> This has made a lot of people very angry and been widely regarded as a bad move.
>
> - Douglas Adams [1]

In the beginning, we set out to study the Hall coefficient in A_3C_{60} compounds, by applying the Kubo-Greenwood formula to a variety of tight-binding models. This we did, walking a path much longer and more complicated than we expected, and encountering a variety of interesting phenomena along the way. Having walked this path, it is easy for *us* to see how these many pieces fit together; it is rather more difficult to explain to anyone else.

It is the purpose of this introduction to introduce the various pieces of this work, and to show, at least in a general way, how they all fit together. This is easier said than done. For example: to clearly understand the first sentence in this introduction, one must know A) what A_3C_{60} is, B) what the Kubo-Greenwood formula is, C) what a tight-binding model is and how one would apply the Kubo-Greenwood formula to it, and D) why anyone would want to do this, or care what the result was... and that's just the *first* sentence.

Here we will introduce the "dramatis personae" without delving too deeply into technical details.

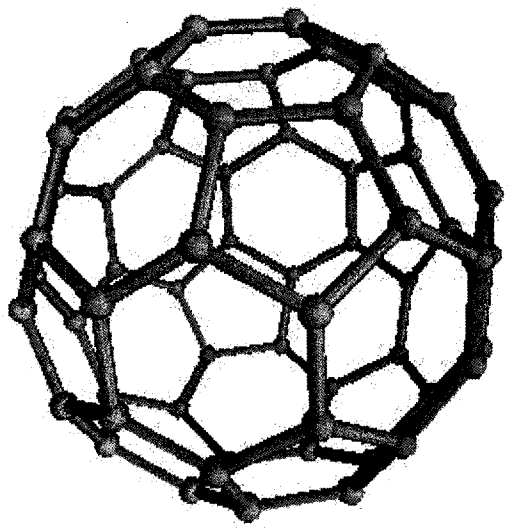

Figure 1.1: The C_{60} molecule. The small spheres represent the positions of the carbon nuclei. The molecule is $\sim$ 10 Å in diameter.

We will set out what we wanted to do, how we went about doing it, what we found when we did it, and what else we found along the way. We then conclude with an organizational overview of this work, to act as sort of a street map to the rest of the thesis.

The C_{60} molecule, commonly known as the "buckyball," is a hollow sphere of sixty carbon atoms that occupy the vertices of a truncated icosahedron—the same geometry as the seams on a soccer ball (Fig. 1.1). In the solid state, C_{60} molecules form an fcc lattice. Electronically, this solid is an insulator because the molecules have a roughly 2.5 eV gap between the highest occupied molecular orbitals (which are five-fold degenerate and fully occupied), and the lowest unoccupied orbitals (which are triply degenerate, and are referred to as t_{1u} orbitals, based on their symmetry properties); see Fig. 1.2 for a "cartoon" view of the situation. The intermolecular interactions are weak, so the bands formed from these orbitals do not overlap.

The buckyballs are large enough, with a 10 Å van der Waals diameter, for atoms to fit comfortably into the interstitial sites of the fcc structure; there are two "tetrahedral" sites and one "octahedral" site per C_{60} molecule. The tetrahedral sites are a snug fit for intercalated atoms, making their size responsible for the "chemical pressure" that affects the inter-C_{60} distance. It is energetically favorable for the buckyballs to always have a hexagonal face to these sites; the symmetry of the

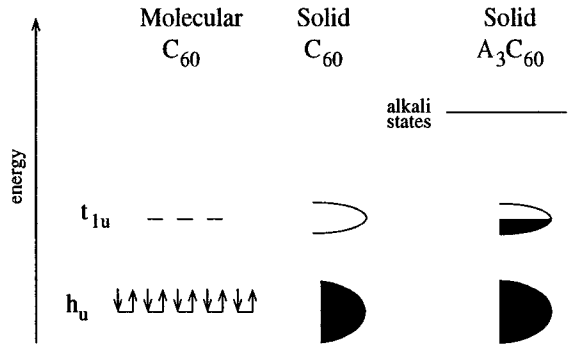

Figure 1.2: Conceptual diagram of the electronic structure of molecular C_{60}, solid C_{60}, and A_3C_{60}. The h_u orbitals (depicted as being filled) are about 2.5 eV below the t_{1u} orbitals. The band corresponding to the t_{1u} orbitals is about 0.5 eV wide.

buckyball is such that there are two equivalent ways to do this, which gives rise to "merohedral" disorder (discussed below). The octahedral sites are bigger, and intercalated atoms in them have no effect on the buckyball's orientation or on the chemical pressure. Alkali atoms, in particular, will diffuse through C_{60} solids at sufficiently high temperatures, forming intercalation compounds generically referred to as "alkali fullerides", i.e., A_xC_{60}. The alkali atoms act as electron donors, losing electrons to the conduction band formed by hybridization of the t_{1u} orbitals.

The most intensively studied class of alkali fulleride is A_3C_{60}, where A is K, Rb, or a mixture of those with Cs. This family of compounds exhibits a host of interesting and unexpected electrical properties, such as high temperature superconductivity (e.g., the superconducting transition in Rb_3C_{60} takes place at 29 K at ambient pressure) and the absence of resistivity saturation at high temperatures. A more detailed review of the current state of affairs concerning the electrical properties of these materials is deferred to Section 5.1.

The motivation for the present work was provided by an experimental result obtained by L. Lu *et al.* (hereafter referred to as "the Berkeley group"), who found that in single crystal K_3C_{60} and Rb_3C_{60}, the temperature dependence of the Hall coefficient R_H, when plotted on a single graph of R_H versus fcc lattice constant a, seemed to fall onto a single curve [3][1].They also found that R_H changes sign on going from $a \simeq 14.15$ (cold K_3C_{60}) to $a \simeq 14.45$ (warm Rb_3C_{60}), with nearly linear

[1]This was reminiscent of the behavior of the superconducting transition temperature T_c in the A_3C_{60} compounds, in which the variations with pressure for the various compounds almost fall onto a single curve when plotted against lattice constant. It was this T_c behavior that inspired the Berkeley group to look for similar behavior in their R_H data.

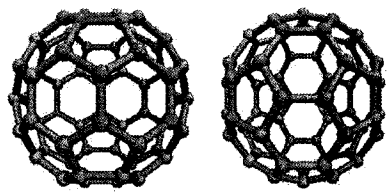

Figure 1.3: The two possible molecular orientations in solid C_{60}. Both orientations are shown from the point of view of the nearest neighbor. Hint: look at the orientation of the bond in the center of each picture.

dependence on a in between.

This experimental result is rather surprising. Within the classical Drude theory of transport, the Hall coefficient depends only on the densities and charges of the mobile charge carriers in a conductor, and the modest change in carrier density covered by the experimental conditions could not possibly account for their results, particularly not the sign change. Of course the Drude theory is not complete; many surprising Hall coefficient behaviors can be understood only within the modern theory of transport, in terms of scattering rates and the detailed properties of the Fermi surface. However, the apparent "data collapse" of R_H versus a onto a straight line suggests that the observed phenomenon is not, intrinsically, a dependence on temperature; one would expect the pressure-dependence of R_H in Rb_3C_{60} to exhibit the same behavior. What, then, could be changing with a, and a alone, to account for the change in R_H?

A detailed discussion of the explanation offered by the Berkeley group will be deferred until Chapter 5. The short version of the story is that single crystal A_3C_{60} is believed to have two main forms of disorder, with distinct characteristics. One, known as "merohedral" disorder, is associated with C_{60} orientations in the solid (see Fig. 1.3). Different orientations lead to different intermolecular transfer integrals for the t_{1u} states. The strength of this form of disorder scales with the conduction band width, which depends sensitively on a. The other form of disorder is alkali vacancies,[2] which shift the energies of the t_{1u} orbitals associated with nearby molecules. One would not, however, expect a strong dependence of these shifts on a. The Berkeley group attributed the behavior of R_H to the change in relative strengths of these types of disorder as the lattice constant (or, equivalently, the conduction band width) changes.

[2]It is known that alkali vacancies exist in Rb_3C_{60}, which is probably $Rb_{2.95}C_{60}$, so alkali vacancies certainly are *one* source of non-merohedral disorder in A_3C_{60}.

Since the variation of T_c with a in the A_3C_{60} phases is well understood as following primarily from the variation of conduction band width with a, this suggestion by the Berkeley group is a conservative, not radical, hypothesis. However, the details of their argument admittedly involved several questionable assumptions. We believed it was worth carrying out detailed transport calculations, with a minimum of *ad hoc* assumptions, to test the validity of their argument. In the end we found, to our surprise, that it may be necessary to reconsider the "standard model" of electronic structure of A_3C_{60}.

We also found very large deviations from Matthiessen's rule. Matthiessen's rule, as originally formulated, states that the scattering of electrons from impurities is independent of, and additive to, the scattering of electrons from lattice vibrations. More generally, in systems with more than one source of scattering, the resistivities due to each scattering source should add to produce the resistivity of the sample. Deviations from Matthiessen's rule (DMR) are not uncommon, having been found experimentally ever since Matthiessen and Vogt did their initial work on the subject in 1864. It is known that the presence of DMR can lead to considerable difficulty in the interpretation of low-temperature conductivity data [4, 5]. The large DMR we found in our A_3C_{60} models indicates that attempts to extract physical parameters from the experimentally measured temperature dependence of the zero field *longitudinal* conductivity may be unreliable.

These two statements are radical conclusions, which we put forth with some hesitation. However, they seem to follow directly from our calculations, together with the experimental results from the Berkeley group and the assumption that those results reflect the a dependence of R_H at low temperature.

This work can be seen as a continuation of the program begun by Gelfand and Lu [6, 7], who calculated electron transport properties of A_3C_{60} compounds, taking only merohedral disorder into account. Their work comprised calculations of the longitudinal conductivity, thermopower, and thermal conductivity at low temperature and zero magnetic field. Their approach, which we will follow here, is in some sense a "brute force" numerical method. We start with finite cluster of fcc lattice sites, each representing a C_{60} molecule, with either periodic or open boundary conditions; generate a Hamiltonian matrix for the conduction band states for that cluster via a tight-binding model; and then apply the Kubo-Greenwood (KG) formula to it. The present work involves extending their

calculations to non-zero magnetic fields, and adding Anderson disorder to the tight-binding model in an attempt to mimic the effects of alkali vacancies.

We go to the trouble of using this approach, rather than more commonly applied methods based on the Boltzmann transport formalism, because the Boltzmann formalism only makes sense if one can construct wave packets with well defined crystal momentum, which requires that $k_F\ell \gg 1$ (i.e., the mean free path be much larger than the intermolecular spacing). Measurements of the residual resistivity ρ_0 in A_3C_{60} compounds indicate that even at zero temperature $k_F\ell$ is of order unity, so one cannot have much confidence in the answers offered by conventional transport theory. This fact concerning A_3C_{60} justifies the application of finite cluster calculations, since the calculations can be carried out (in practice, not just in principle) for clusters larger than the mean free path.

We discuss the KG formula, in detail, in Chapter 2. The results of the KG calculations for finite clusters are not, by themselves, representative of the thermodynamic limit, and further analysis is needed to extract the information needed for comparison with experimental results. This analysis, which involves making several extrapolations, is not entirely straightforward. Here we were guided by results generated by applying our technique to simple two-dimensional square lattice models known as Anderson impurity models, which will be discussed in Chapter 3.

Our use of these simple two-dimensional models started as an exercise in proving, first the correctness of our code, and second the validity of our approach. Since we can estimate R_H in these systems by other (mostly) analytic methods, we can check our KG results for sanity. Upon closer inspection, these systems had some surprises of their own. Small two-dimensional conductors are well known to exhibit the phenomenon known as universal conductance fluctuations (UCFs). In Chapter 4 we discuss the nature of UCFs, exhibit them in our calculations of longitudinal conductance, and present some evidence that we may have encountered a related, but previously unrecognized, phenomena in the Hall conductance.

At the risk of some repetition, we conclude this introduction with a summary of our work, to act as a sort of "road map" which may be of use:

- Our calculational technique, based on tight-binding models and the Kubo-Greenwood formula, is set forth in Chapter 2. The Kubo-Greenwood formula itself is derived in Appendix A.
- Chapter 3 presents our results concerning the two-dimensional square Anderson impurity

model. This work serves two purposes: first, to validate our approach; and second, to establish procedures by which we may extrapolate from our finite-cluster results to the thermodynamic limit. We end up comparing R_H calculated via our approach with values found by other methods, which are discussed in Appendix B.

- Chapter 4 discusses the phenomenon of universal conductance fluctuations, an issue which we stumbled over while carrying out the work described in Chapter 3.

- Our results concerning A_3C_{60}, the main purpose of this work, are presented in Chapter 5.

Chapter 2

Models and Methods

> ... and so, the Universe being the puzzling place it is ... a race of hyperintelligent pan-dimensional beings once built themselves a gigantic supercomputer called Deep Thought to calculate once and for all the Answer to the Ultimate Question of Life, the Universe, and Everything.
>
> For seven and a half million years, Deep Thought computed and calculated, and in the end announced that the answer was in fact Forty-Two—and so another, even bigger computer had to be built to find out what the actual question was.
>
> -Douglas Adams [1]

In this chapter we describe the tight-binding models that we use to represent the conduction-band states in A_3C_{60}, and develop the equations we use to calculate the conductivity tensor for those models. Keep in mind that our primary goal is to examine the Hall coefficient, which is related to the conductivity tensor σ by

$$R_H = \frac{1}{B}\frac{\sigma_{xy}}{\sigma_{xx}\sigma_{yy} + \sigma_{xy}^2}$$

with B the magnitude of the magnetic field, taken to be in the z direction.

2.1 The Kubo-Greenwood formula.

The conductivity tensor expresses the linear relationship between current density and electric field that holds when the latter is small; it is an example of a linear response coefficient. A general expression for such coefficients, involving an integral over matrix elements of commutators of current operators with respect to exact many-body eigenstates, was presented by Kubo; alas, this expression is generally impossible to evaluate exactly. It was simplified by Greenwood in the case of electronic Hamiltonians in which direct electron-electron interactions are neglected,[1] which gives rise to the Kubo-Greenwood (KG) formula. For interested readers, we present a derivation of the KG formula from the Kubo formula in Appendix A. The KG formula will be the basis for all of our calculations, so let us first write it down in all its glory and then discuss its meaning and application:

$$\sigma_{\alpha\beta}(\omega) = \frac{2}{\omega V} \sum_{rs} \langle r|j_\alpha|s\rangle \langle s|j_\beta|r\rangle \left[f(\epsilon_r) - f(\epsilon_s)\right] \frac{i}{\hbar\omega + \epsilon_r - \epsilon_s + i\eta} . \tag{2.1}$$

Let us start on the left-hand side of the equation. Here, α and β are Cartesian indices x, y, or z, while ω represents the angular frequency at which the conductivity is measured. We will be most concerned with the dc conductivity $\sigma_{\alpha\beta}(\omega = 0)$, since the experimental results we wish to compare with are dc measurements; however, the KG formula is a result for the full frequency-dependent conductivity. Finite-frequency measurements of σ_{xx} are commonly carried out by a variety of experimental techniques (e.g., optical absorption), so the results at nonzero frequency are not just of theoretical interest. In fact, our expression here is not as general as it could be, because we could even consider the wave vector dependence of the conductivity; however, restricting our attention to zero wave vector is sensible because the wavelengths of light at the frequencies relevant to intra-band transitions in A_3C_{60} (microwave to infrared) are much greater than the length scales we can examine in our calculations. In principle the frequency dependence of σ_{xy} is experimentally measurable, but few such experiments have ever been done in the interesting frequency range because they are technically challenging [8].

Moving to the right-hand side of (2.1), the factor of 2 comes from spin degeneracy: in addition to neglecting direct electron-electron interactions we neglect spin-orbit coupling (which is an excellent

[1] Electron-electron interactions are assumed to be taken into account by an effective single-particle Hamiltonian and, hence, the many-body states are Slater determinants of single-particle states.

approximation for electrons associated with carbon atoms), so the electronic wavefunctions can be factored into separate spatial and spin components. V is the volume of the system. The bras and kets labeled r and s are single-particle eigenstates (spatial component only) with corresponding single-particle energies ϵ_r and ϵ_s. The Fermi function is denoted by f, so for zero-temperature calculations we may omit the factor $f(\epsilon_r) - f(\epsilon_s)$ and instead restrict the sum to $\epsilon_s > \epsilon_F > \epsilon_r$, where ϵ_F is the Fermi energy that separates occupied from unoccupied states.

The final ratio on the right-hand side should be looked at in the context of the identity for positive, real, infinitesimal η:

$$\lim_{\eta \to 0^+} \frac{i}{x + i\eta} = \pi\delta(x) + iP\left(\frac{1}{x}\right),$$

which holds in the "distributional" sense (that is, for the purposes of integrating). The KG formula gives both the real and imaginary parts of the conductivity, in a form which trivially satisfies the Kramers-Kronig relations. Our considerations will be restricted to the real part only.[2] Notice that for σ_{xx}, the product of current matrix elements is a positive real number; the real part of the conductivity is a sum of delta functions at frequencies associated with transitions between occupied and empty states. Although the positive, real, infinitesimal value η is introduced in the derivation of the KG formula for purely technical reasons (in order to regularize a divergent integral), we will see that for practical computations it is necessary for η to take on finite values, with the $\eta \to 0^+$ limit being one of the last (and most difficult) steps. For finite η,

$$\frac{i}{x + i\eta} = \frac{\eta}{x^2 + \eta^2} + i\frac{x}{x^2 + \eta^2},$$

so the delta functions are replaced by Lorentzians and the singularities are smoothed out (see Fig. 2.1). The amount of "smearing" is governed by η.

We can see that in order to evaluate the KG formula, we will need expressions for single-particle eigenvalues, eigenvectors, and current operators. All of these will follow from the single-particle Hamiltonian H. The particular form of H we use is a "tight-binding model," and we will describe it below in detail. The essential feature of such a model is that the Hilbert space of the electrons is

[2] We should note that there is an additional term in the KG formula that we are omitting; it is purely imaginary, and has no effect on any of our work.

strongly restricted. Rather than describing each electron by a general wave function $\psi(\mathbf{x})$, the wave function is taken to be a linear combination of t_{1u} molecular orbitals. Thus the Hamiltonian for a system composed of N C_{60} molecules is represented by a $3N \times 3N$ matrix.

Many methods based on the KG formula have been used to numerically evaluate elements of the conductivity tensor for tight binding models: they all have common underlying physics but differ substantially in technical details of implementation. Examples include transfer matrices [9, 10] and various forms of the recursion method [11, 12]. In all these approaches, calculation of off-diagonal elements of σ are rare; we are aware of only two references [13, 14].

The procedure we will apply, following Gelfand and Lu, is of a different nature: we directly apply the Kubo-Greenwood formula to finite clusters. The Hamiltonian matrix for a particular finite cluster is constructed and diagonalized, and the resulting eigenvalues and eigenvectors are inserted into the KG formula. This would seem to be the end of the story, but there are two complications. The first is that the result of any one such calculation is not physically relevant; the resolution of this is well understood, at least in principle, and we will discuss it momentarily. The second is that the effect of the magnetic field needs to be introduced in order to evaluate R_H, and we will discuss that in Section 2.3.

What do we mean by the statement that the result of a KG calculation for any particular finite cluster is not physically relevant? Consider first that we are considering disordered systems, and a given finite cluster represents only a particular *realization* of the disorder for some system with N C_{60} molecules and some Fermi energy. Experiments are carried out on systems where N is so large as to be effectively infinite, and the conductivity in three-dimensional metals is believed to be self-averaging,[3] that is, the conductivity should be independent of the particular realization of disorder as $N \to \infty$. In infinite systems, the spectrum of eigenvalues is dense, and the sum over delta-functions in the KG formula becomes a nice, continuous function of ω. We want to reproduce that infinite system's smooth function, but we can only evaluate the KG formula for systems that are not too large, since full matrix diagonalization is impractical for matrices of dimension larger than a few thousand (at least with the computational facilities available to us). The problem is, in other words, that while we want to calculate the macroscopic properties of A_3C_{60}, the clusters from

[3] At zero temperature, two-dimensional metals are *not* self-averaging, and one-dimensional metals are statistically pathological. These issues are discussed in Chapter 4.

which we can generate results are not macroscopic.

What can we do? First, we can carry out an ensemble average of the conductivity. That is, we perform the calculation for some number (typically tens) of realizations of the disorder and then average the results. This gives, in effect, a denser set of delta-functions for σ_{xx} than for any single realization. Second, we can evaluate the KG formula for finite values of η; in particular, we take values of η which are sufficiently large that the contributions due to many (at least tens of) transitions overlap at any ω. If the relevant energy scale for variations in the conductivity (which is of order h/τ, where τ is the mean free time) is greater than η, and if the relevant length scale for electron transport (the mean free path ℓ) is smaller than the linear dimensions of the sample, then these ensemble-averaged, smoothed conductivities of finite clusters should be representative of the thermodynamic limit. We will try to do even better, by carrying out the calculations for several η values, and extrapolating $\eta \to 0$.

One final problem associated with the finite systems is associated with boundary conditions. For an infinite system boundary conditions ought to be irrelevant, but for finite systems there are noticeable differences in the conductivity between systems with periodic and open boundaries. In particular, for σ_{xx} the periodic boundary conditions lead to a Drude peak centered at $\omega = 0$, just as for infinite systems, while for open boundary conditions the peak is shifted to some $\omega_{\mathrm{peak}} > 0$, the value of which decreases as the system size increases. For calculations with open boundaries—which, unfortunately, we will have no choice but to carry out—it is necessary to consider how to extrapolate as a function of system size in order to extract dc conductivities. This matter, as well as that of the extrapolation in η, will be explored thoroughly in the context of particular tight-binding models.

2.2 Realistic and toy tight-binding models

Let us start by discussing the character of the tight-binding models to be considered in zero field; we will incorporate the magnetic field later. As noted in Chapter 1, detailed electronic structure calculations based on density functional methods (see, for example, [15]) suggest that conduction band states in A_3C_{60} are derived almost entirely from the three-fold degenerate t_{1u} orbitals of individual C_{60} molecules. Hence the degrees of freedom for a conduction-band wavefunction are its amplitudes

on particular molecules (which we will denote "sites" and label by indices i, j) and particular orbitals on each molecule (which we will label by three-valued indices μ, ν). A generic kinetic energy term in the Hamiltonian, then, would have the form $t_{(i\mu)(j\nu)} C^{\dagger}_{i\mu} C_{j\nu}$ in second-quantized notation. (Since we neglect spin-orbit coupling, we can treat our electrons as spinless except for the factor of 2 in the KG formula, and there will be no spin labels on the creation/annihilation operators.) Site-diagonal elements vanish, because the orbitals on any one molecule are orthogonal by construction, and for simplicity we take their energy as zero. The value of the coefficient $t_{(i\mu)(j\nu)}$ depends on both the relative position and orientation of the molecules; different realizations of merohedral orientational disorder correspond to different sets of $t_{(i\mu)(j\nu)}$. Specific numerical values have been derived for these coefficients in various ways, such as simple Huckel theory and fitting to band structures derived from density functional calculations [16, 17]. There are some differences between these approaches, but they are modest. The important qualitative features of the values of $t_{(i\mu)(j\nu)}$ are that

- they can be neglected except for nearest-neighbor sites;
- for a given pair of sites, the dependence on orbital index is strongly affected by the molecular orientations;
- and the variation of the $t_{(i\mu)(j\nu)}$ with respect to lattice constant is approximately given by a single multiplicative factor applied to all of the coefficients.

We adopt the $t_{(i\mu)(j\nu)}$ values from Gelfand and Lu [7], for convenience.

Since their work, however, evidence has accumulated that some other form of disorder besides merohedral plays a role in electron transport in the A_3C_{60} phases. Gelfand and Lu pointed out that, if merohedral disorder is the only form of disorder that exists, and if the number of electrons in the conduction band is fixed at three per C_{60}, then it follows directly from the KG formula that the residual (low temperature) resistivity ought to be essentially independent of lattice constant (and hence of pressure, and of particular alkali intercalant species). However, there is good single-crystal resistivity data which shows that the residual resistivity is an increasing function of the lattice constant. This implies that there are terms in the Hamiltonian which do not vary with lattice constant in the same manner as the $t_{(i\mu)(j\nu)}$. One physical origin for such terms could be alkali vacancies, which have been measured at the few percent level in Rb_3C_{60} [18]. It seems to us that

the main effect of such vacancies would be to introduce shifts in the energies of the t_{1u} orbitals on one molecule relative to another. They might also introduce splitting of the orbitals on any given molecule, since they would break the cubic symmetry of the molecular environments. However, in the absence of any quantitative knowledge concerning the effects of vacancies, we have chosen to introduce as few free parameters as possible into our model, and thus we have adopted

$$H = \sum_{ij\mu\nu} t_{(i\mu)(j\nu)} C^{\dagger}_{i\mu} C_{j\nu} + \sum_{i\mu} V_i C^{\dagger}_{i\mu} C_{i\mu} \tag{2.2}$$

as a more-or-less realistic tight-binding Hamiltonian for A_3C_{60}. The second sum represents the effects of alkali vacancies as orbital-independent but site-dependent potential energy terms. While one might expect correlations in the potential energy term between nearby sites, we have again tried to reduce the number of free parameters by taking the V_i to be uncorrelated, and chosen uniformly from the interval $[-\frac{D}{2}, \frac{D}{2}]$. Thus the strength of other-than-orientational disorder is characterized by the single quantity D. We will refer to this form of disorder as "Anderson disorder" for reasons that will shortly be made clear.

In all of our calculations for merohedrally disordered samples we will also assume that the two molecular orientations have equal probability and are uncorrelated. This is not entirely consistent with experiment, which, at least in Rb_3C_{60}, shows evidence for short-range orientational (anti)correlations [19, 20]. We will want to keep all these various limitations of our model in mind when eventually trying to compare the results of calculations with experiment.

For a system comprising N molecules the Hamiltonian is represented in the molecular orbital basis as a $3N \times 3N$ matrix, with V's on the diagonal and t's occupying some 3×3 off-diagonal blocks. If we write the elements of the Hamiltonian matrix as $H_{(i\mu)(j\nu)}$ then the current operator $\mathbf{j}$ can be expressed in matrix form as

$$\mathbf{j}_{(i\mu)(j\nu)} = \frac{ie}{\hbar} H_{(i\mu)(j\nu)} \left(\mathbf{r}_j - \mathbf{r}_i\right)$$

where $\mathbf{r}_i$ is the position of lattice site i (which we take as the center of the molecule, since the molecular orbitals have their center-of-mass at the molecule centers). The Hamiltonian and current matrices are all that one needs to proceed to evaluate the KG formula for a particular sample.

As noted in Chapter 1, in order to provide some checks on the validity of the computer codes, we have also carried out calculations for a simpler class of tight-binding models. These models involve sites on a two-dimensional square lattice (rather than fcc), with one orbital per site (rather than three), kinetic energy coefficients $t = -1$ between nearest neighbors (without any dependence on nearest neighbor) and potential energies chosen randomly from $[-\frac{D}{2}, \frac{D}{2}]$ (just as for our A_3C_{60} model). This is the Anderson impurity model [21], whence the name "Anderson disorder".

2.3 Incorporating the magnetic field

The Kubo-Greenwood formula, as written in (2.1), is valid for all values of the magnetic field. However, it is necessary to use eigenvalues, eigenfunctions, and current operators associated with a Hamiltonian that includes the relevant physical effects of a magnetic field. So our next step is to indicate how the tight binding Hamiltonians described above need to be modified.

The universally applied method for including the effects of weak magnetic fields in tight binding models is known as the London-Peierls approximation, or Peierls substitution [22]. The zero-field Hamiltonian matrix elements are simply modified by a phase factor:

$$\begin{aligned} t_{ij} &= t^0_{ij}\, e^{i\Theta_{ij}} \\ \Theta_{ij} &= \frac{e}{2\hbar}\,(\mathbf{A}_i - \mathbf{A}_j)\cdot(\mathbf{r}_i + \mathbf{r}_j) \end{aligned} \tag{2.3}$$

where $\mathbf{A}_i$ is the magnetic vector potential at site i, $\mathbf{r}_i$ is again the position of lattice site i, and the superscript on t^0 indicates the zero-field value. Here we have suppressed the Hamiltonian matrix orbital indices, present in the A_3C_{60} tight binding model, for simplicity; the phase factor depends only on the site indices. Since $\Theta_{ii} = 0$, the Peierls substitution does not affect the V_{ii} terms in the tight-binding Hamiltonian (2.2). For the Anderson impurity model this completely describes the effects of the magnetic field; however, for A_3C_{60} we must also consider the effects of the magnetic field on the molecular orbitals themselves. This point is further discussed in Chapter 5.

For Hall effect calculations, we choose to impart a magnetic field in the z direction, and for that $\mathbf{A} = Bx\hat{y}$ (with B the magnetic field strength) is a particularly simple choice of gauge. We can

rewrite the leading constant in the phase factor as π/Φ_0, where $\Phi_0 = h/e = 2.07 \times 10^{-7}\,\mathrm{G}\cdot\mathrm{cm}^2$ is the flux quantum. We then we have

$$\Theta_{ij} = \pi \frac{B}{\Phi_0} (x_i - x_j)(y_i + y_j) \ . \tag{2.4}$$

A calculation of the Hall coefficient would now appear to be straightforward, but there are two complications that arise immediately if one attempts to evaluate σ_{xy} using the KG formula. Firstly, there is the matter of what boundary conditions one can apply to the finite systems. In the absence of a magnetic field, periodic boundary conditions are preferred because they give rise to the least finite-size effects (as alluded to earlier). However, as we will discuss in Section 2.5 below, periodic boundary conditions are not suitable for calculations with a magnetic field.

Secondly, we are interested in calculating the low-field Hall coefficient, which in turn is associated with the behavior of σ_{xy} at low field. For an infinite system, σ_{xy} at zero field is exactly zero, and increases linearly with B at low field. It is first-order correction to σ_{xy}, which we will denote σ'_{xy}, which is of interest, with

$$R_H = \frac{1}{B} \frac{\sigma'_{xy}}{\sigma_{xx}^2}$$

(with σ_{xx} evaluated at zero field as well). For a finite system, unless the particular realization of disorder is invariant with respect to a $\pi/2$ rotation of the sample about the z axis, σ_{xy} is not zero at zero field. Upon a complete ensemble average (over all possible realizations of disorder), the zero-field σ_{xy} should vanish; in fact, by considering an ensemble in which every realization is paired with its $\pi/2$ rotation, the zero-field σ_{xy} will vanish exactly even in a finite ensemble average. However, the matter of trying to take ensemble-averaged results from finite-field calculations to derive a $B = 0$ slope is a complication that is entirely unnecessary. Instead, it is possible to derive an extension of the KG formula to evaluate σ'_{xy} directly for an individual sample, which can then be ensemble-averaged. An additional benefit of this extension is that its implementation requires only the diagonalization of the real zero-field Hamiltonian matrix, rather than of a complex Hermitian matrix that represents the Hamiltonian at finite field. We present the derivation in Section 2.6, and the result will serve as the basis for our numerical calculations of σ'_{xy}.

2.4 Units

Before proceeding, it is convenient to express everything in dimensionless quantities. We will, for the moment, use overbars to denote such quantities, in which the associated physical units have been factored out.

We begin with the Hamiltonian (2.2). The energies represented by $t_{(i\mu)(j\nu)}$ and V_i are, of course, measured in some energy unit; we will write this unit as $\hat{\epsilon}$, and rescale t and V accordingly; this will allow us to write the Hamiltonian as $\hat{\epsilon}\bar{H}$.

Next, we look at the current operators. We denote the unit of length[4] by $\hat{a}$ and rewrite the current operators:

$$\mathbf{j}_{ij} = \frac{ie}{\hbar} H_{ij}\left(\mathbf{r}_j - \mathbf{r}_i\right) \rightarrow \frac{ie}{\hbar}\left(\hat{a}\hat{\epsilon}\right)\bar{H}_{ij}\left(\bar{\mathbf{r}}_j - \bar{\mathbf{r}}_i\right)$$

where we have rescaled both the Hamiltonian and the site position vectors $\mathbf{r}$. We can then define the dimensionless current operators:

$$\mathbf{j}_{ij} = \frac{ie\hat{a}\hat{\epsilon}}{\hbar}\bar{\mathbf{j}}_{ij} \quad \text{with} \quad \bar{\mathbf{j}}_{ij} = \overline{H}_{ij}\left(\bar{\mathbf{r}}_j - \bar{\mathbf{r}}_i\right) \ .$$

Note that, since we write the i out front explicitly, $\bar{\mathbf{j}}$ is now an *anti*-Hermitian operator.

Now let us turn to the phase factor associated with the magnetic field,

$$\Theta_{ij} = \pi\frac{B}{\Phi_0}\left(x_i - x_j\right)\left(y_i + y_j\right) \ .$$

It is useful to break this into two terms, one spatial and one relating to the magnetic field strength. Define

$$\begin{aligned} \bar{\theta}_{ij} &\equiv \left(\bar{x}_i - \bar{x}_j\right)\left(\bar{y}_i + \bar{y}_j\right) \\ \bar{B} &\equiv \pi\frac{B\hat{a}^2}{\Phi_0} \end{aligned}$$

where we have taken the factors of $\hat{a}$ from the spatial terms and put it in $\bar{B}$ to make $\bar{B}$ dimensionless. Note that, geometrical factors aside, $\bar{B}$ is the number of flux quanta per lattice plaquette. We then

[4] We will take $\hat{a}$ to be *half* the fcc lattice constant for A_3C_{60}, and to be the usual lattice constant for the square lattice models.

Table 2.1: Units of electrical properties.

Quantity	2D	3D	C_{60}
$\sigma_{\alpha\beta}$	$\frac{e^2}{\hbar}$	$\frac{e^2}{\hat{a}\hbar}$	$= 536\ (\Omega\,\mathrm{cm})^{-1}$
σ'_{xy}	$\frac{\hat{a}^2 e^2}{\hbar}\frac{B}{\Phi_0}$	$\frac{\hat{a}e^2}{\hbar}\frac{B}{\Phi_0}$	$= 7.28\times 10^{-12}\frac{B}{\Phi_0}\ \mathrm{cm}/\Omega$
R_H	$\frac{\hat{a}^2}{e}$	$\frac{\hat{a}^3}{e}$	$2.33\times 10^{-9}\,\mathrm{m}^3/\mathrm{C}$

have $\Theta_{ij} = \bar{B}\bar{\theta}_{ij}$.

The eigenstate energies have the same units as the Hamiltonian, so define $\epsilon_r \equiv \hat{\epsilon}\bar{\epsilon}_r$ and $\hat{\epsilon}\bar{\omega} = \hbar\omega$. With a further rescaling of the volume, $V = \hat{a}^d\bar{V}$ with d the number of spatial dimensions of the system, and noting that the Fermi functions produce no units [so define $f(\hat{\epsilon}\bar{\epsilon}) = \bar{f}(\bar{\epsilon})$], (2.1) becomes

$$\begin{aligned}\sigma_{\alpha\beta}(\omega) &= \frac{2\left(\frac{ie\hat{a}\hat{\epsilon}}{\hbar}\right)^2}{\left(\frac{\hat{\epsilon}\bar{\omega}}{\hbar}\right)\hat{a}^d\bar{V}}\sum_{rs}\langle r|\bar{j}_\alpha|s\rangle\langle s|\bar{j}_\beta|r\rangle\left[\bar{f}(\bar{\epsilon}_r)-\bar{f}(\bar{\epsilon}_s)\right]\frac{1}{\hat{\epsilon}}\frac{i}{\bar{\omega}+\bar{\epsilon}_r-\bar{\epsilon}_s+i\eta} \\ &= -\left(\frac{e^2}{h\hat{a}^{d-2}}\right)\frac{4\pi}{\bar{\omega}\bar{V}}\sum_{rs}\langle r|\bar{j}_\alpha|s\rangle\langle s|\bar{j}_\beta|r\rangle\left[\bar{f}(\bar{\epsilon}_r)-\bar{f}(\bar{\epsilon}_s)\right]\frac{i}{\bar{\omega}+\bar{\epsilon}_r-\bar{\epsilon}_s+i\eta} \qquad (2.5)\end{aligned}$$

and we can now see the standard units of conductivity out in front. It is useful to note that

$$\frac{e^2}{h} \cong \frac{(1.6\times 10^{-19}\mathrm{C})^2}{(6.63\times 10^{-34}\mathrm{J}\cdot\mathrm{s})} \cong 3.861\times 10^{-5}\frac{1}{\Omega}\,.$$

Also note that our arbitrary units of energy $\hat{\epsilon}$ drop out, which is reassuring.

We now drop the overbars, and henceforth understand all quantities to be dimensionless, with one exception. The magnetic field strength arises in several other contexts, so we will denote the magnetic field strength by B and denote the unitless field strength by b; that is, $b \equiv \bar{B}$.

Finally, we summarize in Table 2.1 the units associated with these conductivity results for two and three dimensions. Using the room-temperature K_3C_{60} lattice constant of 14.4 Å, we translate the three-dimensional values into units more appropriate for comparing with experimental A_3C_{60} results.

2.5 Boundary Conditions

The subject of boundary conditions poses some technical problems. Periodic boundary conditions are generally used for finite-cluster calculations because they give results closest to an infinite system, i.e., they minimize finite-size effects. However, with the magnetic phase factor, periodic lattice boundary conditions are impossible to satisfy for arbitrary values of B; the allowed values are given (for our choice of gauge) by $b = q/N_y$ where q is an integer and N_y is the number of unit cells in the $\hat{y}$ direction. Recall that b is the magnetic field strength rescaled by one flux quantum per plaquette ($\Phi_0 = 2.07 \times 10^{-11}$ T cm^2). For a typical calculation on an A_3C_{60} model with a $6 \times 6 \times 4$ lattice, the smallest magnetic field we can introduce ($q = 1$) is roughly 600 T. (Czycholl [14] used periodic boundaries and proceeded in this fashion, as he was interested in high-field effects.) Since we are interested in the low-field Hall effect, that is to say, a calculation of σ'_{xy}, we will expand the matrix elements $t_{(i\mu)(j\nu)}$ in powers of b. This expansion completely destroys the periodic properties of the phase factor and makes periodic boundary conditions impossible to satisfy for any finite system.

Actually, we can use *some* periodic boundaries, if we are careful. What we cannot use are periodic boundaries that are crossed by nearest-neighbor bonds with a y component. The nearest-neighbor bonds in an fcc lattice always have two non-zero components to them, so for our A_3C_{60} calculations we cannot use periodic boundaries in x or y; however, we can use periodic boundaries in z. For the two-dimensional square lattices, we could (in principle) use periodic boundaries in x and fixed boundaries in y. However, since one of our motivations for looking at these lattices was to guide the analysis of our A_3C_{60} results, we follow suit and use fixed boundaries in x and y there as well.

2.6 Low Field Expansion

First we need to expand the Hall coefficient in powers of magnetic field strength. Recall that

$$R_H = \frac{1}{B} \frac{\sigma_{xy}}{\sigma_{xx}\sigma_{yy} + \sigma_{xy}^2} .$$

For the moment, write that as $R_H = \frac{1}{B}\Lambda(B)$, and expand Λ in powers of B; of course we get $R_H = B^{-1}\Lambda_0 + \Lambda_1 + B\Lambda_2 + \cdots$. However,

$$\Lambda_0 = \frac{\sigma^0_{xy}}{\sigma^0_{xx}\sigma^0_{yy} + \left(\sigma^0_{xy}\right)^2} ,$$

and for systems with square/cubic symmetry, the conductivity tensor is diagonal, so $\sigma^0_{xy} = 0$. The leading term in the expansion for R_H is

$$\Lambda_1 = \frac{\sigma'_{xy}}{\sigma^0_{xx}\sigma^0_{yy}} \quad \text{where} \quad \sigma'_{xy} = \left.\frac{\partial \sigma_{xy}}{\partial B}\right|_{B=0} .$$

So what we need is a Kubo-Greenwood expression for σ'_{xy}.

To obtain that, we expand the Hamiltonian in powers of b, substitute these expansions into the KG formula, and keep terms only to first order. The Hamiltonian expansion is:

$$H_{ij} = H^0_{ij} e^{ib\theta_{ij}} = H^0_{ij}\left[1 + ib\theta_{ij} + \mathcal{O}\left(b^2\right)\right]$$

and we only keep terms to first order, so $H_{ij} = H^0_{ij} + ibH'_{ij}$ where $H'_{ij} = H^0_{ij}\theta_{ij}$.

The current operators are

$$\begin{aligned} \mathbf{j}_{ij} = H_{ij}\left(\mathbf{r}_j - \mathbf{r}_i\right) &= \left(H^0_{ij} + ibH'_{ij}\right)\left(\mathbf{r}_j - \mathbf{r}_i\right) \\ &= H^0_{ij}\left(\mathbf{r}_j - \mathbf{r}_i\right) + ibH'_{ij}\left(\mathbf{r}_j - \mathbf{r}_i\right) \\ &= \mathbf{j}^0_{ij} + ib\mathbf{j}'_{ij} \end{aligned}$$

where the last line can be taken as defining $\mathbf{j}^0$ and $\mathbf{j}'$.

The single-particle energies ϵ do not change to first order. To see this, write the unperturbed eigenstates as $\left|r^0\right\rangle$, and consider that the first-order correction to the energy is

$$\begin{aligned} \epsilon'_a &= \left\langle r^0\right| H' \left|r^0\right\rangle \\ &= ib\left\langle r^0\right| H^0\theta_{ij} \left|r^0\right\rangle . \end{aligned}$$

This is a purely imaginary number, so on physical grounds, it must be zero. The first order correction to the eigenvectors can be written in the form $|r\rangle = |r^0\rangle + ib\,|r'\rangle$ with

$$|r'\rangle = \sum_{s^0 \neq r^0} \frac{|s^0\rangle \langle s^0| H' |r^0\rangle}{E_r - E_s}$$

where $|s\rangle$ is an eigenvector of the unperturbed Hamiltonian.

To summarize: when we expand to first order, the energies do not change; the only terms in the KG formula that are affected by the expansion are the matrix elements. With the above expressions for the eigenvectors and current operators,

$$\langle r\,|j_\alpha|\,s\rangle = \langle r^0\,|j^0_\alpha|\,s^0\rangle + ib\Big\{\langle r^0\,|j^0_\alpha|\,s'\rangle + \langle r^0\,|j'_\alpha|\,s^0\rangle + \langle r'\,|j^0_\alpha|\,s^0\rangle\Big\}$$

and the product of matrix elements in (2.5) ends up giving us seven terms:

$$\begin{aligned}
\langle r\,|j_\alpha|\,s\rangle\langle s\,|j_\beta|\,r\rangle \;&=\; \langle r^0\,|j^0_\alpha|\,s^0\rangle\langle s^0\,|j^0_\beta|\,r^0\rangle \\
&+\; ib\Big\{\langle r^0\,|j^0_\alpha|\,s^0\rangle\langle s^0\,|j^0_\beta|\,r'\rangle + \langle r^0\,|j^0_\alpha|\,s^0\rangle\langle s^0\,|j'_\beta|\,r^0\rangle + \langle r^0\,|j^0_\alpha|\,s^0\rangle\langle s'\,|j^0_\beta|\,r^0\rangle \\
&+\; \langle r^0\,|j^0_\alpha|\,s'\rangle\langle s^0\,|j^0_\beta|\,r^0\rangle + \langle r^0\,|j'_\alpha|\,s^0\rangle\langle s^0\,|j^0_\beta|\,r^0\rangle + \langle r'\,|j^0_\alpha|\,s^0\rangle\langle s^0\,|j^0_\beta|\,r^0\rangle\Big\}
\end{aligned}$$

which is quite a mouthful. Some additional notation will be useful; define

$$\begin{aligned}
\mathbf{M}^0_{\alpha\beta;rs} \;&\equiv\; \langle r^0\,|j^0_\alpha|\,s^0\rangle\langle s^0\,|j^0_\beta|\,r^0\rangle \\
\mathbf{M}'_{\alpha\beta;rs} \;&\equiv\; \langle r^0\,|j^0_\alpha|\,s^0\rangle\langle s^0\,|j^0_\beta|\,r'\rangle + \langle r^0\,|j^0_\alpha|\,s^0\rangle\langle s^0\,|j'_\beta|\,r^0\rangle + \langle r^0\,|j^0_\alpha|\,s^0\rangle\langle s'\,|j^0_\beta|\,r^0\rangle \\
&+\; \langle r^0\,|j^0_\alpha|\,s'\rangle\langle s^0\,|j^0_\beta|\,r^0\rangle + \langle r^0\,|j'_\alpha|\,s^0\rangle\langle s^0\,|j^0_\beta|\,r^0\rangle + \langle r'\,|j^0_\alpha|\,s^0\rangle\langle s^0\,|j^0_\beta|\,r^0\rangle
\end{aligned} \tag{2.6}$$

and we now have

$$\sigma_{\alpha\beta}(\omega) = -\left(\frac{e^2}{\hbar\hat{a}^{d-2}}\right)\frac{4\pi}{\omega V}\sum_{rs}\left(\mathbf{M}^0_{\alpha\beta;rs} + ib\mathbf{M}'_{\alpha\beta;rs}\right)\Big[f(\epsilon_r) - f(\epsilon_s)\Big]\frac{i}{\omega + \epsilon_r - \epsilon_s + i\eta}\,.$$

We now have explicit expressions for the real part of both σ and the first-order term in the magnetic field expansion σ'_{xy}:

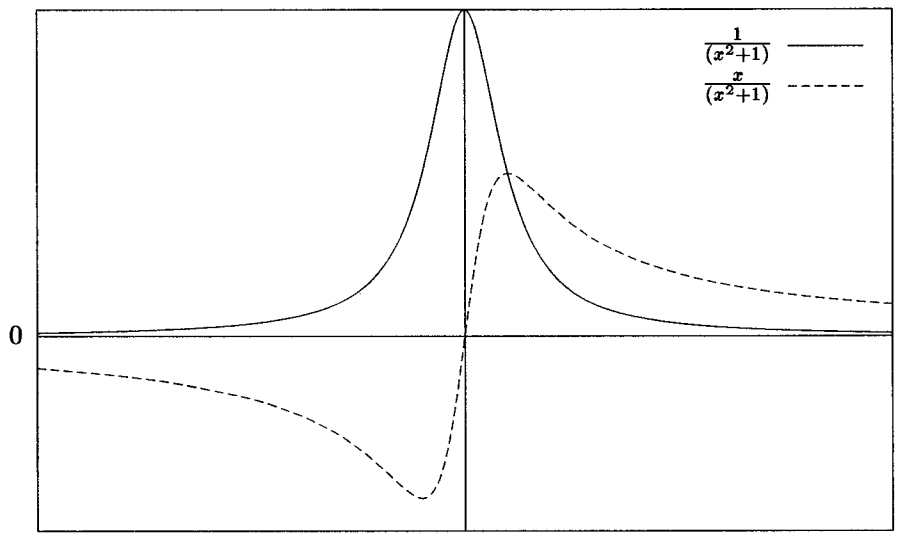

Figure 2.1: The functional forms of the peaks involved in the zero-field σ (solid line) and the first-order correction to σ (dashed line).

$$\sigma_{\alpha\beta}(\omega) = -\left(\frac{e^2}{h\hat{a}^{d-2}}\right)\frac{4\pi}{\omega V}\sum_{rs}\mathbf{M}^0_{\alpha\beta;rs}\left[f(\epsilon_r) - f(\epsilon_s)\right]\frac{\eta}{(\omega+\epsilon_r-\epsilon_s)^2+\eta^2} \tag{2.7}$$

and (writing out b explicitly)

$$\sigma'_{xy}(\omega) = \frac{B\hat{a}^2}{\Phi_0}\left(\frac{e^2}{h\hat{a}^{d-2}}\right)\frac{4\pi^2}{\omega V}\sum_{rs}\mathbf{M}'_{xy;rs}\left[f(\epsilon_r) - f(\epsilon_s)\right]\frac{\omega+\epsilon_r-\epsilon_s}{(\omega+\epsilon_r-\epsilon_s)^2+\eta^2}\,. \tag{2.8}$$

These are the equations we wish to evaluate.

Note that the zero-field conductivity tensor is a sum of Lorentzians (i.e., Lorentzians convolved with a delta function), while the first-order correction is a sum over similarly convolved first-order singularities. Fig. 2.1 shows the functional forms involved.

2.7 Taking Limits and Notation

As noted in Chapter 1, the result of evaluating the KG formula for a specific sample is not representative of the macroscopic system, but is dependent on the microscopic details of the disorder, boundary conditions, and so forth. We write $\sigma_{\alpha\beta}(\omega)$ because, strictly speaking, that is what the

Kubo formula gives you: the conductivity tensor as a function of driving frequency.

However, this is rather misleading. The KG formula is explicitly dependent on η, and implicitly dependent on a host of parameters that go into the particular tight-binding model from which we derive the Hamiltonian: the lattice used, the hopping parameters $t_{(i\mu)(j\nu)}$, the form of disorder, the Fermi energy (usually expressed as a percentage of the band that is filled), the specific realization of the disorder (i.e., the "sample"), and so forth.

For the purposes of this paper, we can reduce all these dependencies down to five parameters, and write

$$\sigma_{\alpha\beta} = \sigma_{\alpha\beta}\left(D, F, L, \eta, \omega\right)$$

where D is the magnitude of the Anderson disorder; F is the percentage of the band that is filled; L represents (in some form) the size of the system; η is the smearing parameter; and ω is the driving frequency.

In addition, we will (almost) always be talking about the ensemble average of σ; that is, for each value of the parameters, we average over many realizations of the disorder, or "samples", where a sample is simply the tight-binding model with a specific set of pseudo-random numbers used to generate the disorder. The notation is getting clumsy enough as it is, so instead of writing $\langle\sigma\left(\ldots\right)\rangle$ everywhere, we will drop the angle brackets and simply state that we are always talking about the ensemble average, unless otherwise explicitly noted.

As we take limits in various parameters, we will drop that parameter from the dependency of the result. Thus, $\sigma'_{xy}\left(D, F\right)$ is the first-order correction to the Hall conductance, with appropriate limits having been taken in the missing parameters (typically, $\omega \to 0$, $\eta \to 0$, and $L \to \infty$).

We make one exception: when we wish to talk about the (ensemble average) of σ without any limits having been taken, we will write $\sigma\left(\omega\right)$. This should pose no problem, since the ω limit will always be the limit we take first.

Chapter 3

Analysis of the Anderson impurity model

"Yes?" urged Arthur. He had picked up Slartibarfast's sense of urgency but didn't know what to do with it.

"Yes what?" said the old man.

"You were saying?"

Slartibartfast looked at him sharply.

"The numbers," he said, "are awful."

-Douglas Adams [23]

3.1 Introduction

Our study of simple, square lattice systems started simply as a way to check the correctness of our computer calculations. They ended up being crucial to guiding our interpretation of our results. Here we compare our numerical results with theoretical results, and also discuss in detail the analysis of our results.

This chapter is rather a mix of comparisons between our numerical results and other, theoretically, derived results; and a discussion of the techniques used to analyze our results so that we can compare them. We can not overstate the value of these checks. They started as simply a check on our computer code, but became a verification of our entire technique (i.e., the low-field expansion , the computer code, and so forth).

The rest of this chapter is organized as follows: first we present the model used. We then check that our calculated density of states (DOS) is correct. Next, we introduce the notion of the inverse participation ratio, and use this to find "good" values for the disorder parameter D (that is, values of D that produce conductors, i.e., systems with delocalized states at the Fermi level).

We then proceed to evaluate σ_{xx} for these models, and discuss the methods used to extrapolate our results to the thermodynamic limit. We perform much the same analysis to our results for σ'_{xy}, and obtain results for R_H. We then compare these results with those discussed in Appendix B.

3.2 The Anderson impurity model

The model we use is the Anderson impurity model [21]; it consists of a square, two dimensional lattice with a single orbital for each site (so $\mu = \nu = 1$). The Hamiltonian is given by (2.2), with $t_{(i\mu)(j\nu)} = -1$, and (as discussed in Section 2.2) the V_{ii} taken from a standard distribution on $[\frac{-D}{2}, \frac{D}{2}]$; the parameter D is a measure of the disorder in the system. D has units of energy, which for these systems is in arbitrary units $\hat{\epsilon}$. The possible energies range from $-4\,\hat{\epsilon}$ to $4\,\hat{\epsilon}$. See Appendix B for more details about this model.

We use L to denote the system size. Unless otherwise noted, all the Anderson impurity models we examine are $L \times L$ systems with open boundaries. Furthermore, we will suppress the Fermi energy dependence; all results in this Chapter (and the next) are at a band filling of 2/3 (i.e., $F = 0.67$), meaning that we set the Fermi level such that the lowest 2/3 of the allowed states are occupied. This filling corresponds to a Fermi energy $E_F = 0.786$ (obtained by integrating the DOS shown in Fig. 3.1).

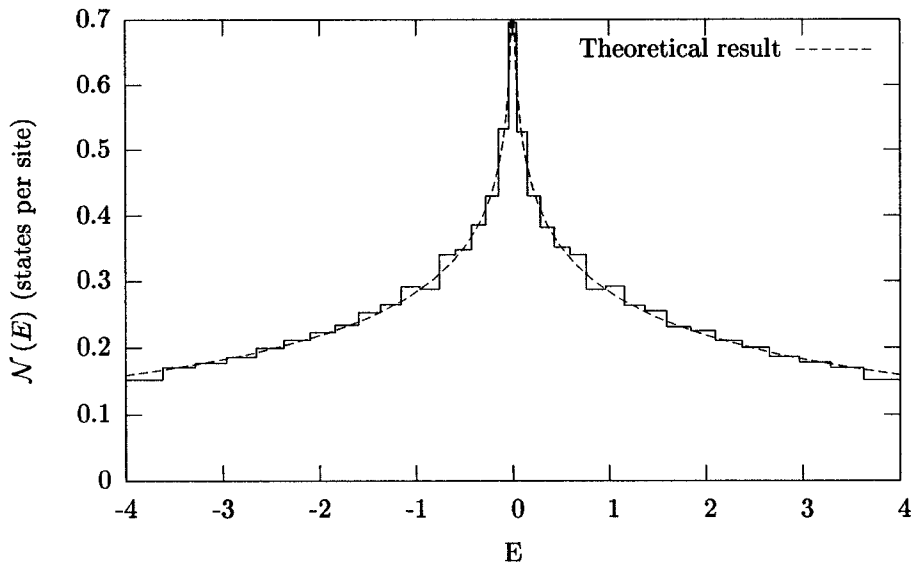

Figure 3.1: Density of states per site for the 2D tight binding model. Also shown is the histogram of state energies, calculated directly for a 50 × 50 system with periodic boundaries. The divergence in the band center is logarithmic.

3.3 Density of states

Since it is easy to check that we have gotten the density of states (DOS) right, we check this immediately. Sheng [24] shows theoretically that the expected density of states for this 2D model is given by $\mathbf{K}\left(\sqrt{1-E^2}\right)$ where $\mathbf{K}$ is the elliptic integral

$$\mathbf{K}(x) = \int_0^{2\pi} \frac{d\phi}{(1 - x^2 \cos^2 \phi)^{1/2}}.$$

which can be evaluated numerically. In Fig. 3.1 we compare this theoretical result with the result of directly diagonalizing the Hamiltonian for a 50 × 50 periodic system.

3.4 Inverse Participation Ratios

We are only interested in systems that are conductors, i.e., systems with delocalized states at the Fermi energy; we need to make sure the set of parameters we have chosen puts us in this regime. (This primarily answers the question "are our 2D systems big enough to give us meaningful results,

and what values of D should we use?") What do we mean by delocalized states? There is a length that characterizes the typical spatial extent of the wavefunctions at a given energy for an infinite system and a specified Hamiltonian. This is known as the localization length ξ. On a finite cluster, the states at a given energy are effectively delocalized if $\xi > L$; this will be true of any "metallic" system. An important point is that in one and two dimensions, the localization length is always finite; thus, in principle, there are no truly delocalized states, and no arbitrarily large metals [24]. In three dimensions, there is a characteristic energy that separates finite and infinite localization lengths [25].

In order to get a handle on the localization length, we examine the inverse participation ratio of an eigenstate ψ, defined as $p_i \equiv \sum \psi_i^4$. Delocalized states should have $p \sim 1/N$ where N is the number of states in the system, for values of N up to the system size of interest. Crudely, this result can be seen by assuming that ψ is uniformly spread out over the system, so $\psi_i = 1/\sqrt{N}$; the inverse participation ratio is then

$$p = \sum_{i=1}^{N} \psi_i^4 = \sum_{i=1}^{N} \frac{1}{N^2} = \frac{1}{N} \, .$$

This strict equality $p = 1/N$ is the result of the assumption above; real eigenstates are generally not so simple, and will have larger inverse participation ratios. However, we do expect the $1/N$ scaling to hold. On the other hand, when $\xi < L$ we expect p to be nearly independent of N. Again, let us assume ψ is spread out uniformly over a clump of N_l sites; then $p = 1/N_l$.

Ideally, this analysis would lead to some quantitative criterion for distinguishing between localized and delocalized states at the Fermi level. Unfortunately, this is not an easy thing to do. To be delocalized, all a state really has to do is extend across the sample; it may not be "clumped" in one place, and may not even be contiguous. Examining the inverse participation ratio will not give us definitive localized/delocalized answers; it will simply give us a rough idea of what systems are probably conductors, are what systems are not. Performing a detailed finite-size scaling analysis might be more revealing, but for our purposes that effort is not really necessary.

Figure 3.2 shows the calculated inverse participation ratios for each state, plotted against that state's energy. For further analysis, we need to treat the inverse participation ratio as a smooth, continuous function. We can produce such a function in much the same way we produce a smooth function from the delta functions in the Kubo-Greenwood equation: we replace each data point by

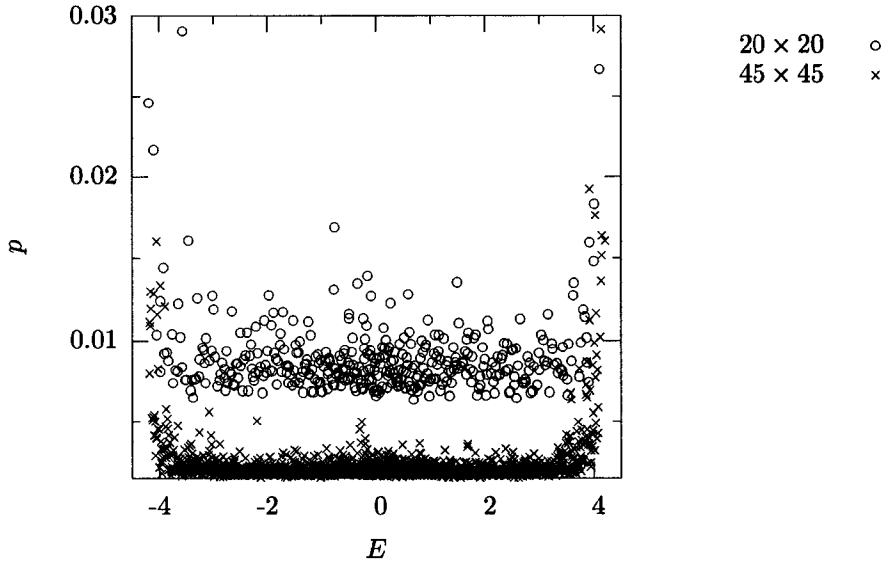

Figure 3.2: Inverse participation ratios for a 20 × 20 and a 45 × 45 system with disorder $D = 1$.

a Lorentzian function and add up the Lorentzians. Define

$$L(a, c, x) \equiv \frac{a\eta}{(x-c)^2 + \eta^2}$$

which is a Lorentzian of amplitude a centered at c with "width" η. The participation ratio p_i of state i at energy E_i is then replaced by $L(p_i, E_i, E)$. Our smoothed inverse participation ratio $P(E)$ is then given by

$$P(E) = \frac{\sum_i L(p_i, E_i, E)}{\sum_i L(1, E_i, E)}$$

where the denominator serves to normalize our result. The smoothing parameter η is chosen to give us reasonably smooth functions. The effect of this smoothing algorithm is shown in Fig. 3.3.

We now average over many samples for each disorder and lattice size. The results of this smoothing are shown in Fig. 3.4.

We now evaluate these functions at the Fermi energy (at 2/3 filling), and plot the results vs. N (Fig 3.5). We multiply P by N anticipating that systems with delocalized states at the Fermi energy will exhibit (nearly) zero slopes for NP, while systems with localized states will show obviously non-zero slopes. None of the curves in Fig. 3.5 are completely constant, but one could believe that the

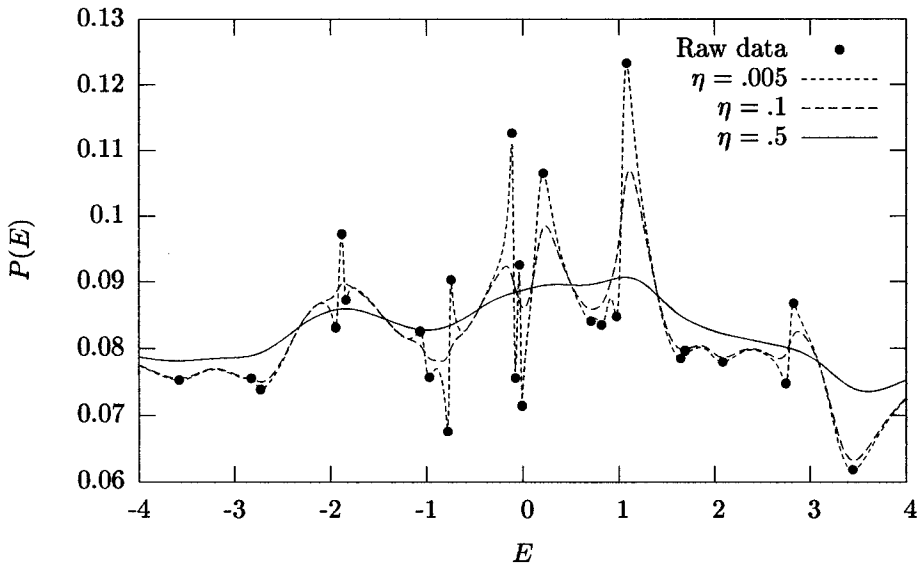

Figure 3.3: Effect of smoothing the inverse participation ratio for a 5×5 system (chosen to reduce the amount of data in the figure).

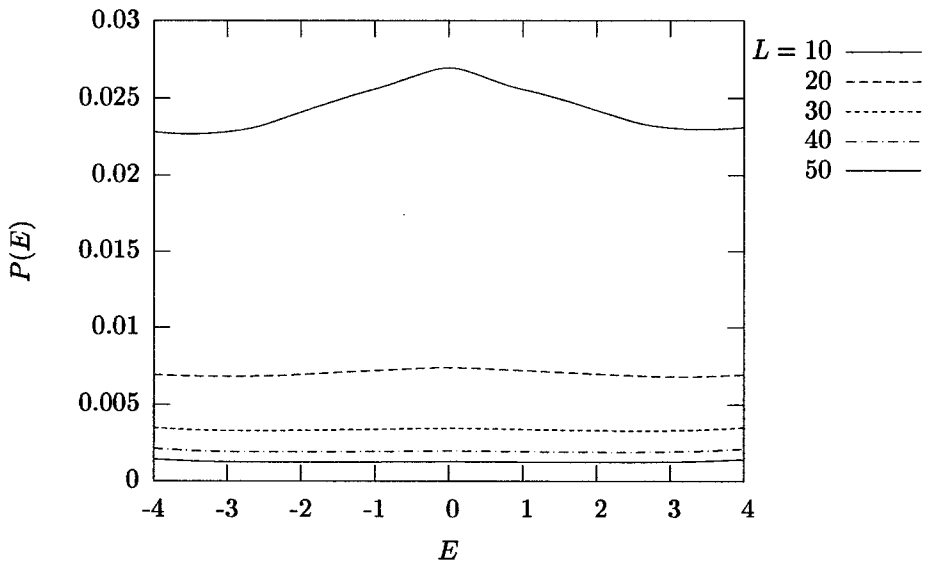

Figure 3.4: Inverse participation ratios for different sizes of system as a function of energy. These systems all had a disorder parameter $D = 1$.

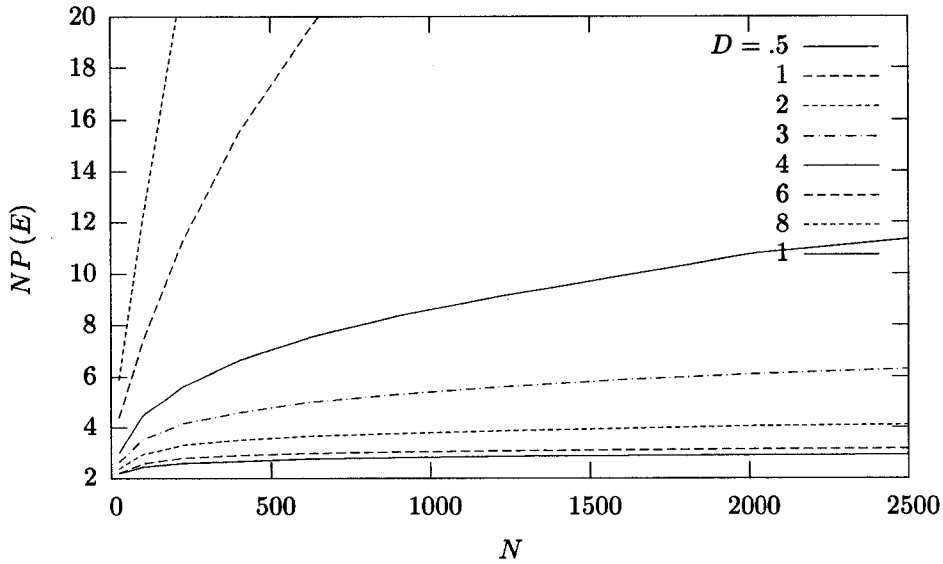

Figure 3.5: Inverse participation ratio at the Fermi energy (for 2/3 filling), multiplied by N, as a function of the number of states (i.e., lattice sites) in the system.

curves for $D = 0.5$, 1, and 2 are leveling off, and therefore represent delocalization. Clearly, $D > 4$ shows localization; $D = 3$ and 4 are debatable. We will avoid any debate by erring on the side of caution, and restricting our discussion of the Anderson impurity model to $D < 2$.

3.5 Longitudinal conductance

For periodic boundary conditions, σ_{xx} has much the same shape predicted by the Drude model. However, using open boundaries changes the height of the Drude peak and shifts its location to a non-zero frequency, as shown in Fig 3.6. We now face one of the fundamental challenges of this work: extrapolating to $\sigma_{xx}(\omega = 0)$ with fixed boundary conditions in the thermodynamic limit.

We begin by noting that the location of the conductivity peak, ω_{peak}, smoothly approaches zero as the size of the system is increased, as shown in Fig. 3.13. We will take $\sigma_{xx}(\omega = \omega_{\text{peak}})$ to be the value most representative of the thermodynamic limit, and will use this value when taking further limits in L and η. One can consider this as having taken a limit in ω, although this is really part of taking the L limit. As mentioned in Section 2.7, we will write $\sigma_{xx}(\omega = \omega_{\text{peak}})$ as $\sigma_{xx}(D, L, \eta)$. (The band filling F is not a parameter here, as all of our work with these systems was done at 2/3

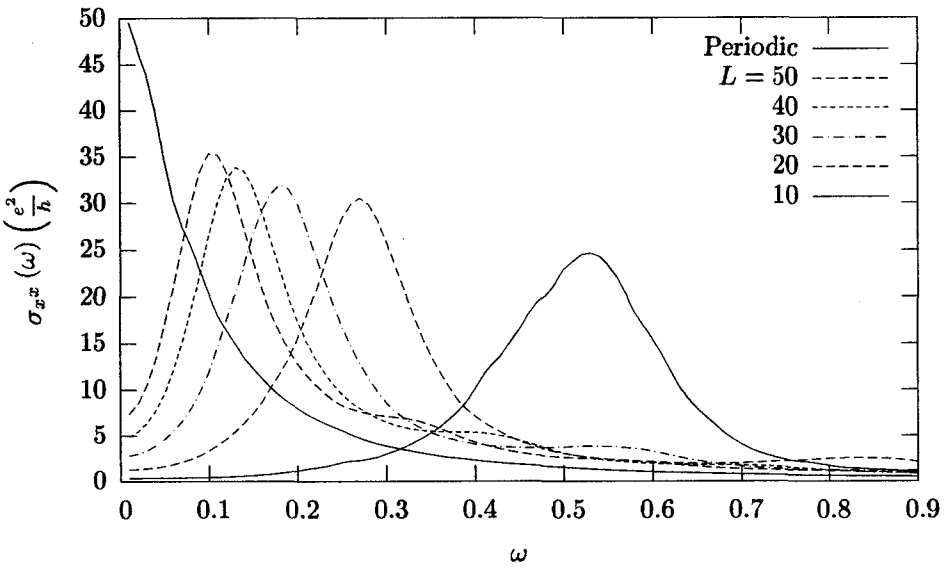

Figure 3.6: $\sigma_{xx}(\omega)$ for a 50×50 system with periodic boundaries, and for open-boundary systems of several sizes. All systems have $L = 50$, $D = 1$ and $\eta = .01$.

filling.)

Now, in both cases (periodic and fixed), the height of the peak is dependent on the value of η. We need, then, to take two limits: $L \to \infty$ and $\eta \to 0$.

3.5.1 The $L \to \infty$ limit

We extrapolate to $L \to \infty$ by fitting $\sigma_{xx}(D, L, \eta)$ to a well-behaved function; the function

$$ae^{-\frac{b}{L}} \tag{3.1}$$

(with a and b the fitting parameters) seems to fit our data well[1].

This extrapolation procedure raises an important point: what sort of error should we report for these extrapolated values? One solution is to use the error reported by the curve-fitting procedure (calculated in the usual way). However, this will not take into account the statistical error from taking the ensemble average. Using a weighted curve fit, which would take statistical error into

[1]This function was suggested by examining log-log plots of the data; it is admittedly ad-hoc. However, the leading behavior $(1/L)$ is physically plausible, since the corrections due to surface effects should, in general, be related to the ratio of surface area to volume.

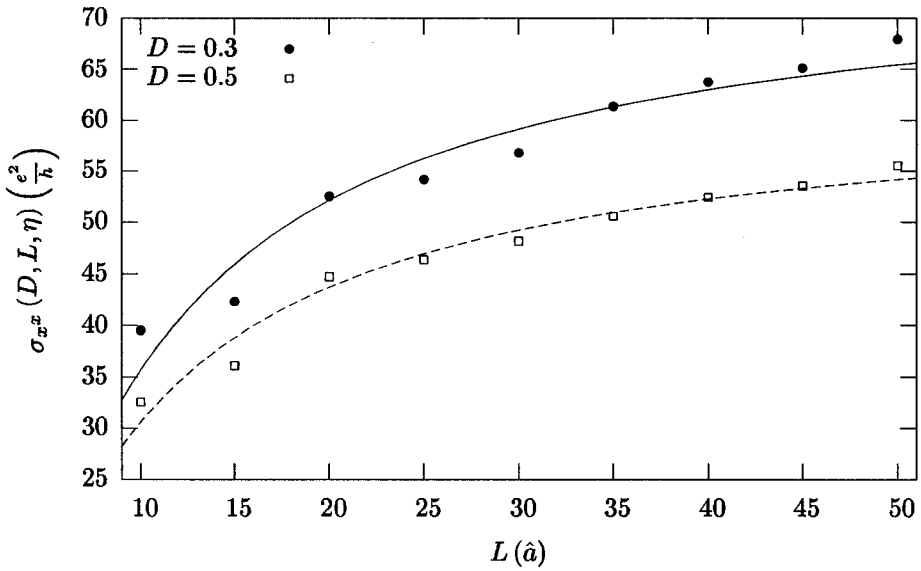

Figure 3.7: System size extrapolation for two disorder levels; in both cases, $\eta = 0.02$. The lines (solid for $D = 0.3$, dashed for $D = 0.5$) are the results of fitting to Eq. (3.1).

account, produces very unsatisfactory results: since smaller systems are so much faster to produce results for, we generated significantly more data for them. They therefore tend to have smaller standard error, and dominate the results of a weighted fit. Using the standard deviation, instead of the standard error, for a weighted fit does not work either; smaller systems have much larger standard deviations, and the fitting results are dominated by larger systems.

In fact, the statistics of these systems is a bit problematic. The distribution in $\sigma_{xx}(D, L, \eta)$ turns out not to be Gaussian when the ensemble average of σ_{xx} is small (as it is for the smaller systems), and is not completely Gaussian even for our larger systems; see Fig. 3.8. It was this odd statistical behavior that lead us to investigate the interesting phenomena of "universal conductance fluctuations" (UCFs). To make a long story short, the unpleasant statistical behavior of our results is an expected property of these two-dimensional models. The phenomenon of UCFs, and what it means for our data, is discussed at length in Chapter 4. (The statistics of the particular data set plotted in Fig. 3.7 are not so bad; the standard error is less than 1% for all the data points shown. This is not generic, however.)

So, we feel the need to indicate more "uncertainty" about our results than would be indicated by either the error estimates from the curve fitting, or the usual statistical methods. Therefore,

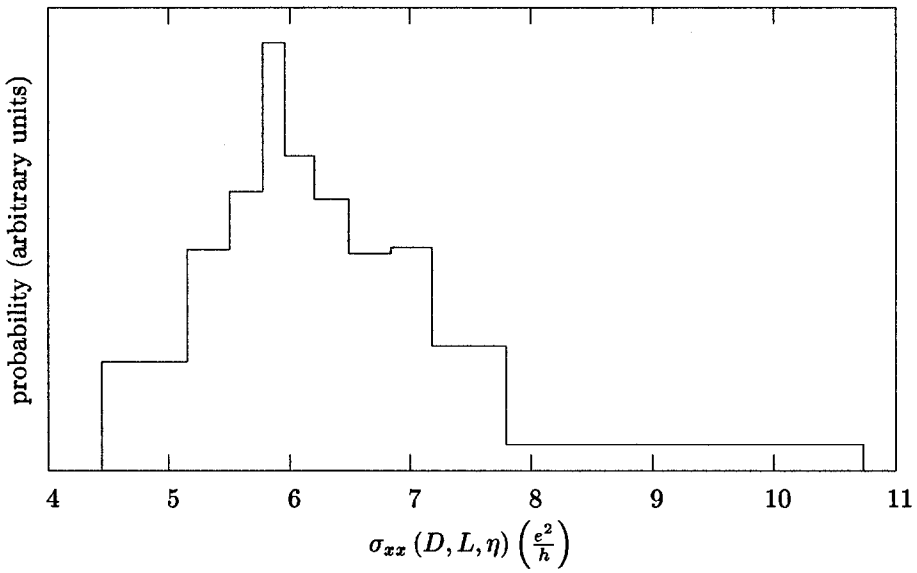

Figure 3.8: Distribution of σ_{xx} for $L = 10$, $D = 0.5$, and $\eta = 0.01$.

we will inflate the stated uncertainty in the result of the $L \to \infty$ extrapolation, making it big enough to account for statistical error and extrapolation (i.e., fitting) error, with a bit left over. For the L extrapolation in Fig. 3.7, the statistical uncertainty is less than 1%; the curve fitting uncertainty about 3%; so reporting an uncertainty of 5% is probably conservative enough. This gives the result of taking $L \to \infty$ of the data shown in Fig. 3.7 as $\sigma_{xx}\,(D = 0.3, \eta = 0.02) = 9.5 \pm 0.5$ and $\sigma_{xx}\,(D = 0.5, \eta = 0.02) = 7.8 \pm 0.4$.

3.5.2 The $\eta \to 0$ limit

We now turn to taking the limit as $\eta \to 0$. we commented during the derivation of the working KG formula that the correct thermodynamic limit is found by letting the system size go to infinity *first* and letting $\eta \to 0$ *second*, since $\eta \to 0$ results in a discrete set of delta functions. (In a real system, of course, all kinds of other effects — mainly non-zero temperature — blur the delta functions.) If we took the limit $\eta \to 0$ first, we would reduce σ to a series of delta functions, which does not accurately describe macroscopic systems.

However, if we restrict ourselves to using only "legitimate" values of η (roughly, η greater than the spacing between delta functions), we should be able to obtain a reasonable extrapolation to

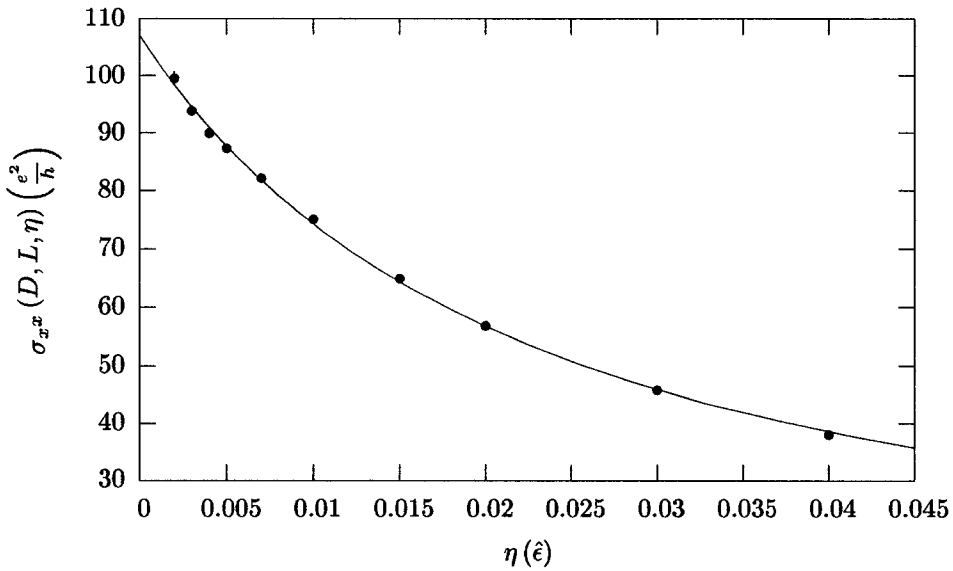

Figure 3.9: $\sigma_{xx}(D, L, \eta)$ vs. η for a 30×30 system with a disorder of $D = 0.3$. The points are the results of averaging over ~ 100 systems; the error bars are the standard error, and (for most points) are smaller than the symbols.

$\eta = 0$. In other words, we can switch the order of the limits in η and system size, provided we extrapolate based on data where both parameters are legitimate. (We should note that, in fact, we can generally use values of η smaller than one might expect, *if* we have a large enough ensemble to average over.)

Fig. 3.9 shows an example of fitting $\sigma_{xx}(D, L, \eta)$ vs. η to the function $1/(a\eta + b)$. We justify this fitting function on the basis that the η dependence of σ_{xx} is

$$\frac{\eta}{(\omega + \Delta\epsilon)^2 + \eta^2}$$

[see (2.7)] so we might expect the leading behavior at large η to be $1/\eta$. (By similar reasoning, we expect the large η behavior of σ'_{xy} to go as $1/\eta^2$, which indeed turns out to be a good fit; see Section 3.6.) Clearly, the fit in η is *much* better than the fit in L was, leading to much smaller fit errors ($< 1\%$). The statistical error tends to grow with decreasing η; generally, it is less than 3% or so. As we did in the previous section, we will inflate this to a comfortable, conservative 5% uncertainty estimate. Applying this limiting procedure to the data shown in Fig. 3.9, we get

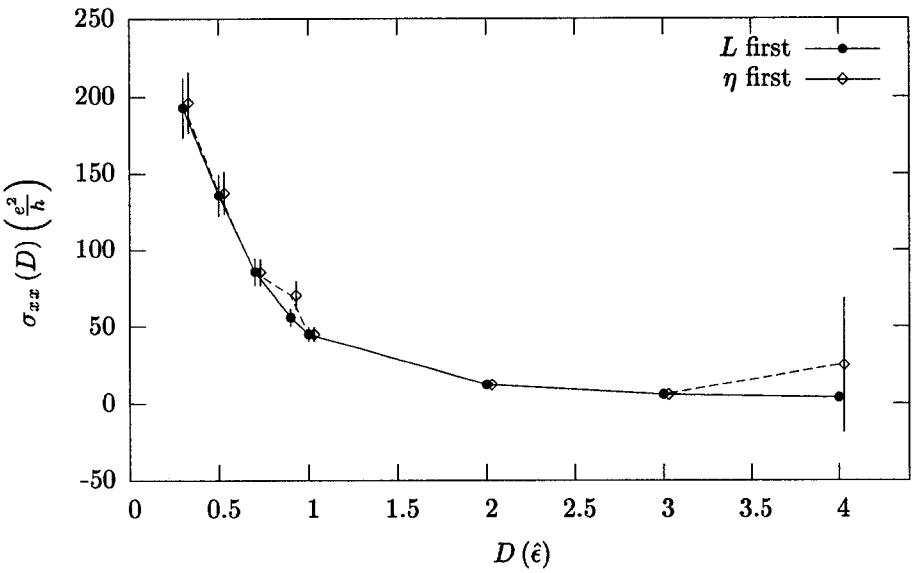

Figure 3.10: Comparison of the two extrapolation procedures, limiting L then η, and limiting η then L. The symbols and error bars for the "η first" data have been offset slightly for clarity.

$\sigma_{xx}(D = 0.3, L = 30) = 13.4 \pm 0.7$.

We note that for these systems, the range in η from .002 to .04 seems to be reasonable; we do not have data outside this range, simply because we did not explore that part of parameter space. However, for the A_3C_{60} systems, we did obtain data for "bad" η values; see Fig. 5.7. We emphasize that, for the purposes of extrapolating $\eta \to 0$, it is important to find the range of η values that are valid.

3.5.3 Comparison of limiting procedures

If it is indeed the case that we can take the limits in L and η in any order we wish, then taking both limits should yield the same results, regardless of which limit is taken first. The limits agree, as Fig. 3.10 shows. Since both procedures are valid, we will usually take the $\eta \to 0$ limit first, as the η parameter is of less interest.

As noted above, the fit to $(a\eta + b)^{-1}$ is much better than the fit to $a\exp(-b/L)$. Since the second extrapolation ignores the uncertainty in the result of the first, the L,η order produces much smaller uncertainties than the η,L does. We put a lower limit of 10% on the results of both procedures; the

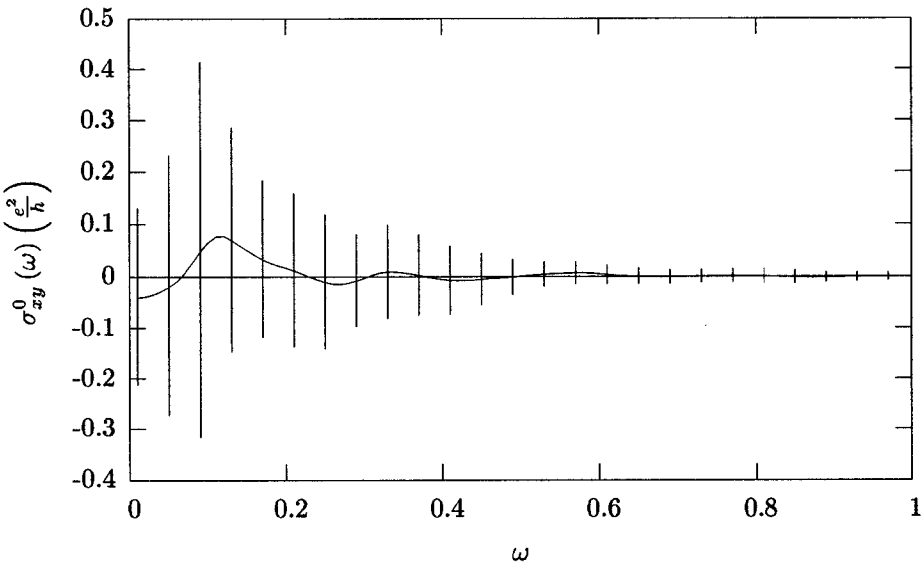

Figure 3.11: $\sigma^0_{xy}(\omega)$ for a 50×50 system with $D = 1$ and $\eta = 0.04$. Here we have averaged over 15 systems, and the error bars represent one standard deviation; they are only shown for every fourth point to improve readability.

uncertainty in two points ($D = .9$ and 4) resulting from taking the L limit second is larger than that, and is reported unchanged.

3.6 σ_{xy} and R_H

As expected, in zero magnetic field, $\sigma^0_{xy}(\omega)$ averages to zero for all ω (see Fig. 3.11). Also as expected, $\sigma'_{xy}(\omega)$ does *not* average to zero; see Fig. 3.12. Note that we are using a larger value of the smoothing parameter η than we did for σ_{xx}; this will be necessary in general for σ'_{xy} data.

As with the longitudinal conductivity, we need to extrapolate our σ'_{xy} results to $\eta \to 0$ and $L \to \infty$. However, in this case, we cannot examine the results from periodic systems to give us any hints, so it is not immediately clear how the $L \to \infty$ extrapolation should be done. However, the behavior of $\sigma'_{xy}(\omega)$ with system size is similar to that of $\sigma_{xx}(\omega)$, suggesting a comparison of peak locations. Fig. 3.13 shows the locations of the conductivity peaks for $\sigma_{xx}(\omega)$ and $\sigma'_{xy}(\omega)$. The close tracking of $\sigma_{xx}(\omega)$ and $\sigma'_{xy}(\omega)$ peak locations suggests that we use the peak $\sigma'_{xy}(\omega)$ value as the value most representative of the thermodynamic limit, as we did for σ_{xx}. Alternately, we could use

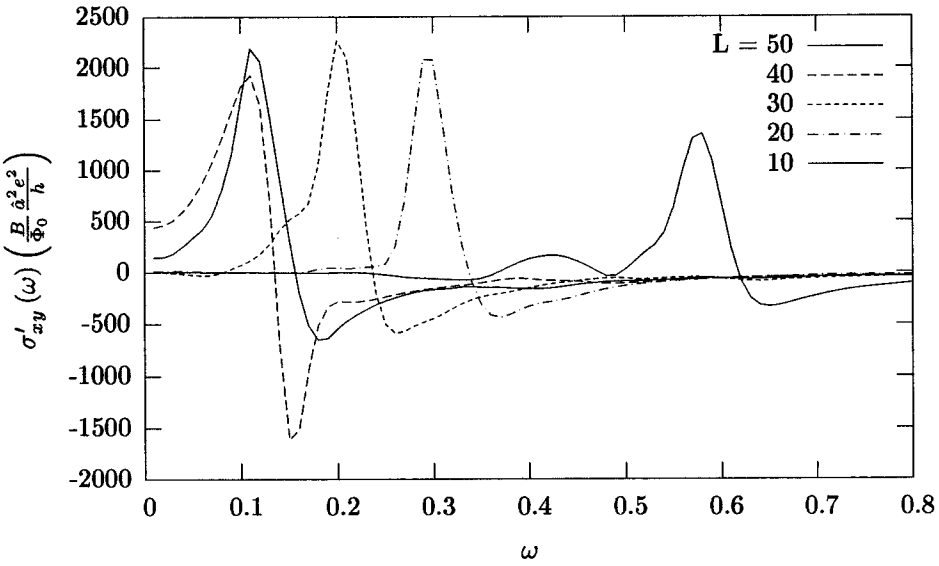

Figure 3.12: $\sigma'_{xy}(\omega)$ for $D = 0.5$ and $\eta = 0.03$, for several system sizes.

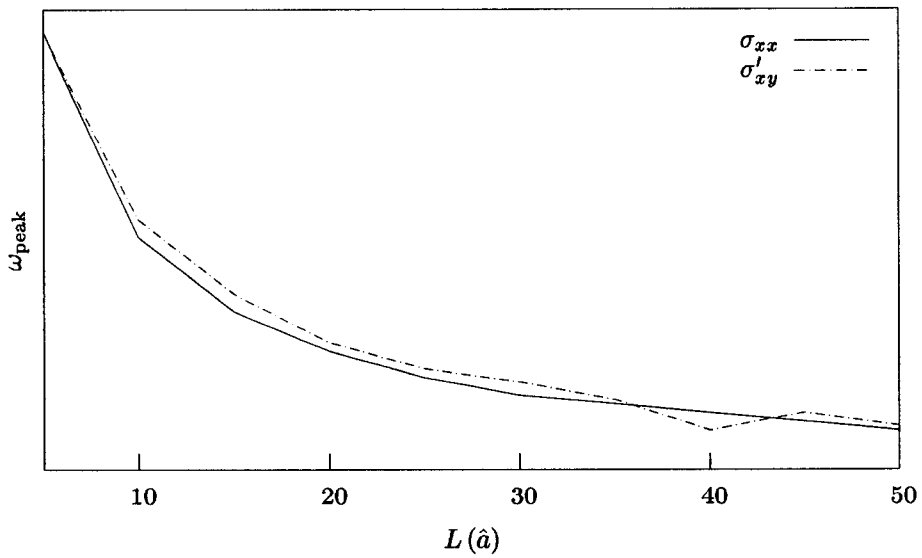

Figure 3.13: Peak location for both $\sigma_{xx}(\omega)$ and $\sigma'_{xy}(\omega)$.

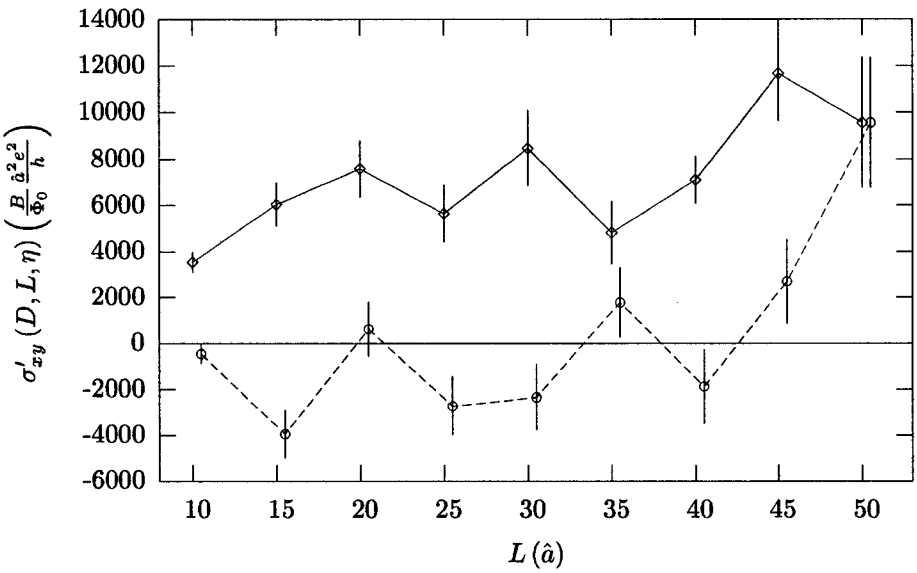

Figure 3.14: Results for $\sigma'_{xy}\,(D,L,\eta)$ using two extrapolation methods: using the maximum in $\sigma'_{xy}\,(\omega)$ (solid line), or taking the value at the location of the $\sigma_{xx}\,(\omega)$ peak (dashed line). The latter data has been offset in the x-direction slightly to make the error bars visible.

the location of the $\sigma_{xx}\,(\omega)$ peak to define ω_{peak}, and take $\sigma'_{xy}\,(\omega = \omega_{\text{peak}})$ as the value we want.

It turns out that the latter method is very unsatisfactory. The narrowness of the peak in $\sigma'_{xy}\,(\omega)$, and the negative values usually found on one or both sides of it, causes a slight offset in peak locations to lead to erroneous results; see Fig. 3.14. We know that the Hall coefficient should be positive in these systems, so this procedure is clearly wrong.

So, we will proceed as we did for $\sigma_{xx}\,(\omega)$: we take limit of $\sigma'_{xy}\,(\omega = \omega_{\text{peak}})$ as $L \to \infty$ and $\eta \to 0$. These limits are done in much the same way they were for σ_{xx}. As for σ_{xx}, the $\eta \to 0$ extrapolation is much more obvious than the size extrapolation. We expect to see $1/\eta^2$ behavior, as that is the behavior of each term in the KG formula [see (2.8)]; and this is indeed the case, for "valid" values of η. Fig. 3.15 shows the excellent fit to $(a\eta + b)^{-2}$. As before, we put a minimum of 5% uncertainty on the result.

The size extrapolation is a bit of a problem. Fig. 3.16 shows the L dependence of $\sigma'_{xy}(D,L)$. Clearly, there is no obvious way to extrapolate to $L \to \infty$, unless we want to say that for the larger D values, it is constant. We will have to settle, then, for simply taking the value at the largest system we can treat (50×50) as being representative of the thermodynamic limit. This is, perhaps,

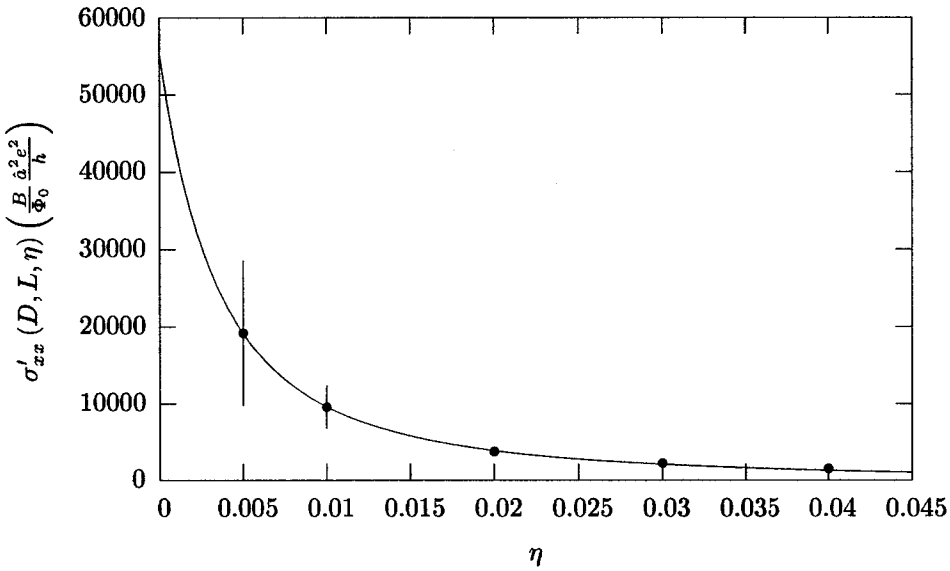

Figure 3.15: $\sigma'_{xy}(D,L,\eta)$ vs. η for 50×50 systems with $D = 0.5$. The extrapolated $\eta = 0$ value is 6900 ± 350. The error bars are statistical.

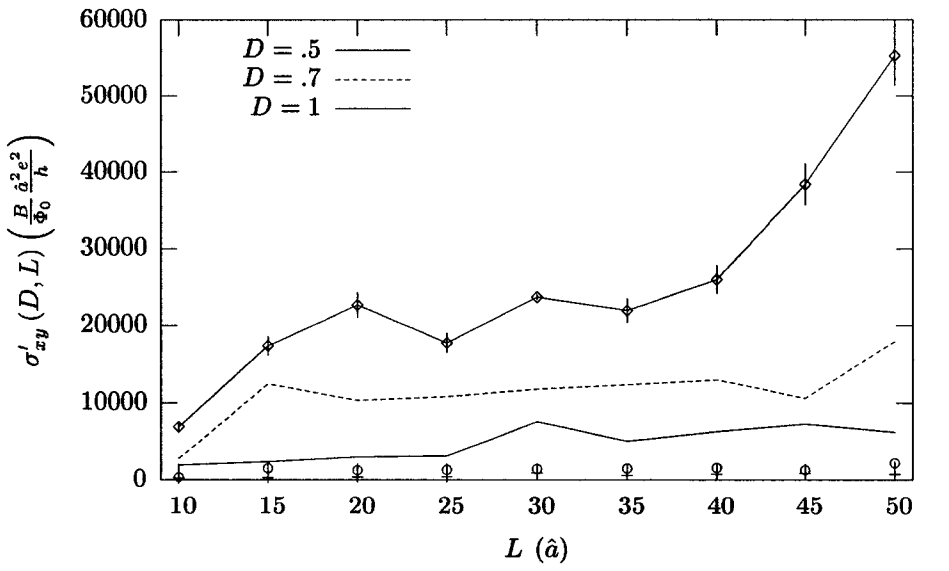

Figure 3.16: $\sigma'_{xy}(D,L)$ vs. L for several values of D.

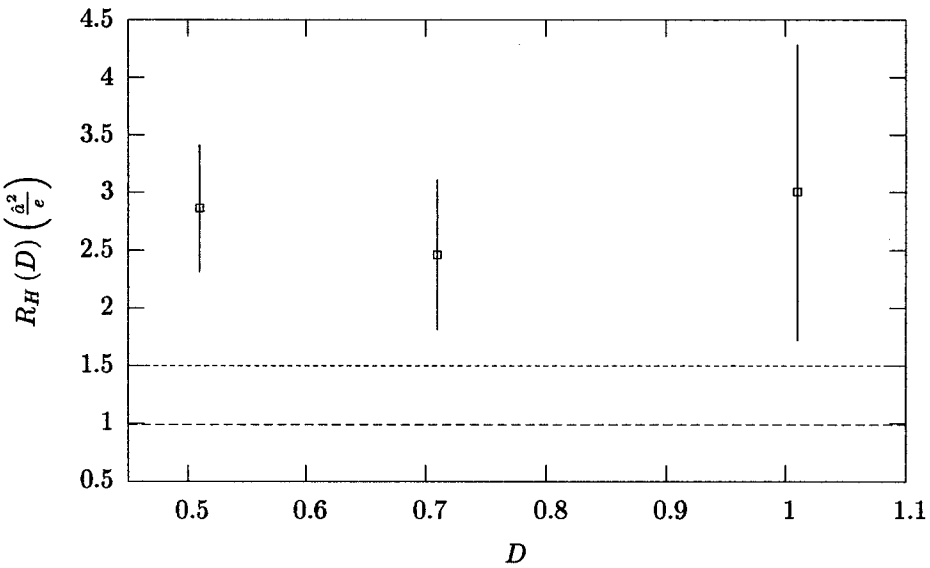

Figure 3.17: R_H as a function of disorder. We have "extrapolated" in size by setting $L = 50$. The values of R_H calculated by other methods (0.989 via Appendix B, and 1.5 via the classical Drude result) are shown as dashed lines.

not so unsatisfying for $D = .7$ and 1; but for $D = .5$ we would like to do better. ($D = 0.3$ is not shown, as it is "noisy" to the point of showing no particular trend at all; I suspect we simply need *much* more data for this disorder level.)

As unsatisfying as these results are, when we calculate R_H from them, the results are quite satisfactory. Using $L = 50$ for both $\sigma_{xx}(D, L)$ and $\sigma'_{xy}(D, L)$ and computing R_H produces results shown in Fig. 3.17, which compare well with the clean-system approximation discussed in Appendix B, differing by factor of ~ 3 or less. We can also compare with the Drude model result, $R_H = 1/ne$, using $n = 2/3$ (the hole density). This gives $R_H = 1.5\,\hat{a}^2/e$, which is also in good agreement with our KG results.

Chapter 4

Universal Conductance Fluctuations

> For thousands more years, the mighty ships tore across the empty wastes of space and finally dived screaming on to the first planet they came across — which happened to be the Earth — where due to a terrible miscalculation of scale the entire battle fleet was accidentally swallowed by a small dog.
>
> -Douglas Adams [2]

4.1 Introduction

It has been known for some time that very small conductors exhibit the phenomenon of "universal conductance fluctuations" (UCFs), first noticed in small wires and rings as a function of magnetic field. These fluctuations are not random, but are reproducible, time-independent fluctuations in σ_{xx} as a function of magnetic field [26]. UCFs are a general property of "mesoscopic" metals. In the present context, macroscopic systems can be defined as those in which electron transport is diffusive, and whose electrical properties are determined by only a few characteristics such as composition and temperature; microscopic systems display ballistic electron transport and sample-specific electrical properties. Mesoscopic systems are somewhere in between: they display diffusive electron transport, but have sample-specific properties.

For our purposes, mesoscopic systems can defined to be those with dimensions L that are larger than the elastic mean-free path ℓ, but smaller than both the inelastic mean-free path $\ell_{\rm in}$ and the localization length ξ. Electron transport in these systems then involves multiple, coherent scattering events, leading to interference patterns: the current density at a given location will depend sensitively on the phases of all the scattered waves reaching it. A familiar example of such a phenomenon is a laser speckle pattern, generated by shining coherent light through a random medium; in fact, the current density in a mesoscopic conductor has been shown to be completely analogous to a speckle pattern [24, 26]. The conductivity of the sample is sensitively dependent on the details of the interference pattern created by the scattering events. Thus, anything which changes the interference pattern (such as changing the magnetic field, the Fermi energy, or the impurity configuration) should produce statistically identical changes in the conductivity; this important "ergodic" hypothesis was first proposed by Lee and Stone [26]. These fluctuations should be of order e^2/h regardless of the conductivity, size of the sample, disorder level, etc., provided the system remains a mesoscopic conductor; hence the term "universal conductance fluctuations". We will denote the magnitude of these fluctuations by $\Delta\sigma_{xx}$. A variety of theoretical calculations [26, 27, 28, 29, 30] of $\Delta\sigma_{xx}$, which are generally field-theoretical and based on perturbation in $(k_F\ell)^{-1}$, have found $\Delta\sigma_{xx}$ to be between 0.6 and 1 e^2/h; a variety of numerical calculations [10, 31, 32] produce similar, but more widely varying, results. The dimensionality of the system has some effect on $\Delta\sigma_{xx}$, but typically only at about the 30% level.

The statistics of σ_{xx} in the presence of UCFs has interesting implications for our work on the Anderson impurity model. In two-dimensional mesoscopic systems at zero temperature, the conductivity is not a self-averaging quantity [26, 28]; fluctuations due to different impurity configurations may persist to almost arbitrarily large systems. (In one dimension, the situation is even worse: not only is the conductivity non-self-averaging, it is statistically pathological [10, 26].) The statistics of σ_{xx} are expected to be Gaussian for $\sigma_{xx} \gg e^2/h$, but to have highly non-Gaussian shape if $\sigma_{xx} \sim e^2/h$ [29]. We saw similar behavior in our Anderson models, which typically have a conductivity greater than, but not *much greater* than, e^2/h.

In this Chapter, we present some evidence that we are, indeed, seeing signs of UCFs in our two-dimensional Anderson models, which is why there are larger sample-to-sample variations in σ_{xx}

than we had expected. We emphasize that investigating $\Delta\sigma_{xx}$ was not one of our research goals, and that we will not say anything new about it here. The only new physics we will present is some evidence for the existence of similar fluctuations in σ'_{xy}, a subject that has not (to our knowledge) been examined previously.

4.2 Mean free path

We need to find a rough estimate of the mean free path for our two-dimensional systems, so we can determine whether or not we are in the mesoscopic regime. We start with a result from Boltzmann transport theory (see Appendix B)

$$\sigma_{xx} = \frac{1}{2} e^2 v_F^2 \tau \mathcal{N}(E_F)$$

and noting that the mean free path $\ell = v_F \tau$, we can solve for ℓ to get

$$\ell = \frac{2}{e^2} \frac{\sigma_{xx}}{v_F \mathcal{N}(E_F)}$$

or, in dimensionless quantities,

$$\begin{aligned} \ell &= \frac{2}{e^2} \frac{\frac{e^2}{\hbar}\bar{\sigma}_{xx}}{\frac{\hat{a}\hat{\epsilon}}{\hbar}\bar{v}_F \frac{\bar{\mathcal{N}}(E)}{\hat{a}^2\hat{\epsilon}}} \\ &= \frac{\hat{a}}{\pi} \frac{\bar{\sigma}_{xx}}{\bar{v}_F \bar{\mathcal{N}}} \end{aligned}$$

Appendix B discusses v_F and obtains results for v_F averaged over the Fermi surface. At 2/3 band filling, $E_F \sim 0.786\hat{\epsilon}$, $\langle \bar{v}_F \rangle \sim 2.282$, and $\mathcal{N}(E_F) = 0.307/\hat{a}^2\hat{\epsilon}$ (see Fig. 3.1); these values give $\ell = 0.454\bar{\sigma}\hat{a}$.

Using extrapolated values of σ_{xx} from Fig. 3.10, we find the mean free path as a function of disorder, shown in Fig 4.1.

For a system to be mesoscopic, it must have $\sigma_{xx} \gg e^2/h$ and $L > \ell$; we need to choose combinations of D and L that put us in this regime. There is no clear way to decide, for example, how *much* bigger than e^2/h the conductivity must be, so at this point, we must make some educated guesses

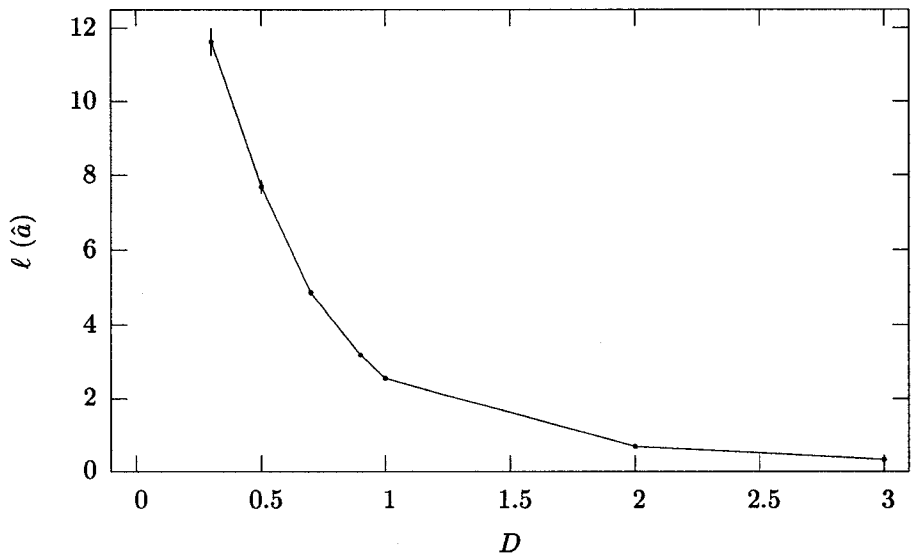

Figure 4.1: Mean free path as a function of D.

about where in D and L space the mesoscopic regime resides. Based on Fig. 3.10, we will restrict ourselves to $D \leq 1$, at which disorder $\sigma_{xx} \simeq 45\, e^2/h$. We also need an electron to scatter at least once as it crosses the sample. Let us demand (on average) two scatterings, just to be safe; Fig. 4.1 indicates using, say, only $L \geq 30$, which should produce two scattering events at $D = 0.3$, the lowest disorder value we treat. We should emphasize that these choices are only first estimates.

4.3 $\Delta\sigma_{xx}$

Xie and Das Sarma [32] calculated $\Delta\sigma_{xx}$ for long thin strips, using the same Anderson model we used in Chapter 3 and a recursive implementation of the Kubo-Greenwood formula. We performed computations with the same lattices and found nearly identical results, although our parameters were slightly different. We take this result as evidence (not necessarily conclusive) that our KG approach can produce UCFs in mesoscopic finite-clusters.

We then examined $\Delta\sigma_{xx}$ in the $L \times L$ systems discussed in Chapter 3. Again, all of our calculations were done at 2/3 band filling.

We must first address the issue that $\Delta\sigma_{xx}$ depends on the value of η. It is not entirely clear if

we should take the $\eta \to 0$ limit before or after we examine the statistics of the ensemble and find $\Delta\sigma_{xx}$. That is, should we find $\Delta\left(\lim_{\eta\to 0}\sigma_{xx}\right)$ or $\lim_{\eta\to 0}\left(\Delta\sigma_{xx}\right)$? Or, indeed, should we be taking $\eta \to 0$ limits at all? Although in both cases we can fit to a curve (as we did in Chapter 3), it is not clear that this is an improvement. We do not have any a-priori guesses about what functional form the fluctuations in σ should have, so any extrapolation based on a fitting function (as we used for σ) would be purely ad-hoc. Therefore, we decided to sidestep the entire issue and simply choose an η value that seemed reasonable.[1] We *do not* expect to obtain a value of $\Delta\sigma_{xx}$ that agrees with any other calculation (except by accident), but we *do* expect to find universal behavior in $\Delta\sigma_{xx}$.

UCFs in the longitudinal conductivity should be constant with respect to cluster size (providing the cluster is mesoscopic), and should also be constant as a function of the disorder parameter. For our open-boundary systems, these behaviors are, at best, only partially present. Fig. 4.2 shows that even at the largest cluster size that we can treat (50×50), there is still size dependence to $\Delta\sigma_{xx}$. Although we have shown a possible fit that one could use to extrapolate to $L \to \infty$, it is a fit to an ad-hoc curve, so we do not take it too seriously; the curves are more useful as a guide to the eye.

Figure 4.3 shows $\Delta\sigma_{xx}$ as a function of disorder for 50×50 systems (as we do not have great faith in our ability to extrapolate to $L \to \infty$); there is some disorder dependence here, although not as much as it might seem; $\Delta\sigma_{xx}$ changes by about 30% as D varies between 0.3 and 1, while σ_{xx} varies by a factor of roughly 5 over the same range (see Fig. 3.10).

To what do we attribute these almost-but-not-quite mesoscopic results? There are two possibilities. First, we may not be as mesoscopic as we thought; Fig. 4.2 indicates that maybe our systems are in some sense too small to be truly mesoscopic; perhaps if we could obtain results for larger systems we would see size-independent fluctuations. However, the mean free path as shown in Fig. 4.1 implies that this should not be the case; an electron crossing a 50×50 $D = 1$ system ought to have on the order of 15 elastic scatterings, which ought to be enough to make the system mesoscopic. More likely is the second option: we are being foiled by our boundary conditions.

Virtually every other numerical approach we have found uses "perfect" (i.e., non-disordered) leads on each side of the sample, and use a recursive Kubo approach. However, we are using open, not periodic, boundaries in x, with no "perfect leads" anywhere: we were trying to perform calculations

[1] All results in this chapter were obtained with $\eta = 0.01\hat{\epsilon}$.

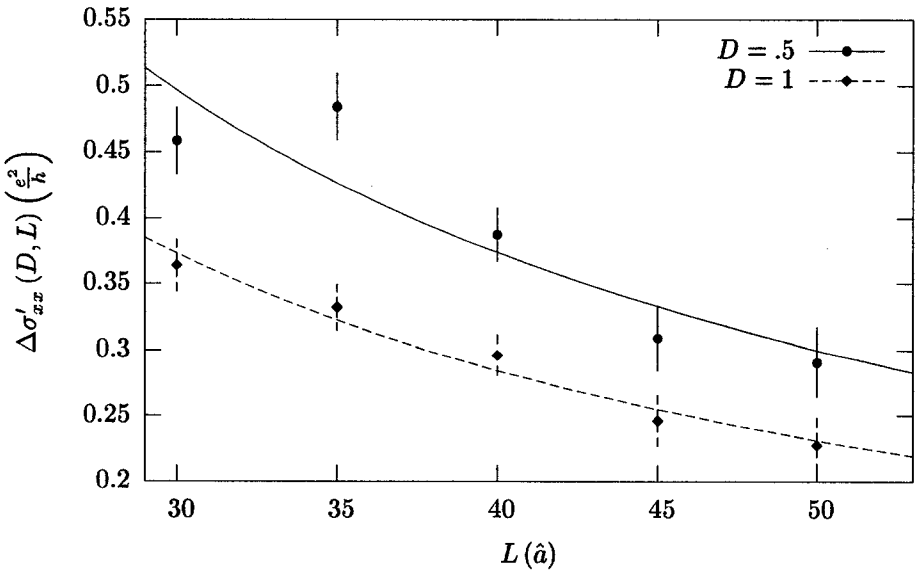

Figure 4.2: $\Delta\sigma_{xx}$ as a function of system size. The error bars represent the statistical standard error (from averaging over samples). The curves are fits to $a + 1/(bL)$

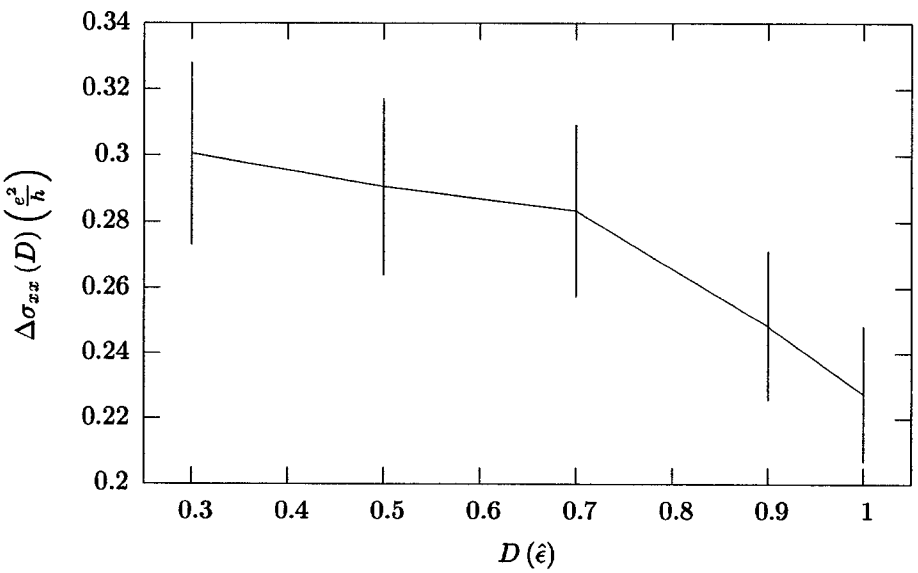

Figure 4.3: $\Delta\sigma_{xx}\,(D, \eta = .01)$ for 50×50 clusters with open boundaries.

analogous to those for our A_3C_{60} models. Given the strong effect of imposing open boundaries (as compared to periodic boundaries; see Fig. 3.6) we should not be surprised to find strong effects in $\Delta\sigma_{xx}$ due to these boundary conditions. If anything, one might expect the increased finite-size effects to make the systems behave as if they were in some sense "smaller" — and therefore, less mesoscopic — than their sizes and mean free paths might indicate.

We conclude, then, that while we see some evidence that our systems are mesoscopic, we are probably not *very* mesoscopic; that our results may not be completely representative of truly mesoscopic systems; and that our results in the next section should be taken only as indications that universal fluctuations in $\Delta\sigma'_{xy}$ *may* exist.

4.4 $\Delta\sigma'_{xy}$

To the best of our knowledge, fluctuations in off-diagonal elements of the conductivity tensor have not been studied; their only mention in the UCF literature that we are aware of is Xiong, Read, and Stone [30], who examined the relationship between $\Delta\sigma_{xx}$ and σ_{xy}/σ_{xx}. We therefore took the opportunity to examine our off-diagonal data for any signs of universal behavior. Fluctuations in σ^0_{xy} are not of interest, because this quantity self-averages to zero, so we examine $\Delta\sigma'_{xy}$. As before, all results are at 2/3 band filling, and we will not do any $\eta \to 0$ extrapolation; all of the following results will use $\eta = 0.01\hat{\epsilon}$.

Figure 4.4, which plots $\Delta\sigma'_{xy}$ as a function of system size, hints that the $\Delta\sigma'_{xy}$ *might* possibly be lattice size independent, although it is hard to be sure. Investigating further, we found more convincing results involving the ratio

$$\gamma = \frac{\Delta\sigma'_{xy}}{\sigma'_{xy}}$$

which seems to be roughly constant as a function of both system size L and disorder D, as shown in Fig. 4.5. These results are striking, as they indicate that when examining an ensemble of systems, the variations in σ'_{xy} will be on order of the mean!

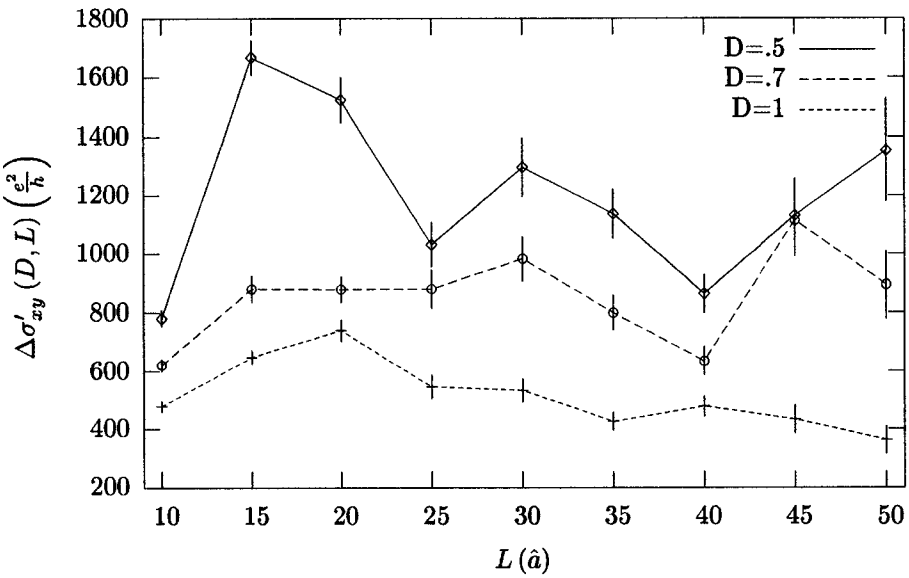

Figure 4.4: $\Delta\sigma'_{xy}(\eta = .01)$ as a function of system size in $L \times L$ systems. The error bars are statistical.

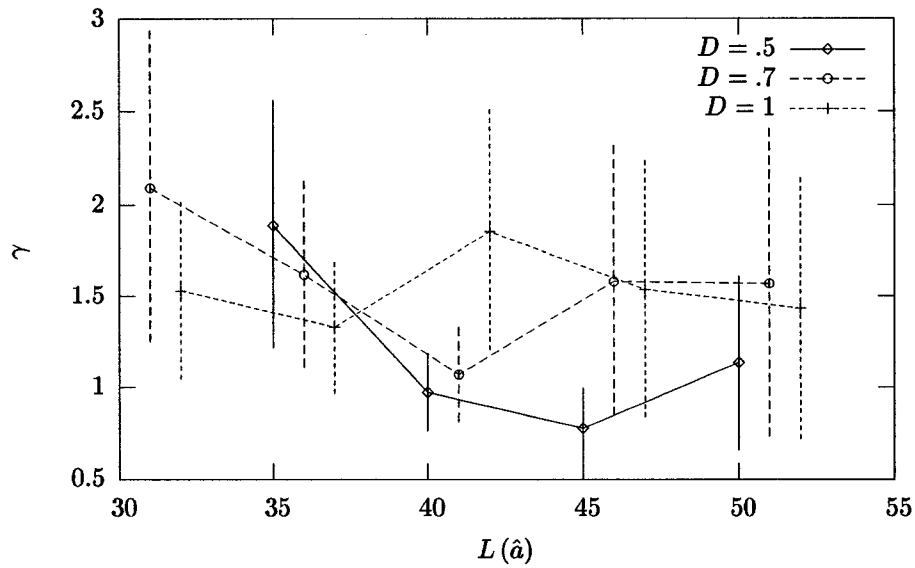

Figure 4.5: γ as a function of L for several values of D. The data for $D = 0.7$ and $D = 1$ are offset slightly in the x direction, to make the error bars more visible.

4.5 Conclusions

Although there is evidence that our systems are too small to show truly mesoscopic behavior, they do show evidence of mesoscopic phenomena such as universal conduction fluctuations, that is, $\Delta\sigma_{xx}$. We have also found evidence of universal behavior in the ratio

$$\gamma = \frac{\Delta\sigma'_{xy}}{\sigma'_{xy}}$$

which is, to the best of our knowledge, the first evidence of universal conductance fluctuations in the off-diagonal elements of the conductivity tensor.

We emphasize, however, that this evidence is rather tenuous, and should be taken more as a direction for future research than as a solid result in and of itself. Which leads us to...

4.6 Directions for Future Research

Given the time and computational resources, it would not be difficult to use our KG formulation with Anderson models that would very likely be more appropriate for studying UCFs. In particular, using periodic boundaries in x would still allow for the magnetic field to be incorporated, probably improving investigations into $\Delta\sigma'_{xy}$. In addition, the universality of γ should be checked by varying E_F for a given sample; if it really is universal, it should satisfy (in some fashion) Lee and Stone's ergodic hypothesis. Finally, we point out that correlations in $\Delta\sigma_{xx}$ and $\Delta\sigma'_{xy}$ should be investigated.

Chapter 5

Alkali Fullerides

> It is an important and popular fact that things are not always what they seem. For instance, on the planet Earth, man had always assumed that he was more intelligent than dolphins because he had achieved so much — the wheel, New York, wars and so on — while all the dolphins had ever done was muck about in the water having a good time. But conversely, the dolphins had always believed that they were far more intelligent than man — for precisely the same reasons.
>
> -Douglas Adams [2]

5.1 Overview of the "standard model" of the electronic properties of A_3C_{60}

In Chapter 1 we presented an overview of A_3C_{60} and its electronic properties. Before continuing, let us briefly revisit this topic.

The discovery [33, 34, 35] of metallicity and remarkably high-temperature superconductivity in the A_3C_{60} family of alkali-doped C_{60} solids (with A = K, Rb, or in part Cs) was followed in fairly short order by the emergence of a widespread conventional wisdom regarding the low-energy electronic properties of these compounds. (For a review, see for example Ref. [36].) Some central

elements of this conventional wisdom, which have both experimental and theoretical support, include the following:

- The conduction band is derived almost exclusively from the triply-degenerate t_{1u} orbitals that are the lowest unoccupied molecular orbitals of C_{60}. For K_3C_{60} this band is approximately 0.5 eV wide, and holds three electrons per C_{60} molecule (that is, the alkali metal atoms fully donate their valence electrons to the C_{60}-derived conduction band). The density of states at the Fermi energy $\mathcal{N}(E_F)$ is approximately 8 states per spin per molecule for K_3C_{60}.

- These compounds are, to first order, identical up to the precise value of the bandwidth W [or, equivalently, $\mathcal{N}(E_F)$], which is in turn determined by the distance between the C_{60} molecules. The latter can be tuned by external pressure or "chemical pressure" (that is, the choice of alkali intercalant species). In going from K to Rb doping, the values given above change by approximately 30% at zero pressure, with W decreasing and $\mathcal{N}(E_F)$ increasing.

- The interactions between quasiparticles apparently have some quantitative effects, such as enhancement of the Pauli susceptibility [37]. But despite their remarkable chemical formulas, and the fact that they are isotropic charge-transfer salts, they appear in many respects to be garden-variety metals.

- Long-wavelength transport measurements can be confounded by the fact that, unless great care is taken in materials preparation, samples are typically composed of A_3C_{60} grains embedded in (or surrounded by thin layers of) insulating material. For example, the initial transport measurements [38], which indicated that the resistivity increased with decreasing temperature, were not measurements of intrinsic properties; this became quite evident upon comparison with later measurements of higher-quality samples [39]. The sensitivity of transport measurements to sample preparation was well illustrated by the work of Watson *et al.* [40], in which K_3C_{60} films were almost continuously driven through a superconductor-insulator transition by varying the conditions under which they were deposited.

- The molecular orientations in the A_3C_{60} compounds exhibit, at room temperature and below, a restricted variety of static orientational disorder known as merohedral disorder [41] which

accounts for, among other things, the fact that x-ray probes indicate that the solid has four-fold rotational axes that the individual molecules lack. Although some correlations between the orientations of neighboring molecules exist [19, 20], this orientational disorder appears, in model calculations [6, 42, 43], to have a strong effect on the conduction band states: it washes out all sharp features in the density of states, and reduces the mean free path to of order the intermolecular spacing. This form of disorder is the bandwidth-dependent scattering mechanism mentioned in Chapter 1.

- In addition to the merohedral disorder, some other mechanism for conduction-electron scattering contributes to the residual resistivity ρ_0. Experimentally K_3C_{60} and Rb_3C_{60} have significantly different residual resistivities [38, 39], but merohedral disorder alone would give them nearly the same ρ_0 [7]. One possible origin is alkali vacancies: nominal Rb_3C_{60} is probably $Rb_{2.95}C_{60}$, for example [18].

We do not mean to slight those authors who disagree with any of the statements above, nor do we deny that various experimental observations are difficult to interpret within this framework. In fact, the purpose of this work is to point out, by means of comparison with model calculations, that electronic transport measurements (specifically the Hall coefficient R_H) in the A_3C_{60} compounds do not seem to be compatible with the conventional wisdom, and that one or more of the statements above may need to be reconsidered.

5.2 The Hall Effect in A_3C_{60}

As mentioned in Chapter 1, a measurement of the Hall effect in K_3C_{60} and Rb_3C_{60} by L. Lu *et al.* [3] produced an interesting result: the Hall coefficient is linearly dependent on the lattice constant a, and apparently has no other temperature dependence. In addition, their data show a sign change in R_H at roughly $a = 14.35$ Å. Their measurements are consistent with an earlier experiment by Palstra *et al.* [38] on K_3C_{60} thin films.

The explanation proposed by L. Lu *et al.*, hereafter referred to as "the Berkeley hypothesis", is based on Ong's scattering-length surface (which we discuss and use in Appendix B). Briefly, the scattering-length is defined by $\vec{l} = \mathbf{v_k}\tau_\mathbf{k}$, where $\mathbf{v_k}$ is the velocity and $\tau_\mathbf{k}$ is the relaxation time.

The scattering length surface A_l is the surface traced out by $\vec{l}$ as $\mathbf{k}$ moves around the Fermi surface. Ong connects the Hall coefficient to the number of flux quanta that penetrate this surface [44].

An important aspect of the scattering-length surface is that, in regions where the Fermi surface has negative curvature, the l curve develops secondary loops that may have the opposite circulation of the main loop. If the circulation is in the opposite sense, the flux threading these secondary loops acts to reduce the Hall coefficient; in some sense, the area in these loops has the same sign as the circulation. The Berkeley hypothesis considers the Fermi surface in A_3C_{60}, which consists of numerous small electron-like and hole-like pockets. These pockets will contribute in opposite ways to the area of the scattering surface.

Now, consider the effect of disorder on the Fermi surface. Macroscopically, disorder blurs the Fermi surface over some width; for a specific realization of the disorder in a finite cluster, the Fermi surface will develop fine detail over that width. This width increases with the disorder. The Berkeley group argues that since regions of negative curvature will, in general, be closer in $\hat{k}$ space to the bottom of the band, and will therefore have larger Fermi velocities, their contribution to A_l will be larger than the contribution from regions of positive curvature.

Since it is known that there are both bandwidth-dependent and bandwidth-independent sources of scattering (merohedral and, in our model, Anderson, respectively), they argue that a bandwidth decrease should increase the effective amount of disorder, which increases the width of the Fermi surface "smearing", and therefore decreases A_l, which in turn decreases R_H. Such a bandwidth decrease would be expected if the lattice constant is increased.

Thus, the Berkeley group argues, an increase in lattice constant increases the amount of Fermi surface blurring, which leads to a greater contribution from the "anti-circulating" loops. The primary loop circulates in such a way to make R_H negative, indicating that these anti-circulating secondary loops should increase R_H, and therefore increasing the lattice constant should increase R_H.

In our calculations, we can directly change the ratio between bandwidth-dependent (merohedral) disorder, and bandwidth-independent (Anderson) disorder. If the Berkeley group's hypothesis is correct, increasing the Anderson disorder should increase the Hall coefficient.

Another possible explanation for the behavior of R_H, the "band-filling hypothesis", was suggested to us by a calculation by Erwin and Pickett [45] on an orientationally ordered A_3C_{60} structure. Their

results show a strong dependence of R_H on the Fermi energy; in particular, there is a sign change near half-filling. While this calculation did not include disorder effects, it does suggest a mechanism by which R_H could change sign: changing the lattice constant could change the effective band filling.

As a part of these calculations, we obtained longitudinal conductivities for these model systems. We therefore took the opportunity to look for deviations from Matthiessen's rule (DMR), an issue that has not previously been examined for A_3C_{60} systems in the theoretical literature, but has important implications for the analysis of experimental conductivity data.

We describe our model systems in Section 5.3. Our results are presented and discussed in Section 5.4, and we present our conclusions in Section 5.5.

Previous A_3C_{60} theoretical work reports only σ_{xx} for merohedral systems at half filling, and R_H for clean systems. As there are some interesting features in both quantities for Anderson and mixed systems, we will examine σ_{xx}, σ'_{xy}, and R_H (as we did for the Anderson impurity models in Chapter 3) for all systems studied.

5.3 A_3C_{60} Models

As was noted in the introduction, it is known that A_3C_{60} has some bandwidth-independent scattering mechanism. We introduce such a mechanism into our calculations in the form of Anderson disorder, a particularly simple type of disorder that can be thought of as crudely accounting for alkali vacancies.

Our model systems then fall into two general categories:

- "Anderson systems": orientationally ordered systems (no merohedral disorder), with the strength of the Anderson disorder denoted D. The special case of $D = 0$ will be referred to as a "clean system".
- "Mixed systems": merohedrally disordered systems, with Anderson disorder again defined by D. The special case of $D = 0$ will be referred to as a "merohedral system".

(We should note that the Anderson systems are not physically realizable: real A_3C_{60} systems are not orientationally ordered. However, these are useful calculations for other reasons; for example, calculations of σ_{xx} for these systems, together with those for mixed systems, permit tests of Matthiessen's rule.)

In constructing the Hamiltonians for these models (as described in Chapter 2), we are making the following assumptions:

- The low-energy electronic excitations are well described by a tight-binding Hamiltonian which only involves molecular valence orbital states [16].
- The merohedral disorder is completely uncorrelated from site to site.
- Anderson disorder, uncorrelated between sites and affecting all C_{60} orbitals equally, adequately accounts for whatever non-merohedral disorder exists in real systems (alkali vacancies and such). In reality, the disorder *would* be correlated to some degree, and would split the t_{1u} degeneracy; but we proceed in this fashion on the grounds that it is the simplest disorder that introduces the physically required bandwidth-independent scattering mechanism.
- We neglect electron-phonon interactions, and perform all calculations at $T = 0$.

Having made these assumptions, we proceed via a "brute force" calculation that does not require any further approximations beyond finite-size extrapolations.

We again use (2.2) as our Hamiltonian, with three orbitals per site. We do not model the alkali sites. In zero magnetic field, the $t_{(i\mu)(j\nu)}$ are the same hopping amplitudes used previously by Gelfand and Lu [6]. (As has been pointed out [7], these matrix elements are too small by roughly a factor of ten, but that has no effect on our results. However, even after rescaling, those matrix elements are not the best one might choose; see Erwin and Mele [42] for a thorough discussion. We did perform a few calculations using their matrix elements, and found that both sets of matrix elements produce essentially the same results. We used Gelfand and Lu's values simply because it was convenient to do so.) Merohedral disorder is introduced via these $t_{(i\mu)(j\nu)}$ by randomly assigning each C_{60} molecule one of the two allowed orientations with equal probability, and inserting the appropriate amplitudes into the Hamiltonian matrix. The second term in (2.2) represents the Anderson disorder, implemented in the same fashion as for the two-dimensional systems is discussed in Section 3.2.

As noted in Section 2.3, the Peierls substitution does not take into account the effect of the magnetic field on the molecular orbitals. The Hamiltonian corresponding to a given buckyball is a 3×3 matrix; each buckyball in a finite-cluster has a corresponding 3×3 matrix on the diagonal of

the finite-cluster Hamiltonian, which can be thought of as the "on-ball" parts of the Hamiltonian. The Peierls substitution affects only the "off-ball" parts; we need to find the first-order correction to the on-ball Hamiltonian.

The triply-degenerate t_{1u} orbitals on each buckyball can be expressed as states that are symmetric with respect to rotation about the x, y, and z axes; let us denote them $|x\rangle$, $|y\rangle$, and $|z\rangle$. We would expect a magnetic field in the z direction to leave $|z\rangle$ alone, but to mix $|x\rangle$ and $|y\rangle$ (i.e., to introduce non-zero off-diagonal elements in the on-ball Hamiltonian). To find this value, we first constructed a Hamiltonian representing a single buckyball, in much the same way we construct Hamiltonians for the KG calculation. The $t_{(i\mu)(j\nu)}$ were taken as 0.25 eV for the bonds between two hexagonal faces, and 1.2 times that for the shorter bonds between hexagonal and pentagonal faces [6]. This Hamiltonian (a 60×60 matrix) was diagonalized; the t_{1u} orbitals were the eigenstates corresponding to the thirty-first, thirty-second, and thirty-third eigenvalues. We arbitrarily chose one of these, rotated it by 180° about the z axis, and found the symmetric part; the result was taken to be $|z\rangle$. The $|x\rangle$ and $|y\rangle$ states were obtained by performing the appropriate geometric transforms on $|z\rangle$. The first-order correction to the on-ball Hamiltonian element $\langle i \,|\, j\rangle$ can be found by taking $\langle i \,|H'|\, j\rangle$. As expected, these values are all zero except $\langle x \,|H'|\, y\rangle \cong 1.74 \times 10^{-3}$ eV. This is roughly an order of magnitude smaller than the inter-molecular matrix elements (typically of order 10^{-2}).

For our A_3C_{60} calculations, we used several lattice sizes, denoted by the number of standard fcc cells in the x, y, and z directions (the number of C_{60} molecules is 4 times the number of cells). Unless stated otherwise, the results below were obtained on $6 \times 6 \times 4$ lattices with open boundaries in x and y, periodic boundaries in z, and typically averaged over 10 to 50 realizations of the disorder. We should note that for periodic systems, the finite-size effects are known to be quite small when merohedral disorder is present: $4 \times 4 \times 4$ and $6 \times 6 \times 6$ systems yield almost indistinguishable results for σ_{xx} [7].

However, we should point out that system size is not a parameter in the following discussions; most of our calculations were using the largest system size we could comfortably handle, and we make no explicit extrapolations in size as we did in Chapter 3. This is consistent with the results of Section 3.6, where R_H was calculated simply on the results from the largest system size available (since no size extrapolation was possible for σ'_{xy}). This was also necessary, as we added the band

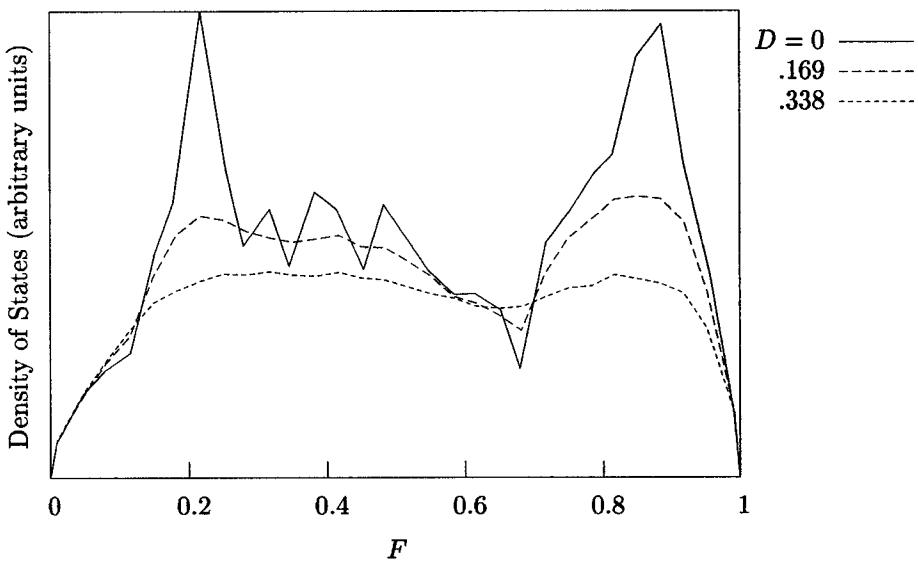

Figure 5.1: DOS as a function of band filling for Anderson systems. The bandwidths have been normalized.

filling F as a parameter for our A_3C_{60} work; the amount of data needed to adequately cover both parameters F and L would have been prohibitive.

5.4 Results

We begin with comment on units: it is simplest to define our unit of energy $\hat{\epsilon}$ to be equal to the bandwidth of the merohedral system. This is not the scale the $t_{(i\mu)(j\nu)}$ are in, which leads to the apparent use of odd values for some parameters, D and η in particular. Those examining our raw data should keep in mind that in the "native" units of our calculation, the merohedral system bandwidth is 0.05907.

Also note that in K_3C_{60}, with an fcc lattice constant of 14.4 Å, $\hat{a} = 7.2$ Å, and $e^2/\hat{a}h = 536$ $(\Omega\,\mathrm{cm})^{-1}$.

As discussed above, we are interested in calculating R_H for systems involving a variety of disorder types and band fillings. The low-field Hall coefficient can be written $R_H = \sigma'_{xy}/\sigma^2_{xx}$, so we examine the behavior of σ'_{xy} and σ_{xx} as a function of both the ratio of Anderson to merohedral disorder and the band filling.

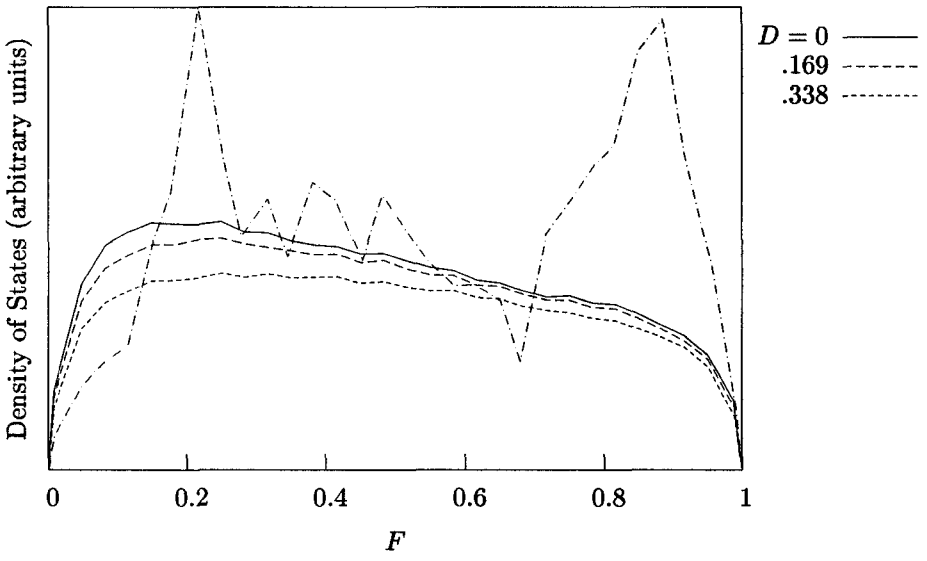

Figure 5.2: DOS as a function of band filling for mixed systems; the clean system bandwidth (from Fig. 5.1) has been superimposed. The bandwidths have been normalized.

We will frequently be referring to the density of states (DOS) for different systems. Figs. 5.1 and 5.2 show the DOS as a function of band filling for Anderson and mixed systems. We can, perhaps, anticipate some results by noting that while Anderson disorder has a large effect on the orientationally ordered system's DOS, in the presence of merohedral disorder it does little more than broaden the band. It may be instructive to compare the band widths for different systems; the D dependence of Anderson and mixed systems' bandwidths is shown in Fig. 5.3.

5.4.1 Merohedral systems

As for σ_{xx} in the two-dimensional systems, we see that that the Drude peak is shifted from $\omega = 0$ to some size-dependent finite frequency (Fig. 5.4), but not by all that much (compare to Fig. 3.6), which to some degree validates the assumption that $6 \times 6 \times 4$ is "large enough" to produce reasonable results without further extrapolation in L.

We now proceed as we did in Chapter 3 to extrapolate to the thermodynamic limit. First, we again take the value $\sigma_{xx}(\omega = \omega_{\text{peak}})$; as noted above, we do not take a $L \to \infty$ limit, and simply (using the same notation we used earlier) write the result as $\sigma_{xx}(D, F, \eta)$. We then take the limit

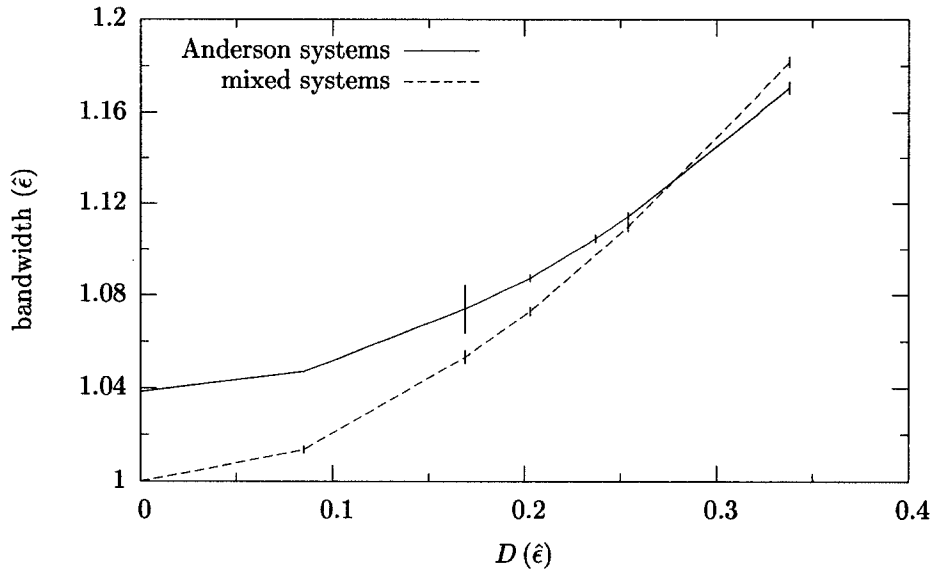

Figure 5.3: Bandwidth as a function of Anderson disorder parameter D. The error bars are statistical.

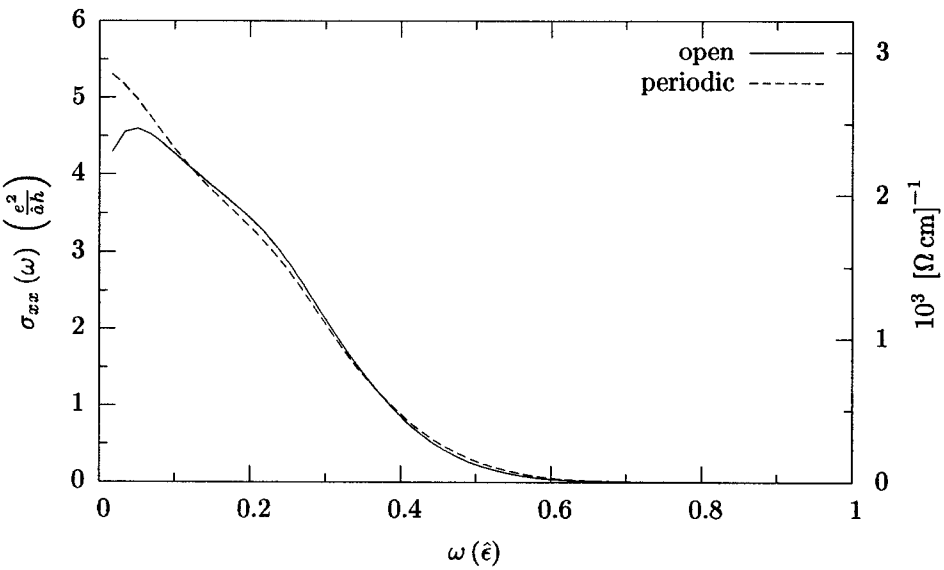

Figure 5.4: $\sigma_{xx}(\omega)$ for merohedral systems with open and periodic boundary conditions. Here, we used $\eta = 0.01$. Statistical errors are roughly the width of the line. Using $\hat{a}$ for $K_3C_60 = 14.4$ Å, the conversion factor is $e^2/\hat{a}h = 536\ (\Omega\,\mathrm{cm})^{-1}$.

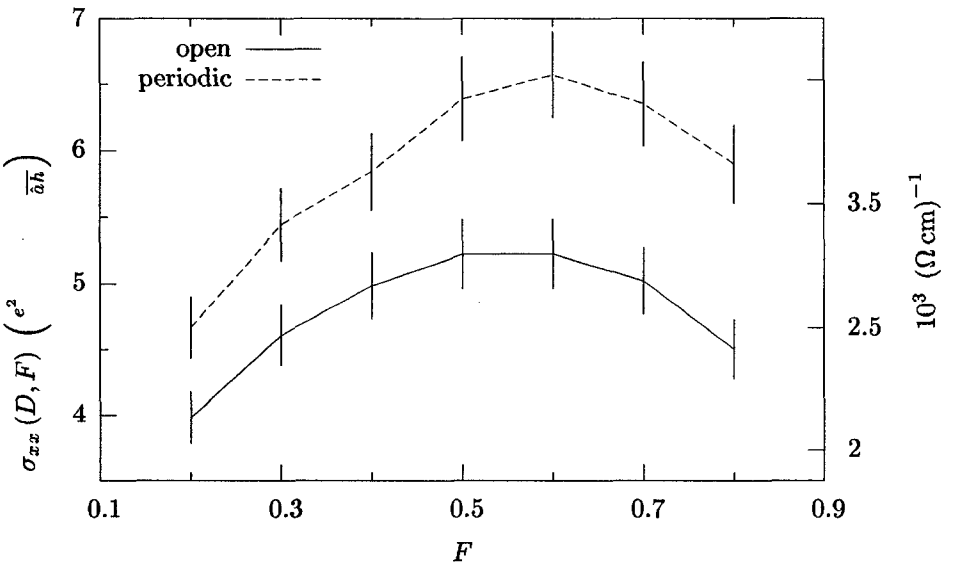

Figure 5.5: $\sigma_{xx}\,(D=0,F)$ as a function of band filling, for merohedral systems with periodic boundaries at $\omega = 0$, and with open boundaries at $\omega = \omega_{\mathrm{peak}}$. The error bars are due to the η extrapolation.

as $\eta \to 0$ using much the same fitting procedure used earlier, fitting to $1/(a\eta + b)$. As before, we require at least 5% error on the fitting results.

In Fig. 5.5, we present the results of this extrapolation for systems with various band fillings, along with the periodic system results for comparison. We note that while our analysis of fixed boundary systems has introduced a systematic error of about 20% compared to the periodic system results, the variation with band filling is nearly identical.

A somewhat counterintuitive finding is that the conductivity is increasing over an interval in band filling where the density of states is decreasing slightly. (Actually, this is not completely surprising, as we do not expect the conductivity to simply be proportional to the DOS in these complicated systems.)

We now turn our attention to σ'_{xy} (σ^0_{xy} again averaging to zero). The first-order correction, σ'_{xy}, as a function of frequency, is shown in Fig. 5.6 for several different fillings. Again, proceeding as we did for the two-dimensional models (see Section 3.6), we take $\omega = \omega_{\mathrm{peak}}$, and then take the $\eta \to 0$ limit by fitting to $(a\eta + b)^{-2}$. Here we had to be particularly careful to find the appropriate range of η values to use. Figure 5.7 shows what happens for η outside of this range. Fig. 5.8 shows the

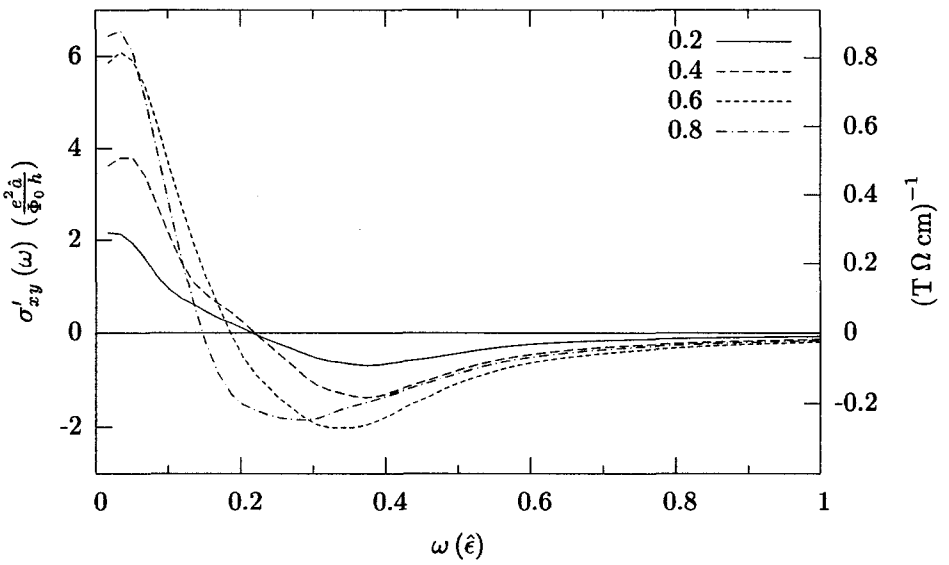

Figure 5.6: $\sigma'_{xy}(\omega)$ for merohedral systems as a function of band filling. Here, $\eta = 3.21 \times 10^{-2}\hat{\epsilon}$. Statistical error bars are omitted for clarity. The conversion factor is $e^2\hat{a}/\Phi_0 h = 0.134\ (\mathrm{T}\,\Omega\,\mathrm{cm})^{-1}$.

result, $\sigma'_{xy}\,(F)$.

With these results in hand, we examine the behavior of the Hall coefficient as a function of band filling (Fig. 5.9). Note, most importantly, that we see no sign change. This stands in contrast to Fig. 2 from Erwin and Pickett [45], which shows a sign change very near half filling in addition to considerable structure in R_H vs. Fermi energy. These differences are not surprising, considering how the DOS differs between Anderson and merohedral systems (Fig. 5.1); in the former, one has two weakly overlapping sub-bands, whereas in the latter the DOS is a nearly constant function of Fermi energy over most of the band.

5.4.2 Anderson systems

We carried out much the same analysis on Anderson systems.

Figure 5.10 shows $\sigma_{xx}\,(\omega)$ for various disorder levels at half filling. The first question we asked was what value for D would be appropriate for comparison with the merohedral systems. We were interested in finding a value for D that approximately reproduced σ_{xx} of the merohedral system, and seeing how σ'_{xy} compared. We can see that roughly $D = 0.169$ produces value of σ_{xx} that matches

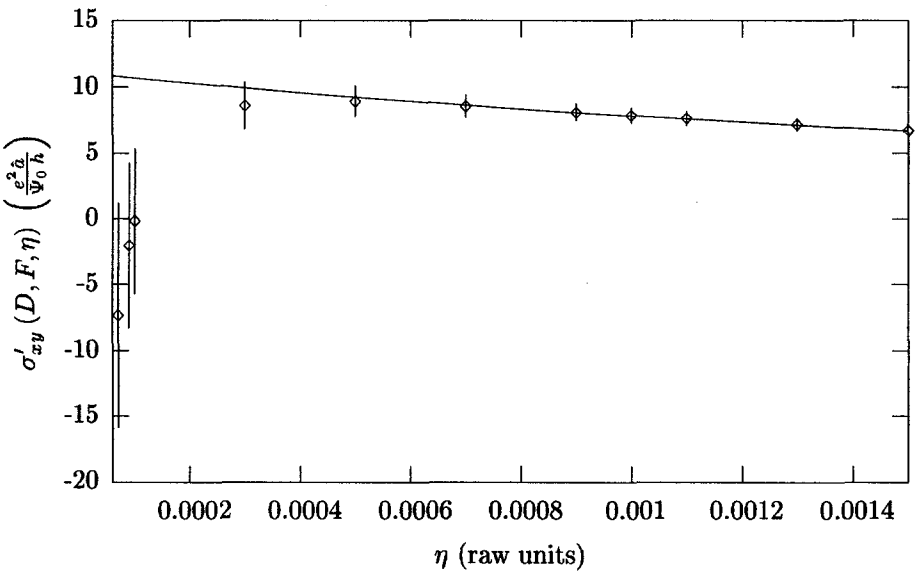

Figure 5.7: An example of the fit of $\sigma'_{xy}(D,F,\eta)$ to $(a\eta+b)^{-2}$, showing the need to restrict the fit to a range of "good" etas. The η axis is in terms of our "native" units. Here, the "good" eta range could be said to start at $\eta = 5 \times 10^{-4}$, but this was not consistently true.

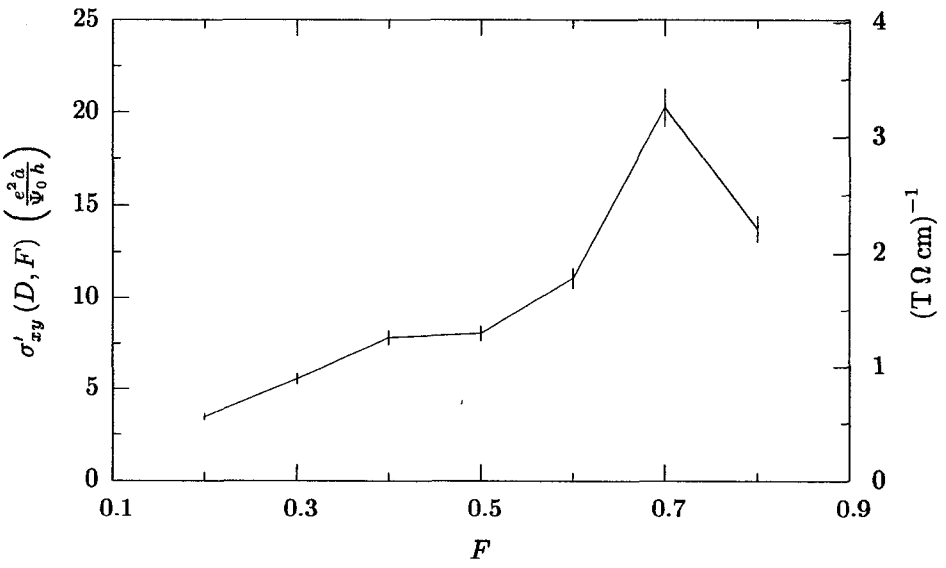

Figure 5.8: $\sigma'_{xy}(D,F)$ as a function of the band filling F for merohedral systems. The error bars represent procedural errors.

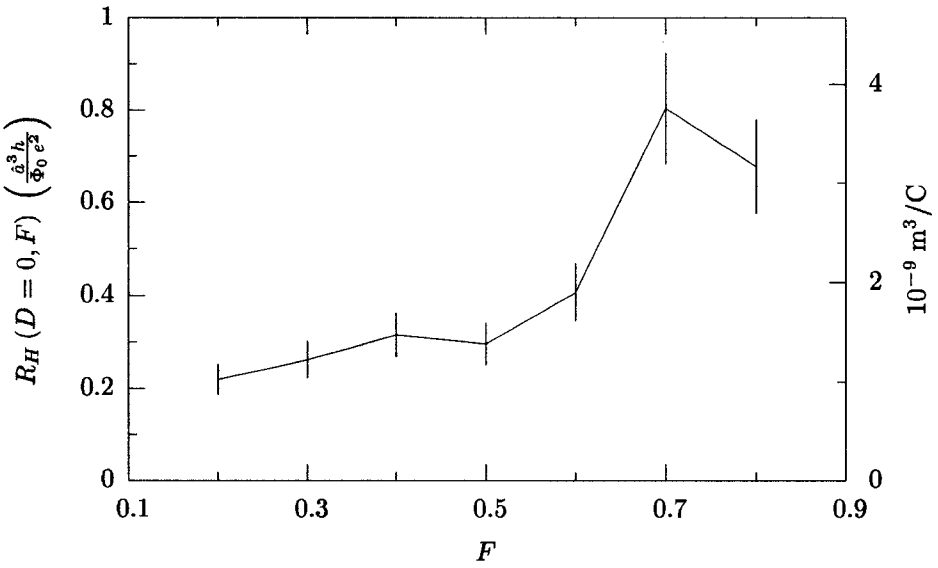

Figure 5.9: Hall coefficient as a function of band filling for merohedral systems. The conversion factor is $\hat{a}^3 h/\Phi_0\, e^2 = 4.671 \times 10^{-9}$ m^3/C

the value obtained for the merohedral system.

Figure 5.11 presents σ_{xx} versus band filling for Anderson systems. The behavior near 2/3 filling is reasonable considering that the DOS has a sharp dip there, in both clean and Anderson systems.

Turning to the Hall effect, Anderson systems yield the results displayed in Fig. 5.12. Here we *do* see a sign changes as a function of band filling, similar in many ways to Erwin and Pickett's results [45].

Figure 5.13 shows R_H at half filling as a function of Anderson disorder. It is evident that increasing D leads to, if anything, a slight decrease in R_H.

5.4.3 Mixed systems

Finally, we examine the results for mixed systems. As a function of filling, σ_{xx} (Fig. 5.14) is similar to the merohedral case; this is, perhaps, not surprising given that adding modest Anderson disorder has little effect on the DOS of merohedrally disordered systems.

An obvious question follows: does Matthiessen's rule hold? Figure 5.15 shows that it does not. In fact, note that the resistivity in mixed systems is, for the larger fillings, actually *less* than the

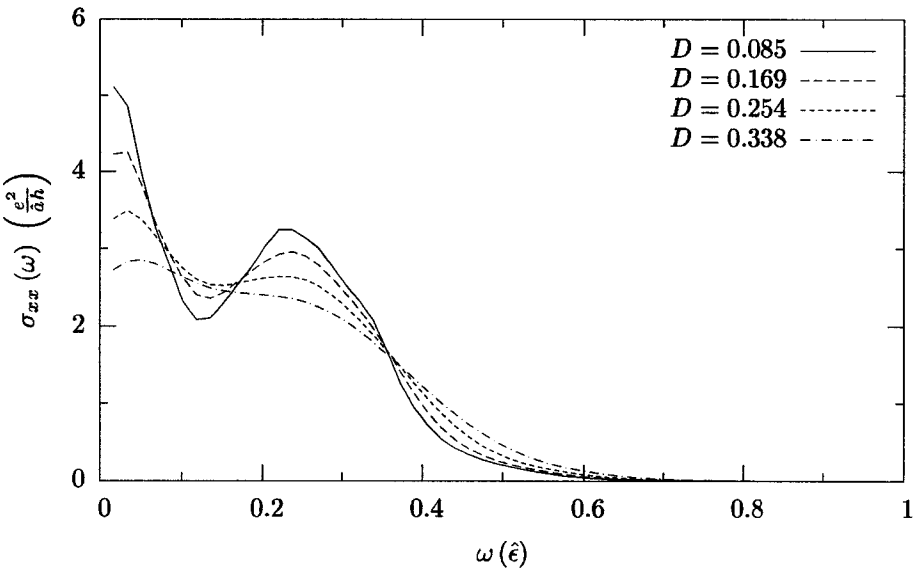

Figure 5.10: $\sigma_{xx}(\omega)$ for Anderson systems, with $F = 0.5$ and $\eta = .01$.

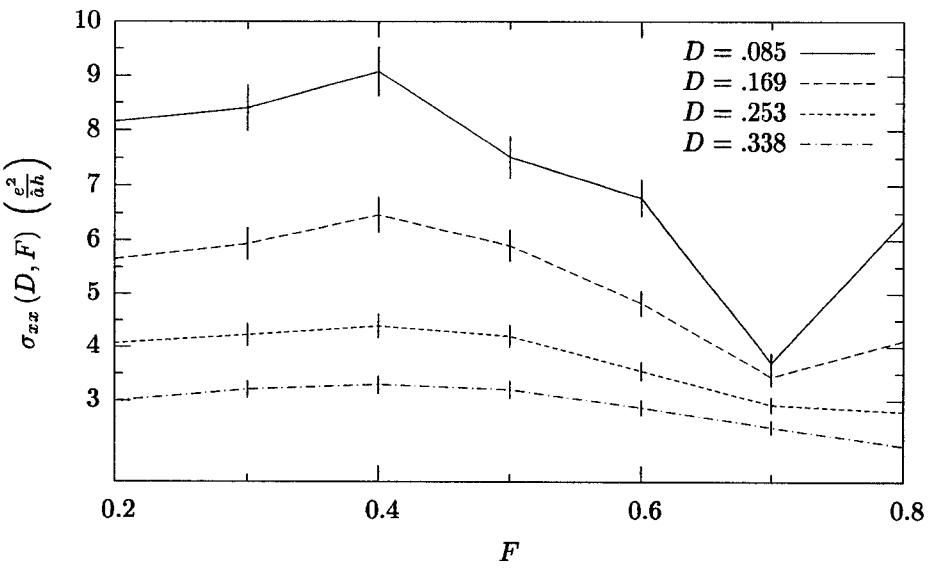

Figure 5.11: $\sigma_{xx}(D,F)$ as a function of band filling for Anderson systems. The error bars represent 5% error, due to the $\eta \to 0$ extrapolation.

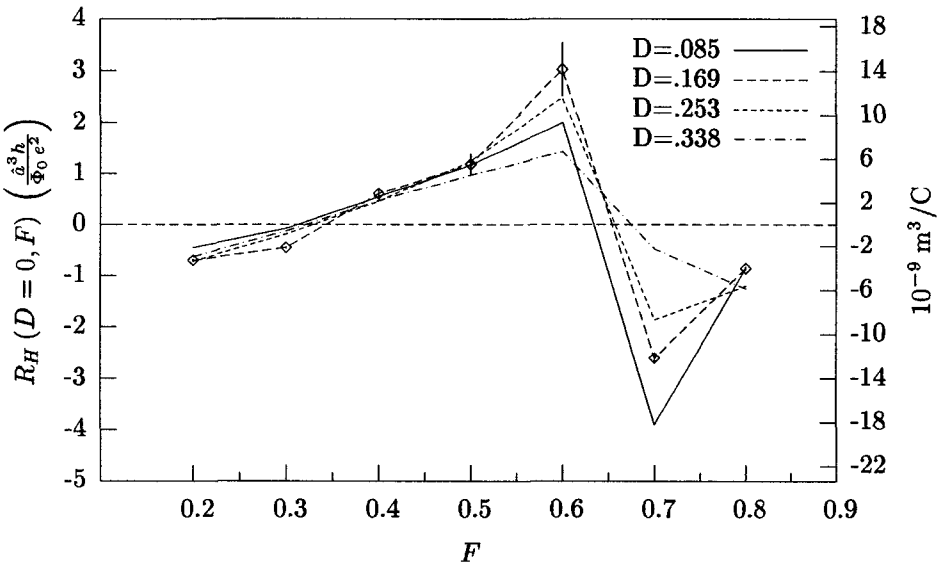

Figure 5.12: R_H as a function of band filling, for Anderson systems with several values of D. Only the error bars for $D = 0.169$ are shown for clarity, and represent 7% error due to the η extrapolation.

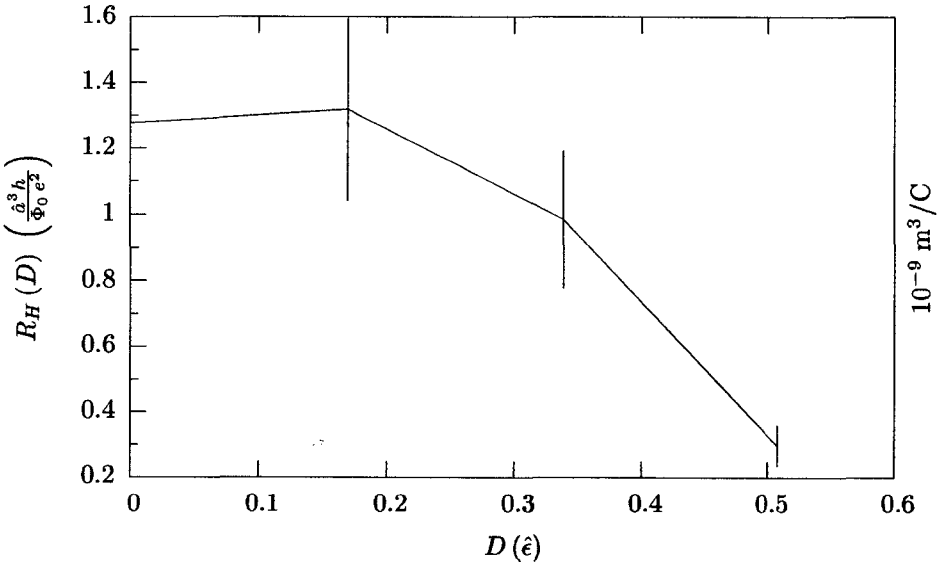

Figure 5.13: Hall coefficient R_H as a function of D in Anderson systems at half filling.

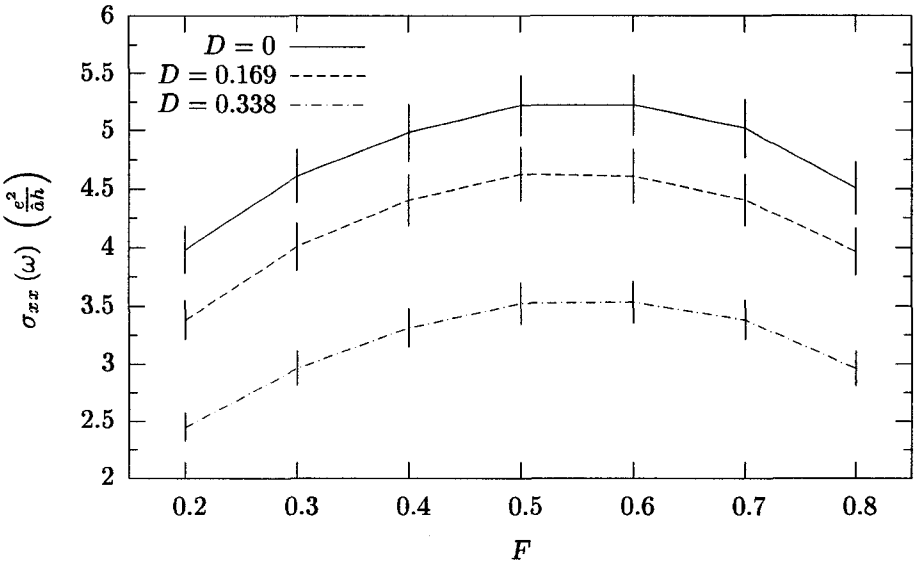

Figure 5.14: $\sigma_{xx}(D, F)$ as a function of band filling for mixed systems. As usual the error bars represent 5% error from the η extrapolation.

resistivity for the corresponding Anderson systems. It seems that the violation of Matthiessen's rule is quite strong. One could anticipate such violations to be quite generic in A_3C_{60} systems because electron scattering due to orientational disorder and due to other mechanisms should have different differential scattering cross-sections [4].

Finally, we turn to the calculations most directly related to the original motivation for our work. Figure. 5.16 shows the dependence of R_H on filling for mixed systems. It is very similar to the merohedral case (Fig. 5.9), and shows little of the structure seen in Anderson systems (Fig. 5.12).

Figure 5.17 shows the Hall coefficient at half filling as a function of Anderson disorder parameter D. We see little variation in R_H, and no sign change, even up to D values of approximately $(2/3)\hat{\epsilon}$. This behavior is similar to that seen in Anderson systems (Fig. 5.13), where we saw a slightly decreasing R_H as a function of D. It seems that at half filling, behavior in contradiction to the Berkeley hypothesis is generic.

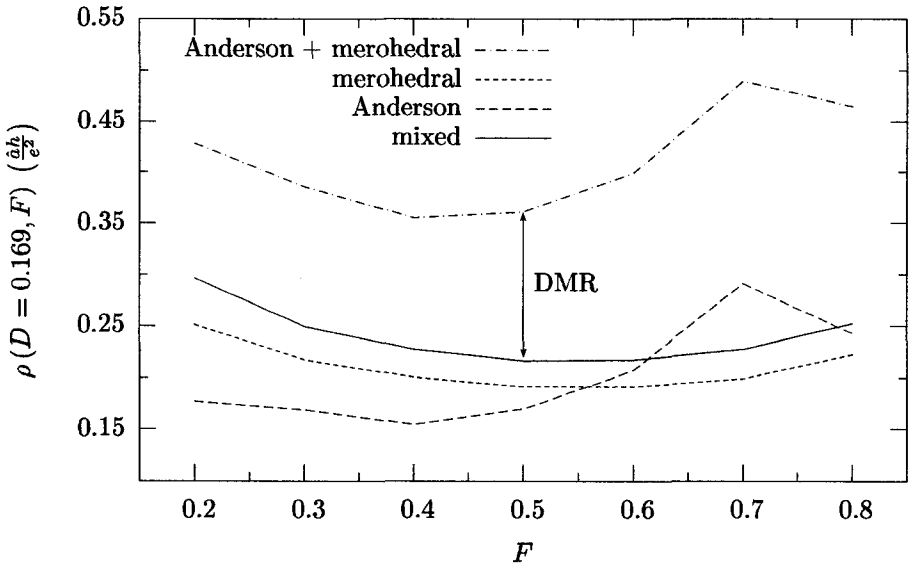

Figure 5.15: ρ as a function of band filling for Anderson, merohedral, and mixed systems. The disorder parameter for all systems with Anderson disorder is $D = 0.169$. Error bars are omitted for clarity. Also plotted (topmost curve) is the sum of the merohedral and Anderson resistivities. The difference between this curve and the mixed system result is the deviation from Matthiessen's rule (labeled DMR) .

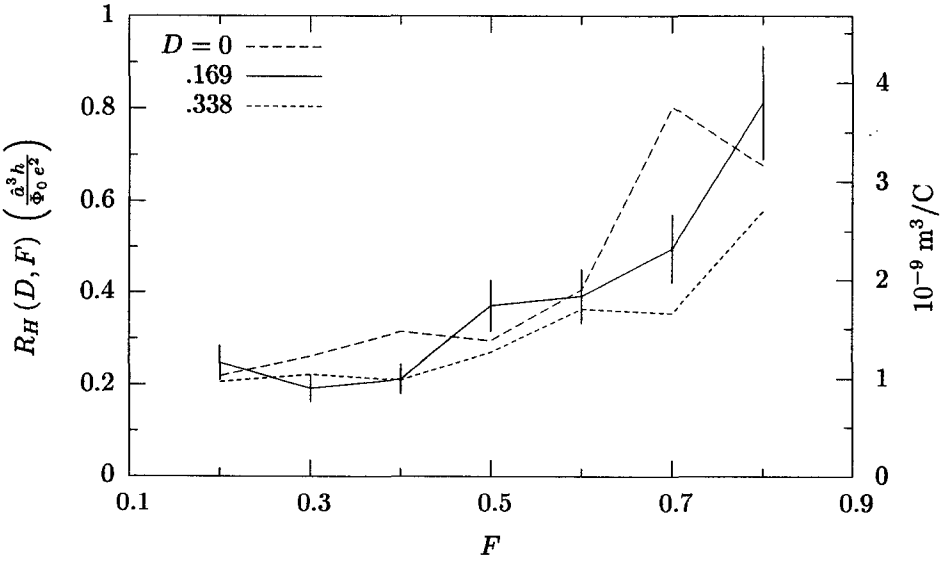

Figure 5.16: R_H for mixed systems. Error bars are only shown for $D = 0.169$ for clarity, and are due to procedural error; the statistical errors were roughly 1/2 to 1/4 as large.

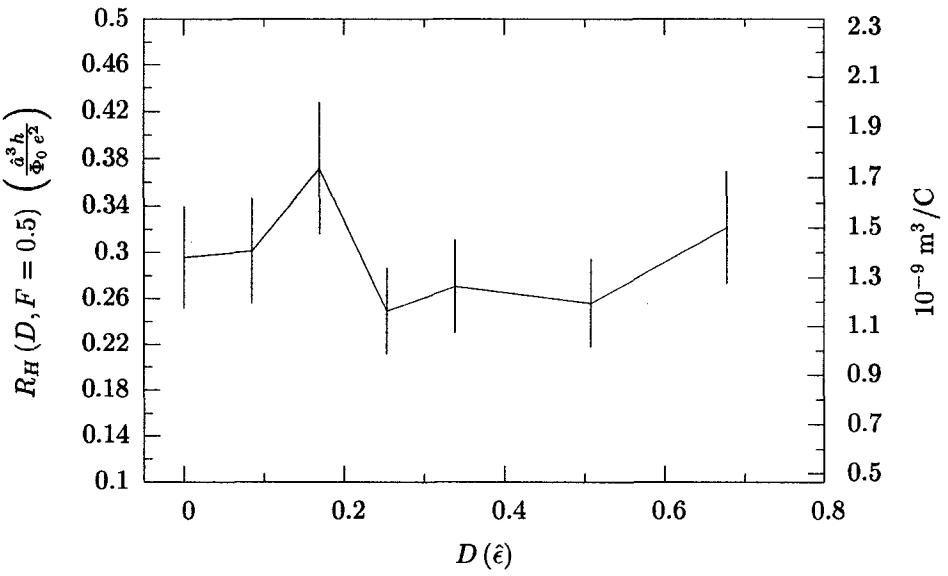

Figure 5.17: R_H for mixed systems, as a function of Anderson disorder parameter D, at half filling.

5.5 Conclusions

5.5.1 Longitudinal conductivity

It is known that the significant deviations from Matthiessen's rule seen in alkali metals has lead to considerable difficulty in the interpretation of low temperature conductivity data [5] in those metals. The enormous violations of Matthiessen's rule evidenced in Fig. 5.15 suggest that similar caution should be used in the interpretation of low temperature conductivity data in A_3C_{60} systems. (In fact, the DMR is so large, it might affect not-so-low temperature work!) In particular, some of the quantitative results of such work as Refs. [39] and [46] may need to be reconsidered. While extracting information about electron-phonon coupling from high-temperature resistivity data (as in Ref. [47]) is probably safe, extracting quantitative information from the low temperature T^2 behavior may be more perilous than previously thought.

5.5.2 Hall effect

Our results for both mixed and Anderson systems do not support the hypothesis presented by L. Lu *et al.* to account for the observed variation of the Hall conductance with lattice spacing in A_3C_{60}

systems. Recall that their hypothesis predicts that the Hall coefficient should be an increasing function of the disorder strength D, with negative values at small D. This hypothesis, if correct, should apply equally well to our calculations and the experimental results, but as shown in Figs. 5.13 and 5.17, we see neither of these predicted features at half band filling: R_H is positive at low D and either shows no clear trend or decreases slightly with D.

We therefore are lead to reexamine the analysis behind their hypothesis. To evaluate σ_{xy}, L. Lu *et al.* applied Ong's scattering length surface construction [44] to the Fermi surface obtained from a disordered supercell. As a result, they find that an increase in the disorder leads to an increase in σ_{xy}; this behavior depends on some specific features of the A_3C_{60} Fermi surface but is otherwise quite generic in that it does not appear to depend on the details of the disorder.

We suspect that their approach may be flawed, in that when applying the scattering length surface construct to a disordered system, Ong's prescription is to use the *clean* system Fermi surface, with the disorder entering only through $\tau(\mathbf{k})$ for $\mathbf{k}$ on the Fermi surface. What they have done instead is calculate the Fermi surface for particular supercell realizations, and then build the corresponding scattering length surface. This must have involved making some assumptions about $\tau(\mathbf{k})$, which may not have been justified.

However, we still must account the discrepancy between our calculations and the behavior observed *experimentally* by L. Lu *et al.* There are various possibilities:

- First, we may not be using the correct static disorder model. Perhaps simple Anderson disorder lacks some crucial property of the (non-merohedral) disorder that is present in A_3C_{60} samples. However, this seems highly unlikely, given the small effect Anderson disorder has on the DOS in merohedrally-disordered systems.

- Second, perhaps the experimentally observed behavior is due in part to finite temperature effects. The Berkeley hypothesis and the current work both neglect thermal effects aside from the temperature dependence of a. However, it seems unlikely such effects could account for the low temperature behavior, such as R_H in K_3C_{60} and Rb_3C_{60} differing by a factor of 6 at roughly 50 K, and having different signs above roughly 150 K.

- Third, electron correlations may be contributing in some fashion to the Hall effect. Given

their narrow conduction bandwidths, the A_3C_{60} materials cannot be very far from a Mott transition with increasing a. Properly accounting for both disorder *and* electron correlations in transport coefficients is beyond our capabilities, so we cannot do more than speculate on their significance.

- Finally, perhaps the observed lattice spacing dependence of R_H reflects a failure of the "conventional wisdom" for the A_3C_{60} compounds. Our calculations of R_H for Anderson systems (see Fig. 5.12) exhibit a sign change at approximately 1/3 filling, and roughly linear behavior in the range from 0.3 to 0.6 band filling. If the band filling were to be an increasing function of a, this might explain the experimental R_H results. This suggestion supposes that A_3C_{60} is, in some sense, "less merohedral" than we suppose; this might be accounted for by correlations in the C_{60} orientations. As noted earlier, it is known that the molecular orientations are correlated to some degree, but we have no such correlation in our models. However, this suggestion is obviously in contradiction with density-functional electronic structure calculations [15, 17].

The only reasons we do not dismiss this last possibility out of hand are that, firstly, the dependence of the DOS on band filling in merohedrally disordered systems is sufficiently weak that low-energy experimental probes (such as nuclear and electronic spin relaxation and electronic specific heat) cannot rule it out, and secondly, it is the only mechanism we have found within the class of models we have explored which can generate anything like the experimental results for R_H. We also note that the range of R_H experimentally found by the Berkeley group (particularly their Rb_3C_{60} results) are roughly $[-3\,\text{to}\,1] \times 10^{-9}$ m^3/C, which is roughly consistent with our Anderson results near 1/3 filling.

Our only justification for pursuing this suggestion further is a paper by Schulte and Böhm [48], whose quantum-chemical calculation indicates that the charge transfer from the alkali intercalants to the C_{60} molecules is incomplete. However, the implications of their calculation for the conduction-band effective Hamiltonian are not easy to work out. Their results imply that the alkali valence orbitals need to be explicitly included in tight-binding models for the A_3C_{60} conduction bands. This we have not attempted. However, if we continue to neglect the alkali orbitals but take the charge transfer values from Schulte and Böhm literally, for K_3C_{60} we arrive at a band filling of roughly one-quarter, which is approximately where we see a sign change in R_H (Fig. 5.12). Furthermore,

the K atoms in octahedral sites have nearly twice as much charge transfer as those in tetrahedral sites, suggesting that the charge transfer should increase with a. (This is a presumption on our part — Schulte and Böhm do not present results for different lattice constants.)

So, this (inconsistent!) application of Schulte and Böhm's calculation yields a prediction for R_H vs. a which has at least the correct sign of the variation and order of magnitude. Because of the inconsistent treatment of the alkali orbitals, we cannot take this agreement with experiment too seriously. However, we do take seriously the notion that the "conventional wisdom" of complete charge transfer from alkali valence orbitals to C_{60} t_{1u} orbitals should critically reconsidered.

5.6 Directions for Future Research

Perhaps the most obvious question to ask is whether or not the experimental data is really a low temperature effect. Is the apparent "collapse" of data from K_3C_{60} and Rb_3C_{60} onto a single curve an accident, or is it really indicative of a low-temperature effect? Measuring R_H in K_3C_{60} while varying the pressure, or using different alkali species, while keeping the temperature fixed, should settle this issue. So this would be our first suggestion for further research:

- Repeat the Berkeley group's experiment, holding temperature constant and varying the pressure.

If we continue to presume that the data collapse is really there (and not just a coincidence), we suggest that our work be continued with more sophisticated models, which would address some of the possible "missing physics" discussed above. In particular:

- Our modeling of merohedral disorder has no correlations at all. Since the only hint of a sign change in R_H was in orientationally-ordered systems, one could add varying amounts of orientational correlation, and see what happens.

- If the charge transfer from the alkali atoms is indeed incomplete — again, a fairly radical hypothesis, but the only mechanism by which our model can reproduce the experimental results — then the alkali sites need to be taken into account. Adding the alkali sites into our finite-cluster models would allow investigation of this possibility.

Appendix A

Derivation of the Kubo-Greenwood formula

"Deep in the fundamental heart of mind and Universe," said Slartibartfast, "There is a reason."

Ford glanced sharply around. He clearly thought this was taking an optimistic view of things.

- Douglas Adams [23]

For this derivation, we will use capital Greek letters for many-particle states, and lower case Roman for single-particle states. Lower-case Greek will represent vector components (i.e., $\alpha = x, y,$ or z). The energies of many-particle states will be denoted by E while energies of single-particle states will be denoted ϵ.

As derived by Mahan [49], the Kubo formula is[1]

$$\sigma_{\alpha\beta}(\mathbf{q},\omega) = \frac{1}{\hbar\omega V}\int_0^\infty dt\, e^{i\omega t}\left\langle [j_\alpha^\dagger(\mathbf{q},t)\,,\, j_\beta(\mathbf{q},0)]\right\rangle + \frac{n_0 e^2}{m\omega} i\delta_{\alpha\beta} \tag{A.1}$$

[1] Unlike Mahan, we will be explicit about factors of $\hbar$ throughout, to simplify the later discussion of units.

which we would like to write in terms of exact single-particle states of a non-conducting system. We neglect the second term on the right, as we are only interested in the *real* part of the conductivity.

The angle-brackets in the integrand denote a thermodynamic average, so this term can be written explicitly (Pathria [50], p 119, eq 5.2.16)

$$\frac{\mathrm{Tr}\left(e^{-\beta(H-\mu N)}\left[j_\alpha^\dagger(\mathbf{q},t)\,,\,j_\beta(\mathbf{q},0)\right]\right)}{\mathcal{Q}(\mu,V,T)}$$

where $\mathcal{Q}(\mu,V,T)$ is the Grand Partition function, and Tr denotes the trace and is the summation over some complete set of many-body states $\mathrm{Tr} \equiv \sum_\Psi \langle\Psi|\cdots|\Psi\rangle$ (Mahan, p 134). Writing $\xi = H - \mu N$, the numerator is then

$$\sum_\Psi \left\langle \Psi \left| e^{-\beta\xi}\left[j_\alpha^\dagger(\mathbf{q},t)\,,\,j_\beta(\mathbf{q},0)\right]\right|\Psi\right\rangle \ .$$

Operating the exponential to the left gives

$$\sum_\Psi e^{-\beta\xi_\Psi}\left\langle \Psi \left|\left[j_\alpha^\dagger(\mathbf{q},t)\,,\,j_\beta(\mathbf{q},0)\right]\right|\Psi\right\rangle \ .$$

We now simplify the current operators. As written, (A.1) describes a system under the influence of an electric field $\mathbf{E} = Ee^{i\mathbf{q}\cdot\mathbf{r}-i\omega t}$. We are interested in the ac conductivity, so we want a driving electric field that varies in time but not in space; therefore we let $\mathbf{q} \to 0$. We then use the general result that $\mathcal{O}(t) = e^{iHt/\hbar}\mathcal{O}(t=0)e^{-iHt/\hbar}$, and defining $j_\alpha \equiv j_\alpha(t=0)$, we can furthermore drop the $\dagger$ on j_α (as the operator is now Hermitian). We then expand the commutator to get

$$\sum_\Psi e^{-\beta\xi_\Psi}\left[\left\langle\Psi\left|e^{iHt/\hbar}j_\alpha e^{-iHt/\hbar}j_\beta\right|\Psi\right\rangle - \left\langle\Psi\left|j_\beta e^{iHt/\hbar}j_\alpha e^{-iHt/\hbar}\right|\Psi\right\rangle\right] \ .$$

Using the identity $e^{iHt/\hbar} = \sum_\Gamma |\Gamma\rangle\, e^{iE_\Gamma t/\hbar}\,\langle\Gamma|$, we get

$$\begin{aligned}\textstyle\sum_{\Psi\Phi\Gamma} e^{-\beta\xi_\Psi}\,&\left(\langle\Psi|\,\Phi\rangle\, e^{iE_\Phi t/\hbar}\,\langle\Phi\,|j_\alpha|\,\Gamma\rangle\, e^{-iE_\Gamma t/\hbar}\,\langle\Gamma\,|j_\beta|\,\Psi\rangle\right.\\ &\left.-\langle\Psi\,|j_\beta|\,\Phi\rangle\, e^{iE_\Phi t/\hbar}\,\langle\Phi\,|j_\alpha|\,\Gamma\rangle\, e^{-iE_\Gamma t/\hbar}\,\langle\Gamma|\,\Psi\rangle\right)\end{aligned}$$

and with $\langle \Psi | \Phi \rangle = \delta_{\Psi\Phi}$ and $\langle \Gamma | \Psi \rangle = \delta_{\Gamma\Psi}$ we get

$$\sum_{\Psi,\Gamma} e^{-\beta\xi_\Psi} e^{i(E_\Psi - E_\Gamma)t/\hbar} \langle \Psi | j_\alpha | \Gamma \rangle \langle \Gamma | j_\beta | \Psi \rangle - \sum_{\Gamma,\Phi} e^{-\beta\xi_\Gamma} e^{i(E_\Phi - E_\Gamma)t/\hbar} \langle \Gamma | j_\beta | \Phi \rangle \langle \Phi | j_\alpha | \Gamma \rangle \ .$$

Relabeling the states ($\Phi \to \Psi$ in the second term) gives

$$\sum_{\Psi\Gamma} \left(e^{-\beta\xi_\Psi} - e^{-\beta\xi_\Gamma} \right) e^{i(E_\Psi - E_\Gamma)t/\hbar} \langle \Psi | j_\alpha | \Gamma \rangle \langle \Gamma | j_\beta | \Psi \rangle \, .$$

So we can now write

$$\sigma_{\alpha\beta}(\omega) = \frac{1}{\hbar\omega V} \sum_{\Psi\Gamma} \frac{\left(e^{-\beta\xi_\Psi} - e^{-\beta\xi_\Gamma} \right)}{\mathcal{Q}(\mu, V, T)} \langle \Psi | j_\alpha | \Gamma \rangle \langle \Gamma | j_\beta | \Psi \rangle \int_0^\infty dt \, e^{i\omega t} e^{i(E_\Psi - E_\Gamma)t/\hbar} \ .$$

(Note that we could have written the Grand Partition function outside of the sum. For the moment, however, we wish to indicate via this notation that it "belongs" with the difference of exponentials, as this ratio will eventually become the difference between two Fermi functions.)

Before proceeding further with the evaluation of the matrix elements, let us finish off the integral which, as written, is undefined. Using the standard trick of adding an infinitesimal imaginary part to the frequency,

$$\int_0^\infty dt \, e^{i(\hbar\omega + i\eta + E_\Psi - E_\Gamma)t/\hbar} = \frac{\hbar}{i\left(\hbar\omega + i\eta + E_\Psi - E_\Gamma\right)} \left[e^{-\eta t/\hbar} e^{i(\hbar\omega + E_\Psi - E_\Gamma)t/\hbar} \right]_0^\infty$$

$$= \frac{\hbar}{i\left(\hbar\omega + i\eta + E_\Psi - E_\Gamma\right)} (0 - 1) = \frac{i\hbar}{\hbar\omega + E_\Psi - E_\Gamma + i\eta} \ .$$

The real part of this result is a delta function, as

$$\lim_{\eta \to 0} \frac{i}{x + i\eta} = \pi\delta(x) + iP\left(\frac{1}{x}\right)$$

and the Kubo-Greenwood formula is usually written with the delta function, as people are generally interested in the real part of σ. However, we will have need of the imaginary part later.

Substituting into our working KG formula, the factors of $\hbar$ cancel out, and we now have

$$\sigma_{\alpha\beta}(\omega) = \frac{1}{\omega V} \sum_{\Psi\Gamma} \frac{\left(e^{-\beta\xi_\Psi} - e^{-\beta\xi_\Gamma}\right)}{\mathcal{Q}(\mu, V, T)} \langle \Psi | j_\alpha | \Gamma \rangle \langle \Gamma | j_\beta | \Psi \rangle \frac{i}{\hbar\omega + E_\Psi - E_\Gamma + i\eta}$$

where it is understood we are talking about the *real* parts of both sides.

Next, let us fix the number of particles N in the system; sums over many-body states become sums over all many body states with N particles, and we must sum over all N explicitly. Then

$$\begin{aligned} e^{-\beta\xi_\Psi} - e^{-\beta\xi_\Gamma} &= e^{-\beta(E_\Psi - \mu N)} - e^{-\beta(E_\Gamma - \mu N)} \\ &= e^{\beta\mu N}\left(e^{-\beta E_\Psi} - e^{-\beta E_\Gamma}\right) \\ &= z^N\left(e^{-\beta E_\Psi} - e^{-\beta E_\Gamma}\right) \end{aligned}$$

with the fugacity $z = e^{\beta\mu}$, and we now have

$$\sigma_{\alpha\beta}(\omega) = \frac{1}{\omega V} \sum_N \sum_{\Psi\Gamma} z^N \frac{\left(e^{-\beta E_\Psi} - e^{-\beta E_\Gamma}\right)}{\mathcal{Q}(\mu, V, T)} \langle \Psi | j_\alpha | \Gamma \rangle \langle \Gamma | j_\beta | \Psi \rangle \frac{i}{\hbar\omega + E_\Psi - E_\Gamma + i\eta} .$$

As written above, $|\Psi\rangle$ and $|\Gamma\rangle$ are many-particle wavefunctions, and $j_{\alpha,\beta}$ are many-particle current operators. We would like to express these quantities in terms of single-particle states $|r\rangle$ and $|s\rangle$ (which are assumed known, via diagonalization of the single-particle Hamiltonian). We can also assume we know $\langle r | j | s \rangle = j^{rs}$, the matrix elements of the single-particle current operators (which can be derived from the single-particle Hamiltonian), and write the current operators as

$$j = \sum_{r,s} j^{rs} C_r^\dagger C_s$$

with the $C^\dagger$ and C representing creation and annihilation operators. A many-particle state, in this context, consists of N electrons distributed in some set $\{P\}$ of single-particle states. So, we can write a many-particle state $|\Psi\rangle$ as the product of a set of creation operators acting on the vacuum state:

$$|\Psi\rangle = C_{P_1}^\dagger C_{P_2}^\dagger \ldots C_{P_N}^\dagger |0\rangle$$

where $|0\rangle$ represents the vacuum state. We need a better notation for this; the usual notation (such as used in Fetter and Walecka) is explicit, but clumsy, particularly for the (relatively) simple manipulations we are interested in. So let us define the operators:

$$\begin{aligned} P_N^\dagger &= C_{P_1}^\dagger C_{P_2}^\dagger \dots C_{P_N}^\dagger \\ P_N &= C_{P_N} C_{P_{N-1}} \dots C_{P_1} \end{aligned}$$

where the subscript on P_N will keep track of how many creation/annihilation operators there are in the product, and the P itself reminds us that the N operators act on the vacuum state to create a set of states $\{P\}$. Using this new notation, we will write

$$\begin{aligned} |\Psi\rangle &= P_N^\dagger |0\rangle \qquad E_\Psi \to E_P \\ |\Gamma\rangle &= Q_N^\dagger |0\rangle \qquad E_\Gamma \to E_Q \end{aligned} \qquad \sum_\Psi \sum_\Gamma \to \sum_P \sum_Q \ .$$

(For example, for three electrons in states 13, 23, and 42, define $P = \{13, 23, 42\}$ and write the state as $P_3^\dagger |0\rangle$). The Kubo-Greenwood equation is now

$$\sigma_{\alpha\beta}(\omega) = \frac{1}{\omega V} \sum_N \sum_{PQ} z^N \frac{\left(e^{-\beta E_P} - e^{-\beta E_Q}\right)}{\mathcal{Q}(\mu, V, T)} (\text{matrix elements}) \frac{i}{\hbar\omega + E_P - E_Q + i\eta} \ ,$$

with the matrix elements given by, for example,

$$\langle \Psi | j_\alpha | \Gamma \rangle \langle \Gamma | j_\beta | \Psi \rangle = \sum_{rsqp} j_\alpha^{rs} j_\beta^{qp} \left\langle 0 \left| P_N C_r^\dagger C_s Q_N^\dagger \right| 0 \right\rangle \left\langle 0 \left| Q_N C_q^\dagger C_p P_N^\dagger \right| 0 \right\rangle .$$

In order to deal with this, let us deal separately with two cases involving the first matrix element: either $r = s$ or $r \neq s$.

Case 1: $r = s$

In this case, the first matrix element is $\left\langle 0 \left| P_N C_r^\dagger C_r Q_N^\dagger \right| 0 \right\rangle$. If $r \notin Q$, this vanishes (as C_r has no state r to annihilate). Otherwise, $r \in Q$, and this term reduces to $\left\langle 0 \left| P_N Q_N^\dagger \right| 0 \right\rangle$. If P and Q are different sets of states, this vanishes; otherwise, it reduces to ± 1 (depending on how many anticommutations it takes to arrange their operators in the same order). Then the second matrix

element is nonzero only if $p = q$, which means the product of matrix elements simplifies to

$$\pm \sum_{r,s \in Q} j_\alpha^{rr} j_\beta^{ss} .$$

Physically, this amounts to the current due to removing two electrons from the system and putting them back in the same states; we would expect to get zero current in this case, as we can see this explicitly by returning to our expression for the Kubo-Greenwood formula and noting that a factor in that expression along with this delta function gives

$$\left(e^{-\beta E_P} - e^{-\beta E_Q}\right) = \left(e^{-\beta E_P} - e^{-\beta E_P}\right) = 0.$$

Thus, the case of $r = s$ gives no contribution to the sum.

(We knew this from the start, of course, because we know that we get no conduction unless we excite an electron across the Fermi energy. That the term above actually has anything to do with the Fermi energy will be shown below.)

Case 2: $r \neq s$

In this case, only way for $\left\langle 0 \left| P_N C_r^\dagger C_s Q_N^\dagger \right| 0 \right\rangle$ to be nonzero is for one of the annihilation operators in P_N to annihilate the state created by $C_r^\dagger$, and for C_s to annihilate one of the states created by $Q_N^\dagger$. To be specific, let the state $r = P_i$ (that is, r is the ith state in the set $\{P\}$), and similarly let $s = Q_j$. We can then simplify this matrix element by anticommuting $C_r^\dagger$ through the last $i - 1$ operators in P_N, and anticommuting C_s through the first $j - 1$ operators of $Q_N^\dagger$. Explicitly, this gives the first matrix element as

$$\begin{aligned}(-1)^{i+j} \left\langle 0 \left| C_{P_N} C_{P_{N-1}} \ldots C_{P_i} C_r^\dagger \ldots C_{P_1} C_{Q_1}^\dagger C_{Q_2}^\dagger \ldots C_s C_{Q_j}^\dagger \ldots C_{Q_N}^\dagger \right| 0 \right\rangle \\ = (-1)^{i+j} \left\langle 0 \left| P'_{N-1} Q'^\dagger_{N-1} \right| 0 \right\rangle\end{aligned}$$

where P'_{N-1} represents the operator P_N without the ith term (that term being state r), and Q'_{N-1} is similarly missing term j (which is state s). We can now see that the remaining inner product results in $\delta_{P'Q'}$.

We now know that $P_N \neq Q_N$, so in the second matrix element, a similar argument gives (with $q = Q_k$ and $p = P_l$)

$$(-1)^{k+l} \langle 0 | P''_{N-1} Q''_{N-1} | 0 \rangle = \delta_{P''Q''}$$

where P'' is missing state l and Q'' is missing state k. We now have a product of delta functions $\delta_{P'Q'}\delta_{P''Q''}$, which can be collapsed if we remember that P' and P'' are both the state P missing some single state (i in the first case, and l in the second); if $P'_{N-1} = Q'_{N-1}$(as must be the case for a nonzero contribution from the first matrix element), then P_N and Q_N differ only by one state: if we remove one state from each, we have the same sets of states.

Now for the clever part: since P and Q differ by only one state — meaning, again, that we subtract some state r from P and some other state s from Q, and get identical sets of states — we must conclude that there is only *one* state r in P and *one* state s in Q that we can remove to generate identical sets. We must further conclude, then, that the sets P' and P'' are in fact the same set, and that Q' and Q'' are also the same set. This, in turn, implies that our single-particle-states $p = r$, $q = s$, and $i + j = k + l$.

Thus, this second case reduces the product of the two matrix elements to the simple expression

$$j_\alpha^{rs} j_\beta^{sr} \delta_{P'Q'}.$$

If we put this expression back into the Kubo-Greenwood formula, we now have

$$\sigma_{\alpha\beta}(\omega) = \frac{1}{\omega V} \sum_N \sum_{PQ} z^N \frac{\left(e^{-\beta E_P} - e^{-\beta E_Q}\right)}{\mathcal{Q}(\mu, V, T)} \frac{i}{\hbar\omega + E_P - E_Q + i\eta} j_\alpha^{rs} j_\beta^{sr} \delta_{P'Q'} .$$

Now the question is, what do we do about the P' and Q' in that expression? Well, remember that P' was the set P missing its ith term, which happened to be state r. we are summing over the set of all possible Ps, that is, over the set of all possible many-particle states consisting of N electrons — let us call that a "meta-set", that is, the set of all possible sets of single-particle states with a given number of particles. We can generate the same meta-set by summing over all sets of P' (i.e., the set of states with $N - 1$ electrons) and all possible ways of adding one electron to that P'. In

other words, and more succinctly,

$$\sum_P \equiv \sum_r \sum_{P' \not\ni r} \qquad \text{and} \qquad \sum_Q \equiv \sum_s \sum_{Q' \not\ni s} .$$

Now the $\delta_{P'Q'}$ makes sense: since $P' = Q'$, the delta function is really telling us that Q' includes neither r nor s. Writing the energies out (i.e., $E_P = E_{P'} + \epsilon_r$ — we are using E for the energy of a many-body state and ϵ for the energy of a single-particle state), and again remembering that $P' = Q'$ (so the energy difference between P and Q is really the energy difference between states r and s), we then have

$$\sigma_{\alpha\beta}(\omega) = \frac{1}{\omega V} \sum_{rs} j_\alpha^{rs} j_\beta^{sr} \left(e^{-\beta\epsilon_r} - e^{-\beta\epsilon_s}\right) \frac{i}{\hbar\omega + \epsilon_r - \epsilon_s + i\eta} \frac{z \sum_N \sum_{P'} z^{N-1} e^{-\beta E_{P'}}}{\mathcal{Q}(\mu V, T)}$$

keeping in mind that P' does *not* include states r or s. Also note how we have explicitly broken out one factor of the fugacity z.

Look at that last sum: $\sum_N \sum_{P'} z^{N-1} e^{-\beta E_{P'}}$. The sum over P' really means a sum over all possible many-particle states, with $N-1$ electrons, *that do not have states r or s occupied.* To handle this sum, let us temporarily remove that restriction and look at $\sum_N \sum_P e^{-\beta(E_P - \mu N)}$ where P again labels a many-particle state with N particles. We can write *this* as a sum over all possible occupations (0 or 1) of all single particle states n:

$$\sum_{n_1=0}^{1} \sum_{n_2=0}^{1} \sum_{n_3=0}^{1} \cdots e^{-\beta\left[(\epsilon_{n_1} - \mu n_1) + (\epsilon_{n_2} - \mu n_2) + \cdots\right]} .$$

The exponential can be factored, giving

$$\prod_i \sum_{n_i=0}^{1} e^{-\beta(\epsilon_i - \mu)} = \prod_i \left(1 + z e^{-\beta\epsilon_i}\right) .$$

So, we can now see how to handle our sum over P' by restricting the values of i:

$$\sum_N \sum_{P' \not\ni r,s} z^{N-1} e^{-\beta E_{P'}} = \prod_{i \neq r,s} \left(1 + z e^{-\beta\epsilon_i}\right) .$$

If we now rewrite the partition function (it's been hanging around all this time; you were wondering when we'd do something with it) using Pathria [50](p 142, eq 16):

$$\mathcal{Q}(\mu V,T)=\prod_i\left(1+ze^{-\beta\epsilon_i}\right)$$

we then find the ratio of our sum with the partition function to be

$$\frac{\prod_{i\neq r,s}\left(1+ze^{-\beta\epsilon_i}\right)}{\prod_i\left(1+ze^{-\beta\epsilon_i}\right)}=\frac{1}{\left(1+ze^{-\beta\epsilon_r}\right)\left(1+ze^{-\beta\epsilon_s}\right)}$$

and we have a factor that looks like

$$\frac{z\left(e^{-\beta\epsilon_r}-e^{-\beta\epsilon_s}\right)}{\left(1+ze^{-\beta\epsilon_r}\right)\left(1+ze^{-\beta\epsilon_s}\right)},$$

and a little algebra gives

$$\begin{aligned}
\frac{z\left(e^{-\beta\epsilon_r}-e^{-\beta\epsilon_s}\right)}{\left(1+ze^{-\beta\epsilon_s}\right)\left(1+ze^{-\beta\epsilon_s}\right)} &= \frac{ze^{-\beta\epsilon_r}e^{-\beta\epsilon_s}\left(e^{\beta\epsilon_s}-e^{\beta\epsilon_r}\right)}{\left(1+ze^{-\beta\epsilon_r}\right)\left(1+ze^{-\beta\epsilon_s}\right)} \\
&= \frac{z^{-1}\left(e^{\beta\epsilon_s}-e^{\beta\epsilon_r}\right)}{z^{-2}e^{\beta\epsilon_r}e^{\beta\epsilon_s}\left(1+ze^{-\beta\epsilon_r}\right)\left(1+ze^{-\beta\epsilon_s}\right)} \\
&= \frac{z^{-1}\left(e^{\beta\epsilon_s}-e^{\beta\epsilon_r}\right)}{\left(z^{-1}e^{\beta\epsilon_s}+1\right)\left(z^{-1}e^{\beta\epsilon_r}+1\right)} \\
&= \frac{z^{-1}e^{\beta\epsilon_s}+1-z^{-1}e^{\beta\epsilon_r}-1}{\left(z^{-1}e^{\beta\epsilon_s}+1\right)\left(z^{-1}e^{\beta\epsilon_r}+1\right)} \\
&= \frac{1}{z^{-1}e^{\beta\epsilon_r}+1}-\frac{1}{z^{-1}e^{\beta\epsilon_s}+1} \\
&= f\left(\epsilon_r\right)-f\left(\epsilon_s\right)\ .
\end{aligned}$$

With this result, we now have

$$\sigma_{\alpha\beta}(\omega)=\frac{1}{\omega V}\sum_{rs}j_\alpha^{rs}j_\beta^{sr}\left[f\left(\epsilon_r\right)-f\left(\epsilon_s\right)\right]\frac{i}{\hbar\omega+\epsilon_r-\epsilon_s+i\eta}$$

and we are almost done. At this point, note that the difference of Fermi functions tells us that we are taking an electron below the Fermi level and exiting it to a state above, which is the usual way we think of a linear response in ideal systems.

Finally, we need to take electron spin into account: assuming spin level degeneracy, this just means we need to multiply by two. (We *do not* multiply by four since there are no spin-flip processes, i.e., an $\uparrow$ electron below the Fermi level gets excited to an $\uparrow$ electron above it.)

Our result for the Kubo-Greenwood formula is then

$$\sigma_{\alpha\beta}(\omega) = \frac{2}{\omega V} \sum_{rs} \langle r | j_\alpha | s \rangle \langle s | j_\beta | r \rangle [f(\epsilon_r) - f(\epsilon_s)] \frac{i}{\hbar\omega + \epsilon_r - \epsilon_s + i\eta} \tag{A.2}$$

with an (implied) limit $\eta \to 0$.

Appendix B

The square-lattice Anderson impurity model

> "Listen, three eyes," he said, "don't you try to out-wierd me, I get stranger things than you free with my breakfast cereal."
>
> - Douglas Adams [23]

We present here some results related to the square lattice Anderson impurity model. Much of the first section is elementary, and is taken from chapter 10 of Ashcroft and Mermin [51]; it is included here for completeness.

Aside from collecting various relations used in other parts of this thesis, our goal in this Appendix is to estimate the low-field Hall coefficient for a two dimensional system of the kind considered in Chapter 3. To this end we apply a technique described by N. P. Ong [44] (which also appears in the Berkeley group's explanation of their A_3C_{60} results), in combination with an approximate treatment of disorder which is quantitatively reliable only in the low-disorder limit. We can then compare this estimate of R_H to the results of calculations based on our implementation of the Kubo-Greenwood formula, as a check on the validity of the latter (though the approximation we make in implementing Ong's formula means that we should not expect perfect agreement).

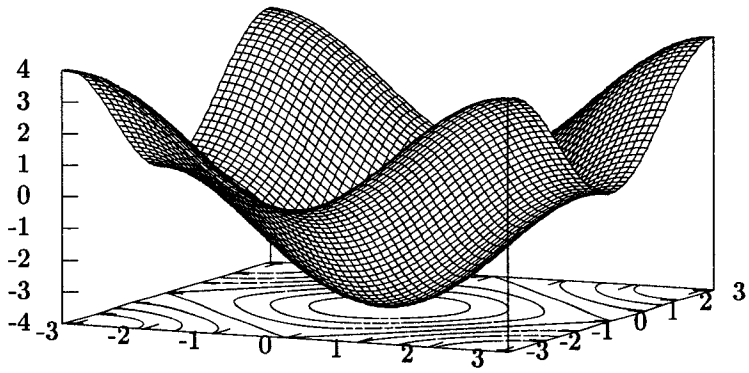

Figure B.1: Dispersion relation in the first Brillouin zone for the square 2-d tight binding model.

B.1 The square-lattice nearest-neighbor tight binding model

Before discussing the Anderson impurity model further it is necessary to present some results for the square-lattice, single-orbital, nearest-neighbor tight-binding model.

B.1.1 Energy and Fermi surfaces

The dispersion relation for the square-lattice tight-binding model is

$$E = -2\left(\cos k_x + \cos k_y\right) \tag{B.1}$$

where we have rescaled the energy by the energy scale $\hat{\epsilon}$ (the nonzero matrix elements in the single-particle Hamiltonian are all $-\hat{\epsilon}$) and the components of $\mathbf{k}$ by the lattice constant $\hat{a}$; this makes all quantities dimensionless. (Keep in mind that derivatives will produce factors of $\hat{a}$ or $\hat{\epsilon}$.) Figure B.1 shows the energy in the first Brillouin zone, and Fig. B.2 shows the Fermi surface for different Fermi energies.

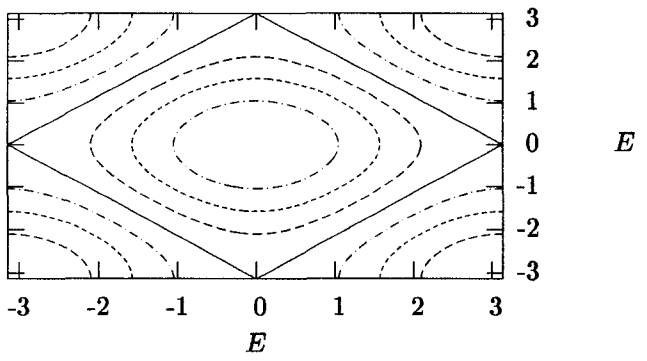

Figure B.2: Fermi surfaces in the first Brillouin zone. The contours are at $1\hat{\epsilon}$ increments.

We can invert Eq. (B.1) to find

$$k_y = \pm \cos^{-1}\left(-\frac{E}{2} - \cos k_x\right) = \pi \pm \cos^{-1}\left(\frac{E}{2} + \cos k_x\right)$$

which gives the Fermi surface $k_y = f(k_x)$ at energy E. Note that since the energy is symmetric with respect to k_x and k_y, this expression (and many others below) are also symmetric with respect to interchange of k_x and k_y.

B.1.2 Electron velocity

The velocity of an electron wavepacket with crystal momentum centered at $\mathbf{k}$ is given by

$$\mathbf{v_k} = \frac{1}{\hbar}\vec{\nabla}_k E(\mathbf{k}) \tag{B.2}$$

$$= \frac{2\hat{a}\hat{\epsilon}}{\hbar}\left[\sin(k_x)\,\hat{k}_x + \sin(k_y)\,\hat{k}_y\right] \tag{B.3}$$

$$= \frac{\hat{a}\hat{\epsilon}}{\hbar}\left(v_x\hat{k}_x + v_y\hat{k}_y\right) \tag{B.4}$$

where the last line defines $v_{x,y} = 2\sin(k_{x,y})$ as the dimensionless components of $\mathbf{v_k}$. (Note the factors of $\hat{a}$ and $\hat{\epsilon}$ that result from the derivative.) It will be useful to have v_y as a function of v_x, so we eliminate k_y using the relation above

$$\begin{aligned} v_y &= 2\sin k_y && \text{(B.5)} \\ &= 2\sin\left(\cos^{-1}\left(-\frac{E}{2} - \cos k_x\right)\right) && \text{(B.6)} \\ &= \pm 2\sqrt{1-\left(\frac{E}{2}+\cos k_x\right)^2} && \text{(B.7)} \end{aligned}$$

which, effectively, gives us the components of $\mathbf{v_k}$ as functions of k_x. We now invert the relation for v_x and substitute:

$$\begin{aligned} k_x &= \sin^{-1}\left(\frac{v_x}{2}\right) \\ v_y &= \pm 2\sqrt{1-\left(\frac{E}{2}+\cos\sin^{-1}\frac{v_x}{2}\right)^2} \\ &= \pm 2\sqrt{1-\left(\frac{E}{2}\pm\sqrt{1-\frac{v_x^2}{4}}\right)^2} \\ &= \pm\sqrt{4-\left(E\pm\sqrt{4-v_x^2}\right)^2}\,. \end{aligned}$$

It is also useful to determine $\langle v_F \rangle$, the average value for v on the Fermi surface; this will be used below, and is also used in Chapter 4. It is simplest to find $\langle v_F \rangle$ numerically; the result is shown in Fig B.3. For 2/3 filling, $\langle v_F \rangle = 2.283$.

B.2 R_H in the zero-disorder limit

B.2.1 Ong's technique

N. P. Ong [44] developed an elegant geometric method to calculate σ'_{xy} in two-dimensional metals based on a "scattering path length" construct.

For each $\mathbf{k}$ point on the Fermi surface define the "scattering path length" vector $\vec{l} = \mathbf{v_k}\tau_{\mathbf{k}}$ where

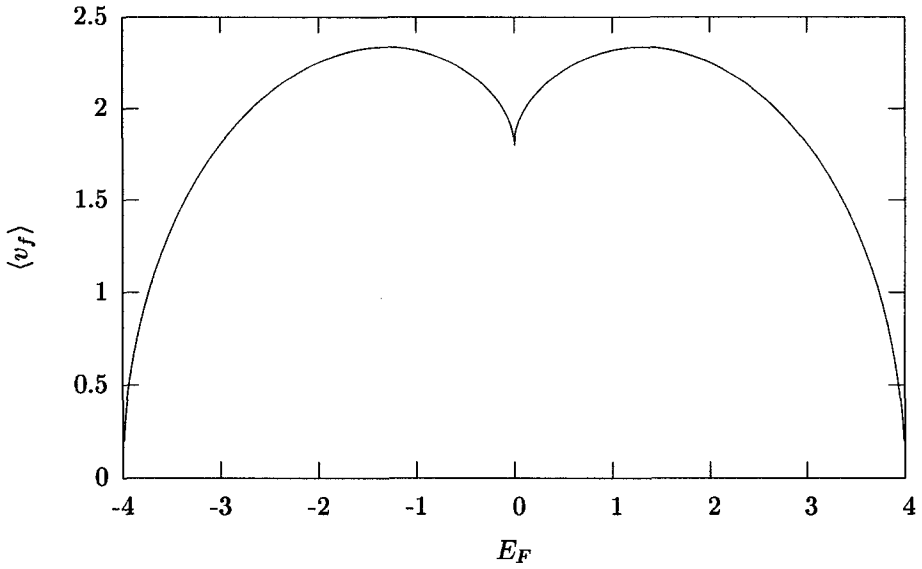

Figure B.3: Average Fermi velocity $\langle v_F \rangle$ as a function of Fermi energy.

τ is the relaxation time (which, in general, may depend on wave vector). If we move $\mathbf{k}$ around the Fermi surface, the vector $\vec{l}$ sweeps out an area in "l" space. This area, denoted A_l, is related to σ'_{xy} by

$$\sigma'_{xy} = \frac{e^2}{h}\frac{1}{\Phi_0} 2A_l \ .$$

There is an obvious difficulty in applying this to the Anderson impurity models of interest to us: there is no simple way to determine $\tau_{\mathbf{k}}$, particularly at the rather large values of D for which we can obtain meaningful numerical results from finite cluster Kubo-Greenwood calculations. As we are ultimately interested in R_H, we can proceed by assuming that the relaxation time is in fact independent of wave vector, so that $\tau_{\mathbf{k}} \equiv \tau$; factors of τ^2 that appear in both the numerator and denominator of $R_H = \sigma'_{xy}/\sigma^2_{xx}$ will then cancel out.[1] (We will return to the issue of finding σ_{xx} in the next subsection.)

We will evaluate A_l numerically. For convenience, we will factor τ out of $\vec{l}$, and denoting the components of $\vec{l}$ by x and y the curve traced out by the scattering path vector as the wave vector

[1] Although this treatment of the disorder is approximate, the non-circular character of the Fermi surface is properly accounted for.

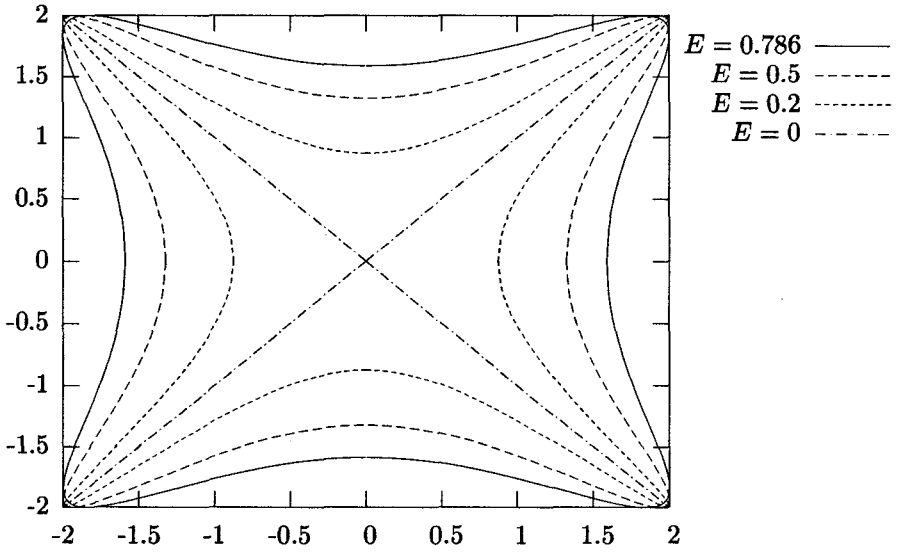

Figure B.4: Curves defined by $\vec{l}$ as we move around the Fermi surface of the square lattice tight binding model. The axes have units of $\hat{a}\epsilon\tau/\hbar$. Note that the area bounded by the curve vanishes at $E = 0$; for negative E values, the curves are identical to the positive E curves, but are traced out in the other direction (which causes the expected sign change at half filling). $E = 0.786$ corresponds to 2/3 filling.

circles the Fermi surface is given by

$$y(x) = \pm\sqrt{4 - \left(E \pm \sqrt{4 - x^2}\right)^2}$$

where the various combinations of $\pm$ form a closed curve. This curve is symmetric about both axes and the lines $y = \pm x$; see Fig. B.4.

Now to find the area inside this curve, we concentrate on the first quadrant. Using Cartesian coordinates, we find the area under the "top" half of the curve in the first quadrant, then subtract the area of the triangle below the $x = y$ line. This will give us the area bounded below by $x = y$, bounded on the left by the y axis, and bounded on the top by the curve (which corresponds to choosing the negative branch of the innermost square root, and the positive branch of the outermost). This area is $\frac{1}{8}$th of A_l. If we denote by Q (to pick a letter at random) the upper limit of integration, we can then write

$$A_l = 8\left\{\left[\int_0^Q dx\, y\,(x)\right] - \frac{1}{2}Q^2\right\}$$

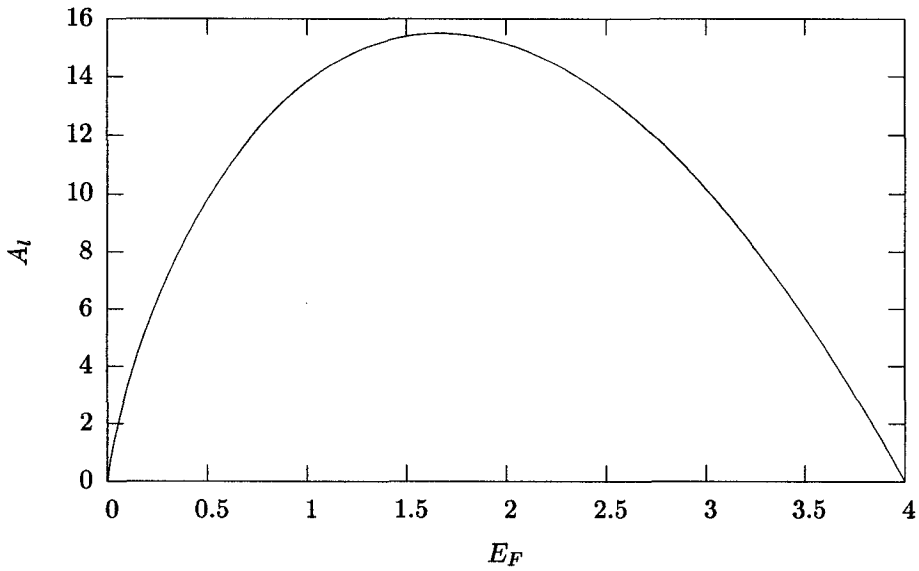

Figure B.5: A_l as a function of Fermi energy.

where the last term in braces is the area of the triangle.

Next, we need to find Q. We are integrating with respect to x from $x = 0$ to the point where the curve meets the $x = y$. This point is part of the "top" of the curve, so it is given by

$$\begin{aligned} y(Q) &= Q \\ \sqrt{4 - \left(E - \sqrt{4 - Q^2}\right)^2} &= Q \end{aligned}$$

which can be solved for Q, giving

$$Q = 2\sqrt{1 - \frac{E^2}{16}}\,.$$

So finally, our integral is

$$A_l = 8\left\{\left[\int_0^Q dx \sqrt{4 - \left(E - \sqrt{4 - x^2}\right)^2}\right] - \frac{1}{2}Q^2\right\}$$

which, given E, we can evaluate numerically. The result is shown in Fig. B.5; for 2/3 filling ($E_F = .786$) A_l is approximately 12.5. The units are those of $(v_F\tau)^2$, which are $(\hat{a}\hat{\epsilon}\tau/\hbar)^2$.

B.2.2 Longitudinal conductivity and onward to R_H

Conventional Boltzmann transport theory, under the assumption of an isotropic Fermi surface and relaxation time independent of wave vector, leads to the following well known relation [52] between conductivity, Fermi velocity, relaxation time, and density of states $\mathcal{N}$ at the Fermi energy:[2]

$$\sigma_{xx} = \frac{1}{2} e^2 v_F^2 \tau \mathcal{N} \ . \tag{B.8}$$

Of course, our Fermi surface is not isotropic, and our use of this formula is therefore an approximation. We will make a further approximation, and use the average Fermi velocity $\langle v_F \rangle$ as calculated numerically above (see Fig. B.3).[3] We will use $\mathcal{N}$ as calculated numerically in Fig. 3.1. First, let us rewrite the expression for the conductivity so that all of the factors in it are expressed in dimensionless form. The units of σ_{xx} should be e^2/h, giving

$$\begin{aligned} \sigma_{xx} &= \frac{1}{2} e^2 \left(\frac{\bar{v}_F \hat{a} \hat{\epsilon}}{\hbar} \right)^2 \tau \frac{\bar{\mathcal{N}}(E_F)}{\hat{\epsilon} \hat{a}^2} \\ \sigma_{xx} &= \frac{1}{2} \frac{e^2 \hat{\epsilon}}{\hbar^2} \bar{v}_F^2 \bar{\mathcal{N}}(E_F) \tau \ . \end{aligned}$$

We then have

$$\begin{aligned} R_H &= \frac{\sigma_{xy}'}{\sigma_{xx}^2} \\ &= \frac{\frac{e^2}{\hbar} \frac{1}{\Phi_0} 2A_l \left(\frac{\hat{a}\hat{\epsilon}}{\hbar} \tau \right)^2}{\left[\frac{1}{2} \frac{e^2 \hat{\epsilon}}{\hbar^2} \bar{v}_F^2 \bar{\mathcal{N}}(E_F) \tau \right]^2} \\ &= \frac{\hat{a}^2}{e(2\pi)^2} \frac{8A_l}{\bar{v}_F^2 \bar{\mathcal{N}}(E_F)} \\ &= \frac{\hat{a}^2}{e(2\pi)^2} \frac{8(12.5)}{(2.282)^2 (0.3073)^2} \\ &= \frac{\hat{a}^2}{e} 0.989 \end{aligned}$$

[2] Ziman's expression has a leading factor of 1/3, which reflects the three-dimensional nature of the system he was discussing. The correct factor for two-dimensional systems is 1/2.

[3] Given these approximations, we expect the resultant value of R_H to be only roughly accurate, which will be good enough to compare with our KG results.

using $\Phi_0 = h/e$ and the values appropriate for 2/3 filling: $\bar{v}_F = 2.282$ and $\bar{N}_F = 0.3073$.

Bibliography

[1] Douglas Adams. *The Restaurant at the End of the Universe.* Harmony Books, New York, 1980.

[2] Douglas Adams. *The Hitchhiker's Guide to the Galaxy.* Harmony Books, New York, 1980.

[3] Li Lu, Vincent H. Crespi, M. S. Fuhrer, A. Zettl, and Marvin L. Cohen. Universal Form of Hall Coefficient in K and Rb Doped Single Crystal C_{60}. *Phys. Rev. Lett.*, 74(9):1637–1640, February 1995.

[4] J. Bass. Deviations from Matthiessen's Rule. *Adv. Phys.*, 21(9):431–604, May 1972.

[5] J. Bass, W. P Pratt Jr., and P. A. Scroeder. The temperature-dependent electrical resistivities of the alkali metals. *Rev. Mod. Phys.*, 62(3):645–744, 1990.

[6] Martin P. Gelfand and Jian Ping Lu. Orientational Disorder and Electronic States in C_{60} and A_3C_{60}, where A is an Alkali Metal. *Phys. Rev. Lett.*, 68(7):1050–1053, February 1992.

[7] Martin P. Gelfand and Jian Ping Lu. Orientational disorder and normal-state electronic-transport properties of A_3C_{60}. *Phys. Rev. B*, 46(7):4367–4370, August 1992.

[8] S. G. Kaplan, S. Wu, H.-T. S. Lihn, H. D. Drew, Q. Li, D. B. Fenner, Julia M. Phillips, and S. Y. Hou. Normal State ac Hall Effect in $YBa_2Cu_3O_7$ Thin Films. *Phys. Rev. Lett.*, 76(4):696–699, January 1996.

[9] A. MacKinnon. The conductivity of the one-dimentional disordered Anderson model: a new numerical method. *J. Phys. C*, 13:1031–1034, 1980.

[10] N. Giordano. Numerical study of conductance fluctuations in disordered metals. *Phys. Rev. B*, 36(8):4190–4196, September 1987.

[11] D. Mayou. Calculation of the conductivity in the short-mean-free-math regime. *Europhys. Lett.*, 6:549–554, July 1988.

[12] L. E. Ballentine and J. E. Hammerberg. Computation of electrical conductivity and thermoelectric power in strong-scattering disordered metals. *Can. J. Phys.*, 62:692–700, 1984.

[13] Ahmed Houari and R. Harris. The Hall effect in simple glassy structures. *J. Phys. Condens. Mat.*, 4:1505–1512, 1991.

[14] G. Czycholl. The Diagonal and Hall conductivity of a two-dimensional electron system in a strong magnetic field. *Solid State Commun.*, 67(5):499–503, 1988.

[15] N. Troullier and J. L. Martins. Structural and electronic properties of C_{60}. *Phys. Rev. B*, 46:1754, 1992.

[16] S. Satpathy. Electronic structure of the truncated-icosahedral C_{60} cluster. *Chem. Phys. Lett.*, 130:545, 1986.

[17] S. Satpathy, V. P. Antropov, O. K. Andersen, O. Jepsen, O. Gunnarssson, and A. I. Liechtenstein. Conduction-band structure of alkali-metal-doped C_{60}. *Phys. Rev. B*, 46(3):1773–1793, July 1992.

[18] J. E. Fischer, G. Bendele, R. Dinnebier, P. W. Stephens, C. N. Lin, N. Bykovetz, and Q. Zhu. Structural-analysis of fullerene and fulleride solids from synchrotron X-ray-powder diffraction. *J. Phys. Chem. Solids*, 56:1445, 1995.

[19] I. I. Mazin, A. I. Liechtenstein, O. Gunnarsson, O. K. Anderson, and V. P. Antropov. Orientational order in A_3C_{60}: Antiferromagnetic Ising models for the fcc lattice. *Phys. Rev. Lett.*, 70(26):4142–4145, June 1993.

[20] S. Teslic, T. Egami, and J. E. Fischer. Short-range antiferromagnetic orientational correlations in Rb_3C_{60}. *Phys. Rev. B*, 51(9):5973–5976, 1995.

[21] P. W. Anderson. Absense of diffusion in certain random lattices. *Phys. Rev.*, 109(1):1492–1505, March 1958.

[22] J. A. Pople. Molecular-Orbital Theory of Diamagnetism. I. An Approximate LCAO Scheme. *J. Chem. Phys.*, 37(1):53–59, July 1962.

[23] Douglas Adams. *Life, the Universe, and Everything.* Harmony Books, New York, 1982.

[24] Ping Sheng. *Introduction to Wave Scattering, Localization, and Mesoscopic Phenomena.* Academic Press, Inc., San Diego, 1995.

[25] E. Abrahams, P. W. Anderson, D. C. Licciardello, and T. V. Ramakrishnan. Scaling Theory of Localization: Absence of Quantum Diffusion in Two Dimensions. *Phys. Rev. Lett.*, 42:673, 1979.

[26] P. A. Lee, A. Douglas Stone, and H. Fukuyama. Universal conductance fluctuations in metals: Effects of finite temperature, interactions, and magnetic field. *Phys. Rev. B*, 35(3):1039–1070, January 1987.

[27] B. L. Al'tschuler and D. E. Khmel'nitskii. Fluctuations properties of small conductors. *JETP Lett.*, 42(7):359–363, October 1985.

[28] B. L. Al'tshuler. Fluctuations in the extrinsic conductivity of disordered conductors. *JETP Lett.*, 41(12):648–651, June 1985.

[29] B. L. Al'tshuler, V. E. Kravtsov, and I. V. Lerner. Statistical properties of mesoscopic fluctuations and similarity theory. *JETP Lett.*, 43(7):441–444, April 1986.

[30] Shanhui Xiong, N. Read, and A. Douglas Stone. Mesoscopic conductance and its fluctuations at a nonzero Hall angle. *Phys. Rev. B*, 56(7):3982–4012, August 1997.

[31] A. Douglas Stone. Magnetoresistance fluctuations in mesoscopic wires and rings. *Phys. Rev. Lett.*, 54(25):2692–2695, June 1985.

[32] X. C. Xie and S. Das Sarma. Numerical study of conductance fluctuations based on the Kubo formula. *Phys. Rev. B*, 38(5):3529–3532, August 1988.

[33] R. C. Haddon, A. F. Hebard, M. J. Rosseinsky, D. E. Murphy, S. J. Duclos, K. B. Lyons, B. Miller, J. Rosamilia, R. M. Fleming, A. R. Kortan, S. H. Glarum, A. V. Makhija, A. J. Muller, R. H. Eick, S. M. Zahurak, R. Tycko, G. Dabbagh, and F. A. Thiel. Conducting films of C_{60} and C_{70} by alkali-metal doping. *Nature*, 350:320–322, 1991.

[34] A. F. Hebard, M. J. Rosseinsky, R. C. Haddon, D. W. Murphy, S. H. Glarum, , T. T. M. Palstra, A. P. Ramirez, and A. R. Kortan. Superconductivity at 18K in potassium-doped C_{60}. *Nature*, 350:600–601, 1991.

[35] M. J. Rosseinsky, A. P. Ramirez, S. H. Glarum, D. W. Murphy, R. C. Haddon, A. F. Hebard, T. T. M. Palstra, A. R. Kortan, S. M. Zahurak, and A. V. Makhija. Superconductivity at 28 K in Rb_xC_{60}. *Phys. Rev. Lett.*, 66:2830–2832, 1991.

[36] Martin P. Gelfand. Alkali fullerides: Theoretical perspectives, progress and problems. *Superconductivity Review*, 1:103–150, 1994.

[37] F. Aryasetiawan, O. Gunnarsson, E. Koch, and R. M. Martin. Pauli Susceptibility of A_3C_{60} (A=K, Rb). *Phys. Rev. B*, 55(16):10165–10168, April 1997.

[38] T. T. M. Palstra, R. C. Haddon, A. F. Hebard, and J. Zaanen. Electronic transport properties of K_3C_{60} films. *Phys. Rev. Lett.*, 68(7):1054–1057, February 1992.

[39] T. T. M. Palstra, A. F. Hebard, R. C. Haddon, and P. B. Littlewood. Fermi-liquid behavior in the electrical resistivity of K_3C_{60} and Rb_3C_{60}. *Phys. Rev. B*, 50(9):3462–3465, 1994.

[40] S. K. Watson, K. Allen, D. W. Denlinger, and F. Hellman. Destruction of superconductivity in the narrow-band metal K_3C_{60}s. *Phys. Rev. B*, 55(6):3866–3869, February 1997.

[41] Peter W. Stephens, Laszlo Mihaly, Peter L. Lee, Robert L. Whetten, Shiou-Mei Hwang, Richard Kaner, Francois Deiderich, and Karoly Holczer. Structure of single-phase superconducting K_3C_{60}. *Nature*, 351:632–634, June 1991.

[42] S. C. Erwin and E. J. Mele. Tight-binding parameterization of first-principles electronic dispersion in orientationally disordered A_3C_{60}. *Phys. Rev. B*, 50(8):5689–5692, August 1994.

[43] E. J. Mele and S. C. Erwin. Electron propagation in orientationally disordered fullerides. *Phys. Rev. B*, 50(4):2150–2158, July 1994.

[44] N. P. Ong. Geometric interpretation of the weak-field Hall conductivity in two-dimensional metals with arbitrary Fermi surface. *Phys. Rev. B*, 43:193, 1991.

[45] Steven C. Erwin and Warren E. Pickett. Theoretical normal-state transport properties of K_3C_{60}. *Phys. Rev. B*, 46(21):14257–14260, December 1992.

[46] Vincent H. Crespi and Marvin L. Cohen. Scattering mechanisms in Rb-doped single-crystal C_{60}. *Phys. Rev. B*, 52(5):3619–3623, August 1995.

[47] J. G. Hou, Li Lu, Vincent H. Crespi, X.-D. Xiang, A. Zettl, and Marvin L. Cohen. Resistivity Saturation in alkali-doped C_{60}. *Solid State Commun.*, 93(12):973–977, 1995.

[48] Joachim Schulte and Michael C. Böhm. Charge Distribution in K_3C_{60} revisited: Incomplete Alkali to C_{60} electron transfer. *Solid State Commun.*, 93(3):249–253, 1995.

[49] Gerald D. Mahan. *Many-particle physics.* Plenum Press, New York, 2nd edition, 1990. ISBN 0306434237.

[50] R. K. Pathria. *Statistical Mechanics.* Pergamon Press, Oxford, New York, 1972. ISBN 0080189946.

[51] Neil W. Ashcroft and N. David Mermin. *Solid State Physics.* Harcourt Brace College Publishers, Orlando, Florida, 1976. ISBN 0-03-083993-9.

[52] J. M. Ziman. *Principles of the Theory of Solids.* Cambridge University Press, Cambridge, Great Britain, 1984. ISBN 0-521-29733-8.